ICP Enhanced HIPIMS System Design and Characterisation

A Thesis Submitted to the
College of Graduate and Postdoctoral Studies
in Partial Fulfillment of the Requirements
for the degree of Master of Science
in the Department of Physics and Engineering Physics
University of Saskatchewan
Saskatoon

By
Alex Chang

Permission to Use

In presenting this thesis in partial fulfilment of the requirements for a Postgraduate degree from the University of Saskatchewan, I agree that the Libraries of this University may make it freely available for inspection. I further agree that permission for copying of this thesis in any manner, in whole or in part, for scholarly purposes may be granted by the professor or professors who supervised my thesis work or, in their absence, by the Head of the Department or the Dean of the College in which my thesis work was done. It is understood that any copying or publication or use of this thesis or parts thereof for financial gain shall not be allowed without my written permission. It is also understood that due recognition shall be given to me and to the University of Saskatchewan in any scholarly use which may be made of any material in my thesis.

Requests for permission to copy or to make other use of material in this thesis in whole or part should be addressed to:

Dean of the College of Graduate and Postdoctoral Studies
116 Thorvaldson Building, 110 Science Place
University of Saskatchewan
Saskatoon, Saskatchewan S7N 5C9
Canada

Head of the Department of Physics and Engineering Physics
116 Science Place, Room 163
University of Saskatchewan
Saskatoon, Saskatchewan S7N 5E2
Canada

Abstract

A custom inductively coupled plasma assisted high-power impulse magnetron sputtering system was designed and assembled for the study of $\mathbf{E} \times \mathbf{B}$ plasma spoke instabilities. The magnetron plasma was characterized using time-resolved Langmuir probe, floating probe, optical emission spectroscopy and high-speed camera methods. Fluctuations in the floating potential of the plasma were observed, this was attributed to localized rotating spokes. Localized spoke structures were observed in the camera footage, the shape and size of these spokes were found to be influenced by argon gas rarefaction.

Acknowledgements

J'aimerais remercier mon directeur de thèse Lénaïc Couëdel, qui a toujours été à l'écoute de mes questions et à même de me conseiller. Votre soutien m'a beaucoup aidé dans ce projet. Ce fut un grand plaisir de travailler avec vous. I would like to express my deep gratitude to my supervisor Michael Bradley for giving me this opportunity. This project would not have been possible without your continuous support.

Thanks to the Natural Sciences and Engineering Research Council for funding this project. And thanks to the faculty and staff of the University of Saskatchewan physics and Engineering physics department for their support throughout my degree.

I would also like to thank my lab mates Joel Moreno, Nathan Nelson and Ayub Khodaee for all the discussions we had and time spent together in the plasma labs. Thanks to Patrick Braun for reviewing my thesis and pointing out all the typos. Thanks to everyone in the choices group for our much-needed weekly soup pilgrimages.

感謝我的爸爸媽媽辛苦把我養大，還感謝哥哥姊姊和嫂嫂，你們一路的支持讓我可以讀完碩士。

Contents

Permission to Use i

Abstract ii

Acknowledgements iii

Contents iv

List of Tables vi

List of Figures vi

List of Abbreviations ix

1 Introduction 1

2 Plasma Physics Background 2
- 2.1 Plasma Temperature . . . 2
- 2.2 Magnetized Plasmas . . . 5
  - 2.2.1 Gyromotion . . . 5
  - 2.2.2 **E** cross **B** drift . . . 7
  - 2.2.3 Transport Across Magnetic Fields . . . 8
  - 2.2.4 Plasma Spokes . . . 9
- 2.3 Plasma Generation . . . 10
  - 2.3.1 Magnetron Plasma Source . . . 10
  - 2.3.2 High-Power Impulse Magnetron Sputtering . . . 14
  - 2.3.3 Inductively Coupled Plasma . . . 16
- 2.4 Plasma Characterization Techniques . . . 18
  - 2.4.1 Langmuir Probe Theory . . . 18
  - 2.4.2 Optical Emission Spectroscopy . . . 20
  - 2.4.3 Morphological Image Processing . . . 22

3 Experiment 24
- 3.1 HiPIMS Design . . . 24
- 3.2 ICP and Test Chamber . . . 30
- 3.3 Time-Resolved Langmuir Probe Measurements . . . 31
- 3.4 Floating Probes . . . 32
- 3.5 High-speed camera . . . 33
- 3.6 Optical Emission Spectroscopy . . . 35

4 Analysis 37
- 4.1 Time resolved Langmuir probe . . . 37

4.2 Probe array measurements and EMD 41
4.3 Cross-correlation 45
4.4 High-Speed Camera 46

5 Results **49**
5.1 Magnetron Discharge Characteristics 49
5.2 Emission Spectroscopy 55
5.3 Time Resolved Langmuir Analysis 59
5.4 Floating Probes 66
5.5 High-speed Camera 71
5.6 Arcing 81

6 Conclusion **83**

References **86**

Appendix A **90**
A.1 Figures 90

List of Tables

2.1 Properties and costs of gases 11

5.1 Spectroscopic data for Ar I lines. 57
5.2 Particle axial drift time and calculated speed 62

List of Figures

2.1 Scales of plasma temperature and densities 4
2.2 $\mathbf{E} \times \mathbf{B}$ drift of a negatively charged particle in the space above a magnetron target. 8
2.4 Simplified magnetron operation diagram 12
2.5 Types of magnetron magnetic configurations 13
2.6 HiPIMS discharge current curve with varying values of self-sputtering parameter Π_{ss}. 15
2.7 Simplified diagram of inductive coils on top of chamber, generating ICP in H-mode. 17
2.8 Theoretical IV curve of Langmuir Probe 18
2.9 Examples of structuring element shapes. 22
2.10 Morphological operations performed on an image. 23

3.1 Cross-section of magnetron assembly 25
3.2 Magnetron exploded isometric view 26
3.3 (a) Magnetic field lines of magnetron with 304 stainless-steel housing, (b) Magnetic field lines of new magnetic housing. Simulated using FEMM 27
3.4 Bolts sputtered with stainless steel 28
3.5 Magnetic field values 28
3.6 Silicon target magnetron discharge plasma. The bright annulus on the target surface is the magnetron racetrack. The plasma is seen extending out in front of the magnetron due to the type-2 unbalanced magnetic configuration. . . . 29
3.7 Vacuum Chamber 30
3.8 Probe and Camera Block Diagram 32
3.9 Assembled magnetron with radial probes 33
3.10 Camera trigger timing 34
3.12 Raytrace diagram of focusing system. 36

4.1 3D plot of time resolved Langmuir probe data for 800 V magnetron discharge with a silicon target. 37

4.2 Fitting procedure to obtain electron transition and electron saturation data from I-V curves. (a) Fitting of arctangent curve to determine location of knee, (b) fitting of transition and electron saturation regions. 38
4.3 Time resolved I-V curves for Langmuir analysis. 39
4.4 Examples of I-V curves not suitable for Langmuir analysis. 40
4.5 Location of I-V curve discontinuities at the start and end of magnetron discharge. 40
4.6 EMD processed signal 41
4.7 Mode mixing example. 45
4.8 Cross-correlation example. 46
4.9 Image processing steps from original image to processed image. 48

5.1 Magnetron Discharge Waveform with varying Pulse Lengths. 49
5.2 Magnetron discharge waveform with varying pulse lengths in ICP 50
5.3 Silicon target magnetron discharge current with varying applied voltage and ICP power. 52
5.4 Magnetron discharge waveform with aluminum target 53
5.5 Effect of the addition of a secondary ICP discharge on magnetron discharge power of silicon and aluminum targets. 54
5.6 Silicon target emission spectrum 55
5.7 Aluminum target emission spectrum 56
5.8 Boltzmann plot of magnetron discharge spectrum 57
5.9 Electron temperature for silicon and aluminum targets at different magnetron discharge voltages. 58
5.10 Time-resolved Langmuir probe measurement of magnetron discharge for silicon target 60
5.11 Time-resolved Langmuir probe measurement of magnetron discharge for aluminum target 61
5.12 Plasma parameters obtained from Langmuir analysis of time resolved curves for a silicon target. 64
5.13 Plasma parameters obtained from Langmuir analysis of time resolved curves for an aluminum target. 65
5.14 Processing of probe data using EMD. 66
5.15 Processed probe signals 67
5.16 Lag time between probe 1 and probes 2 and 3 for a silicon target (a) and aluminum target (b) discharge, determined using cross-correlation. 67
5.17 High speed camera exposure for silicon 69
5.18 High speed camera exposure for aluminum 70
5.19 Silicon target HiPIMS discharge captured by High-speed camera 72
5.20 Reconstructed time evolution of silicon target magnetron discharge. 73
5.21 Average number of spokes observed by high-speed camera during the discharge. 75
5.22 Average spoke brightness during discharge plotted with discharge current. . . 76
5.23 Silicon spoke size distribution for mode 1 and 2 spokes. 78
5.25 Average spoke size and discharge current for aluminum target magnetron discharge. 80
5.26 Magnetron arc during discharge. 81

5.27 Aluminum target surface damage due to arcing. 82

A.1 Magnetron dimensions 90
A.2 Measured emission from calibrated quartz tungsten halogen lamp. 91

List of Abbreviations

ICP	Inductively Coupled Plasma
PVD	Physical Vapour Deposition
HiPIMS	High-powered Impulse Magnetron Sputtering
DC	Direct Current
RF	Radio frequency
IPVD	Ionized Physical Vapour Deposition
OES	Optical Emission Spectroscopy
FEMM	Finite Element Method Magnetics
CAD	Computer-Aided Design
TTL	Transistor-Transistor Logic
CMOS	Complementary Metal-Oxide-Semiconductor
EMD	Empirical Mode Decomposition
IMF	Intrinsic Mode Function
EEMD	Ensemble Empirical Mode Decomposition
CEEMD	Complete Ensemble Empirical Mode Decomposition
NIST	National Institute of Standards and Technology
LTE	Local Thermal Equilibrium

1 Introduction

This project focuses on the characterization of spoke instabilities in ICP enhanced magnetron plasmas. Magnetron sputtering is a widely used physical vapour deposition (PVD) process introduced by J.S. Chapin in 1974 [1]. In a sputtering magnetron, a high negative voltage is applied to the cathode, causing the surrounding gas to breakdown, the resulting ions are accelerated into the cathode at high speeds [1]. The kinetic bombardment of the cathode by ions results in the ejection or "sputtering" of the cathode material, this sputtered material redeposits on a nearby substrate [1]. The result is the synthesis of a high-quality thin film in the nano to micrometer scale [2]. These thin films have applications in semiconductor manufacturing, optical coatings, energy generation and energy storage [1]. However, despite the years of research and industry applications of magnetron sputtering, certain phenomena in the plasma still have not been fully explored [2]. $\mathbf{E} \times \mathbf{B}$ plasma instabilities have been observed in high-power impulse magnetron sputtering (HiPIMS) systems, these instabilities are referred to as spokes, after the name of a similar phenomenon observed in Hall thrusters [3]. Spokes have been studied at the University of Saskatchewan Physics Plasma Labs in a theoretical capacity, but in this project an experimental approach was taken. The goal of this project is to develop a system to produce and study these instabilities. To accomplish this, a custom HiPIMS system was designed, fabricated and its plasma characterized using time-resolved Langmuir probe, floating probes, high-speed camera and optical emission spectroscopy methods.

2 Plasma Physics Background

Plasma is the most common form of matter in the universe and is often referred to as the fourth state of matter [4]. A plasma is a collection of fully or partially ionized gas [1]. Consider the three states of matter commonly seen here on planet Earth: solids, liquids and gases. Heating a solid sufficiently breaks the crystal lattice holding the atoms together, the material then flows as a liquid [5]. Add more heat to a liquid, the atoms vaporize to form a gas [5]. Adding even more heat to the gas, the collisions between atoms become energetic enough to free atomic electrons, this creates a plasma [5]. Plasma is defined as a quasineutral collection of charged and neutral particles that display collective behaviour [4]. Particle interactions in plasma are predominately mediated through long-range electromagnetic forces; this differs from gases where particles interact through collisions [4]. Plasma is found in space in the form of stars, nebulas and the interstellar medium. On Earth, naturally occurring plasma is less prevalent but still found in the ionosphere, aurora and lightning [4]. Artificially generated plasma has broad applications in research and industry. In nuclear fusion research, tokamaks and stellarators use strong magnetic fields to confine high-density and high-temperature plasma to sustain fusion reactions within the plasma [1]. Semiconductor fabrication and materials research uses the process of ion implantation to change the properties of a material, where a plasma is used as an ion source [6]. The glow discharge of plasmas has applications in florescent lighting, plasma displays and atomic emission spectroscopy [1].

2.1 Plasma Temperature

"Thermometers are speedometers for atoms." — Proverb.

Similar to gases, the temperature of a plasma is a measure of the average kinetic energy of particles. The temperature of a plasma affects many properties such as degree of ionization and particle interactions within the plasma, so it is important to understand the definition

of temperature in a plasma. We start with the distribution of particle velocities in thermal equilibrium, which follows a Maxwellian distribution, it is given by the following equation in one dimension [1]

$$f\left(u\right) = A \exp\left(-\frac{mu^2}{2k_B T}\right), \tag{2.1}$$

Where k_B is the Boltzmann's constant, u is the velocity of the particles, m is the mass of each particle, T is the temperature, and A the normalization constant given by [1]

$$A = n\sqrt{\frac{m}{2\pi k_B T}}. \tag{2.2}$$

Equation 2.1 can be generalized to three dimensions by taking the product of the velocity distributions for each spatial dimension and renormalizing, giving the following equation [1]

$$f(\mathbf{u}) = n\left(\frac{m}{2\pi k_B T}\right)^{3/2} \exp\left(\frac{-m(u_x^2 + u_y^2 + u_z^2)}{2k_B T}\right). \tag{2.3}$$

We can write this in terms of speed instead of velocity by using

$$|u| = \sqrt{u_x^2 + u_y^2 + u_z^2}, \tag{2.4}$$

and

$$du_x du_y du_z = u^2 du d\Omega. \tag{2.5}$$

Integrating over all 4π solid angle Ω we get

$$f(u) = 4\pi u^2 n\left(\frac{m}{2\pi k_B T}\right)^{3/2} \exp\left(\frac{-mu^2}{2k_B T}\right). \tag{2.6}$$

The average kinetic energy of the particles is defined as the second moment of this equation [1], which is

$$E_{\text{av}} = \frac{\int_0^\infty \frac{1}{2} mu^2 f\left(u\right) du}{n}, \tag{2.7}$$

$$E_{\text{av}} = \frac{3}{2} k_B T. \tag{2.8}$$

This equation gives us the relation between the average kinetic energy and the temperature of the particles. In plasma physics, temperature is given in terms of energy ($k_B T$) in units of eVs, where $1\,\text{eV} = 11\,600\,\text{K}$ [4]. When talking about the temperature of plasmas we often

have to consider the temperatures ions and electrons separately. Due to the high mobility of electrons, they have much higher temperatures than slow-moving ions [1].

Plasma temperature is important to us because in HiPIMS plasmas, atoms are ionized via electron impact ionization, and the rate of ionization is dependant on electron and neutral densities and their temperatures [1]. In a HiPIMS discharge, electron temperatures of 2.3–7 eV and ion temperatures of 0.05–0.1 eV have been reported [7]. Plasmas can exist in a range of temperatures and densities spanning many orders of magnitude, an example is shown in figure 2.1.

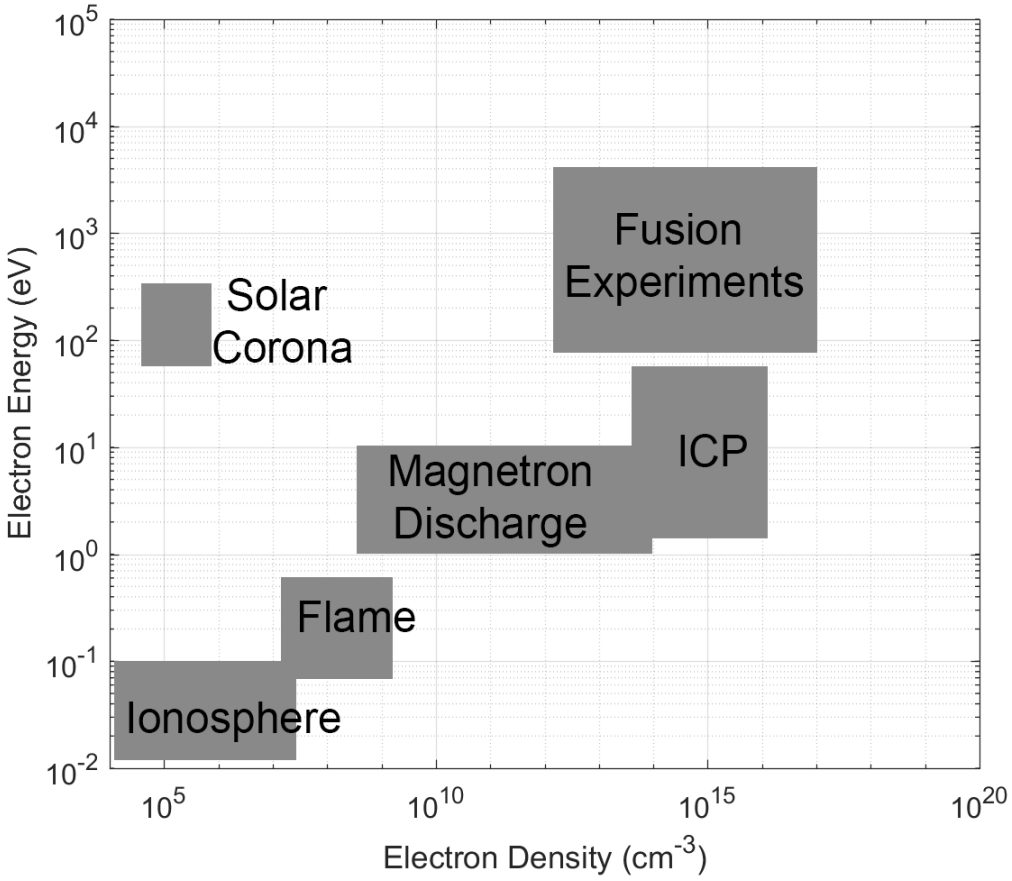

Figure 2.1: Different types of plasmas shown with their temperature and density ranges, adapted from [6].

2.2 Magnetized Plasmas

In the presence of a magnetic field, charged particles in a plasma experience a Lorenz force when moving, this has the effect of limiting movement perpendicular to the field lines and "trapping" the particles. When the magnetic field is strong enough to contain a plasma, the movement of charged particles are limited to along the magnetic field lines. With the degrees of freedom reduced, equation 2.8 becomes [4]

$$E_{av} = \frac{1}{2} k_B T. \tag{2.9}$$

That means in a magnetic field, a single specie of particles can have two temperatures, perpendicular ($T_\perp$) and parallel ($T_\parallel$) to the magnetic field.

Magnetic confinement of plasma occurs naturally in the Van Allen radiation belts in the space near Earth [1]. When charged particles from the sun gets trapped by the Earth's magnetic field their movements are restricted to along the field lines. The magnetic field lines of the Earth converge at the magnetic north and south poles, where the charged particle bombardment is seen in the form of aurora [1].

2.2.1 Gyromotion

Magnetron sputtering systems use radial magnetic fields to trap electrons near the target surface to enhance ionization efficiency, resulting in higher deposition rates. The increased plasma density in front of the target also allows for discharge at a lower background gas pressure. Sputtering at lower pressures allows the sputtered material to travel to the substrate unimpeded by collisions with molecules in the plasma [8]. To trap electrons in front of the target, the magnetic field of the magnetron is configured to be parallel to the target surface, so electrons in the magnetic field experience a Lorentz force [4]

$$\mathbf{F} = q\mathbf{u} \times \mathbf{B}. \tag{2.10}$$

If we consider a magnetic field pointing in the z direction, we can rewrite 2.10 as [4]

$$\begin{aligned}\frac{du_x}{dt} &= u_y \frac{q}{m} B_z, \\ \frac{du_y}{dt} &= -u_x \frac{q}{m} B_z, \\ \frac{du_z}{dt} &= 0.\end{aligned} \tag{2.11}$$

We can differentiate and substitute the first two equations to obtain the following differential equations [4]

$$\begin{aligned}\frac{d^2u_x}{dt^2} &= -\frac{du_x}{dt}\left(\frac{qB_z}{m}\right)^2, \\ \frac{d^2u_y}{dt^2} &= -\frac{du_y}{dt}\left(\frac{qB_z}{m}\right)^2.\end{aligned} \tag{2.12}$$

The solution to these simple harmonic oscillator equations is [4]

$$u_{x,y} = u_\perp \exp\left(\pm i\omega_c t\right). \tag{2.13}$$

Where $u_\perp$ is the constant speed perpendicular to the magnetic field and ω_c is the cyclotron frequency, defined to be [4]

$$\omega_c \equiv \frac{|q|\,B}{m}. \tag{2.14}$$

Here the frequency is chosen to be always positive, so the sign of the charge is denoted in the $\pm$ in equation 2.13 instead. Equation 2.13 describes a circular motion in the x-y plane with frequency ω_c; the radius of that circular motion is the Larmor or gyro radius, defined as [4]

$$r_g \equiv \frac{u_\perp}{\omega_c}. \tag{2.15}$$

Let us calculate the Larmor radius for electrons and argon ions in front of a magnetron target. First, combine equations 2.14 and 2.15 to get

$$r_{ge} = \frac{m_e u_\perp}{|q|\,B}. \tag{2.16}$$

The speed of the electron in a potential difference can be expressed as

$$u_e = \sqrt{\frac{2qV}{m_e}}, \tag{2.17}$$

where V is the potential difference in volts. Combining equations 2.16 and 2.17 gives

$$r_{ge} = \frac{1}{B}\sqrt{\frac{2m_eV}{q}}. \tag{2.18}$$

Similarly, for ions

$$r_{gi} = \frac{1}{B}\sqrt{\frac{2m_iV}{q}}. \tag{2.19}$$

Typical experimental parameters used in this project are

$$B \approx 200G,$$

$$V_{dc} \approx 800V.$$

Substituting these numbers into equation 2.18, the resulting electron gyroradius is 4.8 mm. For singly charged argon ions, equation 2.19 gives a gyroradius of 1.29 meters. This difference in gyroradii between electrons and ions means electrons are trapped by the magnetic field while ions can pass through mostly unimpeded and collide with the target. In this case, the trajectories of the electrons are dominated by magnetic forces and therefore the electrons are "magnetised". On the other hand, the trajectories of the ions are dominated by collisions, not magnetic forces, so they are "unmagnetised".

2.2.2 $\mathbf{E} \times \mathbf{B}$ drift

The trapped electrons near the magnetron experiences several different drifts due to: the gradient of the magnetic field, the pressure gradient, the magnetic field curvature and most importantly for this study, $\mathbf{E} \times \mathbf{B}$ drift [7]. $\mathbf{E} \times \mathbf{B}$ drift is a combination of the circular orbit shown above, and a linear motion of the guiding centre in the $\mathbf{E} \times \mathbf{B}$ direction. The motion of the guiding centre is given by [1]

$$\mathbf{u}_E = \frac{\mathbf{E} \times \mathbf{B}}{\mathbf{B}^2}. \tag{2.20}$$

Note that this equation does not depend on mass or charge, meaning electrons and ions experience the same drift of their guiding centres. This cycloid motion is shown graphically in figure 2.2.

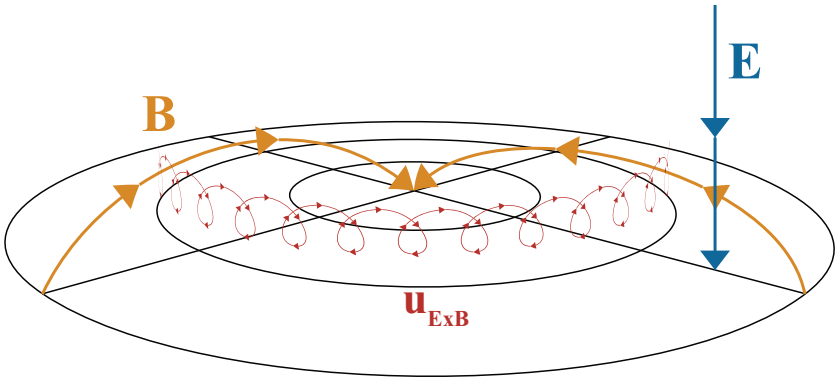

Figure 2.2: $\mathbf{E} \times \mathbf{B}$ drift of a negatively charged particle in the space above a circular magnetron target. Here, the particle gyrates in a clockwise circular motion while the centre of gyration drift clockwise around the circular target. A positive charged particle would gyrate in a counterclockwise motion but its centre of gyration would experience the same drift as the negative particle.

2.2.3 Transport Across Magnetic Fields

A charged particle trapped by magnetic fields experience collisions, these collisions change its guiding centre and allow the particle to diffuse across the magnetic field lines. This random process is described theoretically by the following equation [6]

$$D_{\perp} = \frac{k_B T \tau_m}{m \left(\omega_c \tau_m\right)^2}, \tag{2.21}$$

where $D_{\perp}$ is the diffusion coefficient perpendicular to the magnetic field with units of m^2/s, τ_m is the average time between collisions, m is the mass of the diffusing particle and ω_c is the cyclotron frequency. $\omega_c \tau_m$ is the Hall parameter and it is an important measure of magnetic confinement [1]. When $\omega_c \tau_m >> 1$ (stronger magnetic field, higher cyclotron frequency, smaller gyro radius, less collisions), the diffusion of charged particles across field lines is severely impeded. Recalling the definition of ω_c from 2.14, we rewrite the equation as

$$D_{\perp} = \frac{m k_B T}{\tau_m q^2 B^2}. \tag{2.22}$$

Here we can see that theory predicts $D_{\perp}$ to be proportional to $1/B^2$, but experimental results showed in most circumstances, $D_{\perp}$ is proportional to $1/B$ instead [1]. This lead to the proposal of an semi-empirical diffusion coefficient by Bohm [4]

$$D_{\mathrm{Bohm}} = \frac{1}{16} \frac{k_B T}{qB}. \tag{2.23}$$

The value of the Hall parameter has been determined experimentally for dc magnetrons to be around 16, which is consistent with Bohm diffusion [3]. However, for HiPIMS discharges, the measured Hall parameter is in the range of 2-5, this increased electron diffusion across field lines is known as anomalous diffusion [3].

2.2.4 Plasma Spokes

Spokes are localized plasma inhomogeneities in high-powered $\mathbf{E}\times\mathbf{B}$ discharges, first observed in Hall thrusters [9]. An example of the shape of a triangular spoke above radial magnetron is shown in figure 2.3. It has been shown experimentally that spokes are a mechanism for cross-field diffusion, resulting in diffusion rates 5 times higher than Bohm diffusion [10]. For HiPIMS discharges, spokes have been observed above the target, moving with velocities in the range of 6.5–10 km/s, rotating in the $\mathbf{E}\times\mathbf{B}$ direction as well as the $-\mathbf{E}\times\mathbf{B}$ depending on the discharge conditions [11, 7]. The apparent motion of the spokes is a phase phenomenon not a group phenomenon, which means the motion corresponds to the motion of the ionization zones, not the plasma itself [7]. The number of spokes observed, also known as the the mode number of the spoke, has been shown to be correlated to the discharge power [7]. For HiPIMS discharges, stochastic spokes were observed for powers around 25 $\mathrm{W/cm^2}$, and as the power is increased, mode numbers of four to five are observed; spokes have been observed to evolve, merge and split during the discharge [11, 3]. The mode number decreases with further increases of power until the plasma is homogeneous [3]. The shape of the spoke has been related to the secondary electron production and the properties of the target material [12]. Various attempts have been made to explain or predict the behaviour of spokes, however, contradictory experimental results have been observed, indicating that the spoke phenomenon is heavily dependent on experimental conditions [13]. For this project we characterize the spokes observed in a custom fabricated magnetron.

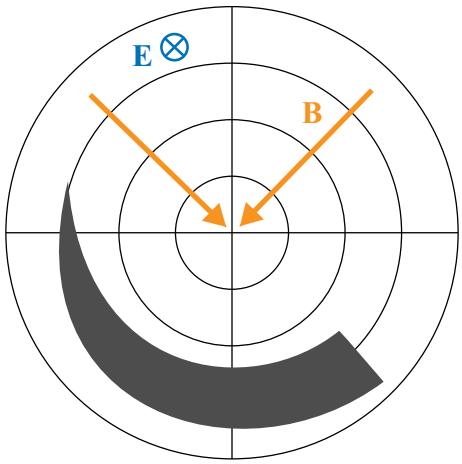

Figure 2.3: The shape of a single triangular spoke above a radial magnetron.

2.3 Plasma Generation

As the plasma in our test chamber loses energy to the chamber walls, a constant input of power is needed to maintain a plasma discharge and keep the ions and electrons from recombining. In this project we have two plasma sources, the magnetron and the inductively coupled plasma (ICP). In this section we will discuss the background behind the operating principle of these two sources.

2.3.1 Magnetron Plasma Source

The sputtering process uses ionized gas atoms to strike a biased target, the impact of the energetic ions causes ejection of the target material which redeposits on a nearby substrate as a thin film [7]. Early sputtering methods operated using a DC powered discharge between a planar anode and cathode without an external magnetic field [1]. The ion impacts at the cathode ejects sputter material and creates secondary electrons [7]. The secondary electrons are the main driving force of the discharge as they are responsible for ionizing the background gas, leading to continued sputtering [1]. At low pressures, electrons generated from the discharge are quickly lost to the chamber walls before colliding and ionizing a gas molecule [1]. At higher pressures, there are more chances for collision, therefore, the ionization efficiency increases with pressure [7]. However, increased pressure leads to a decrease in the mean free path of sputtered material in the plasma, and deflection of these particles leads to

lower quality film and lower deposition rates [1]. The introduction of a magnetic circuit in the magnetron sputtering process mitigates these problems. Magnets are placed behind the target, and as ions bombard the target, emitted secondary electrons are trapped by the magnetic field in a closed $\mathbf{E} \times \mathbf{B}$ drift near the target surface, enhancing ionization. A simplified diagram of the magnetron sputtering process is shown in figure 2.4 with argon as the background gas. Argon is often used as sputtering gas due to its relative high atomic mass, low cost and low reactivity [14]. The properties and cost of potential sputtering gases are shown in table 2.1 for comparison.

Table 2.1: Atomic properties and costs of sputtering background gases [15]. Nitrogen and oxygen occur as diatomic molecules (N_2 and O_2), their molecular properties are the values in brackets.

Symbol	Standard atomic weight	Ionization energy (eV)	Price (USD/kg)
He	4.003	24.5874	24 [16]
N	14.007 (28.013)	14.5341 (15.581)	0.14 [17]
O	15.999 (31.999)	13.6181 (12.0697)	0.15 [17]
Ne	20.180	21.5645	240 [18]
Ar	39.948	15.7596	0.931 [19]
Kr	83.798	13.9996	290 [18]
Xe	131.293	12.1298	1800 [18]

We see the importance of atomic mass when we consider the energy transfer between two particles in an elastic collision, which is given by the equation

$$\frac{E_t}{E_i} = \frac{4M_tM_i}{(M_i + M_t)^2}. \tag{2.24}$$

Maximum energy transfer occurs when the mass of the incident particle M_i is equal to the mass of the target particle M_t. Therefore, matching the atomic masses of the sputter gas and target increases sputtering efficiency.

The magnetic configuration of radial magnetrons is comprised of one pole of the magnet at the centre of the circular target and the opposite pole in a ring around the outside. In a conventional balanced magnetron configuration, the strengths of the inner and outer

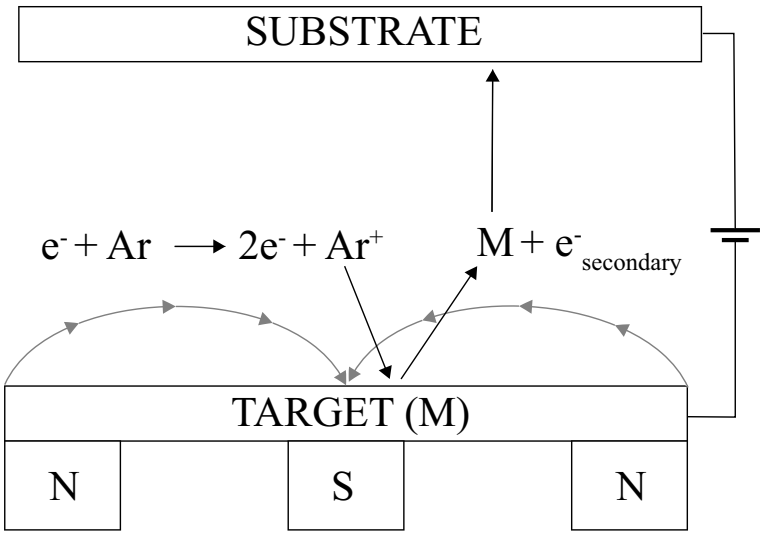

Figure 2.4: Simplified process of magnetron sputtering. Here, neutral argon gas is ionized by energised electrons, the argon ions then collide with the biased target to eject target ions and secondary electrons.

magnets are balanced such that the magnetic field lines are closed, i.e. most field lines from the outer magnet pass through the centre magnet [2], see figure 2.5. This leads to a region of dense plasma confined in front of the target and lower ion flux to the substrate, this is suitable for sputtering temperature sensitive substrates [2]. Type-1 unbalanced magnetrons have a stronger centre magnet. This configuration results in some magnetic field lines being directed toward the chamber walls and leads to lower plasma density and ion current at the substrate [2]. In a type-2 unbalanced magnetron, the strength of the outer magnets is increased, resulting in magnetic field lines that extend towards the substrate, the resulting plasma in front of the target is less confined and some secondary electrons are able to flow towards the substrate [2]. Consequently, the ion current at the substrate is increased by approximately an order of magnitude [2]. The magnetic configuration of type-2 unbalanced magnetrons make them an excellent ion source [2]. Figure 2.5 shows the magnetic field lines of all three types of magnetic configurations. A picture of the magnetron plasma studied in this project is shown in figure 3.6 in section 3.1. There, the forward extension of the bulk plasma, typical of type-2 unbalanced magnetrons is clearly visible.

A common problem faced in magnetron sputtering are arc discharges. Arcing can oc-

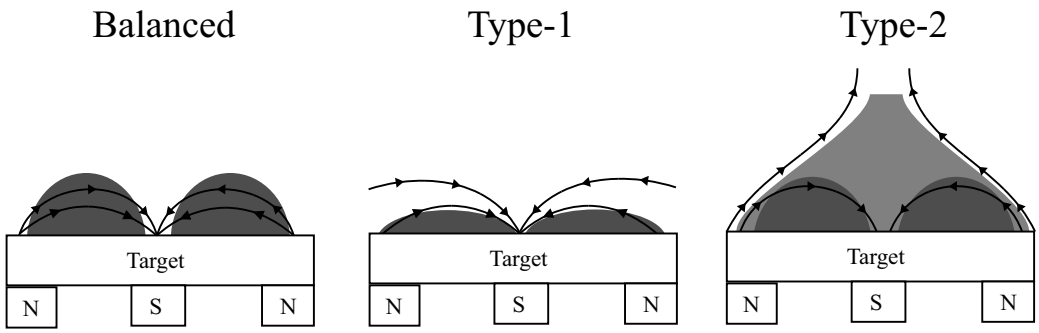

Figure 2.5: Magnetic field lines and plasma confinement of three types of magnetron magnetic configurations.

cur when working with high-power, or reactive sputtering. Arc discharges can be classified into two types, thermionic and cathodic arcs, both of which involve collective electron emission [20]. Thermionic arcs occur when the temperature of the target surface is high, and the thermal energy of the electrons allow them to overcome the work function and escape the surface. The work function of the target surface is lowered due to the applied electric field, increasing thermionic emissions though a process called the Schottky effect [20]. Cathodic arcs do not require high-temperatures to occur, instead, arcs occur when current density on the target reaches $10^{12}\,\mathrm{A/m^2}$ [20]. In cathodic arcs, a large number of electrons overcome the potential barrier causing a micro-explosion that ejects macroparticles from the target surface, the macroparticles can deposit on the substrate and result in defects in the thin film growth [20]. The surface conditions of the target play an important role in the ignition of cathodic discharges. Surface defects on the target such as scratches or dust can enhance the local electric field to many times the average [20]. The locally enhanced electric field leads to a higher field emission current which leads to higher local temperatures. The temperature increases until it reaches the boiling point of the target material resulting in an arc event and the destruction of the spot. Furthermore, when using metal targets, the target material can react with atmospheric oxygen during installation. This causes an oxide layer to form on the surface. Most of the applied voltage drops within the insulating layer, which results in decreased ion bombardment and increased growth of the insulating layer. High electric field strength can cause dielectric break down of the insulating layer resulting in arc events. Con-

trary to the collective electron emissions in arc discharge events, normal magnetron operation requires glow discharge, which emits electrons in individual events.

Magnetron arcing can be reduced by keeping the target surface free from contaminates or defects, using pulsed bias or reversing the bias to prevent charge buildup or using power supplies that can detect arc events and reduce the power or reverse polarity [20]. DC bias is most commonly used for magnetron sputtering due to its low complexity and cost, however, it can only be used with conductive materials. In contrast, RF bias can sputter metal as well as dielectric materials. The disadvantage of RF is it requires a more costly power supply and an impedance matching network to ensure maximal power transfer to the plasma [2]. By applying a pulsed DC bias to the target, one can drastically increase the capabilities of the DC magnetron. A pulsed bias can be used to prevent overheating while sputtering temperature-sensitive materials. Pulsed magnetron sputtering at frequencies around 10–200 kHz has been shown to reduce arcing and produce higher quality thin films. Charge build up on the target can be dissipated by reversing the polarity of the target to around 10–20 % of the operating voltage during the pulse-off period [2]. Dependent on the conditions, arcing was sometimes observed in our custom magnetron. Excessive arcing was observed at high discharge powers and damaged the target surface, this is discussed further in section 5.6.

2.3.2 High-Power Impulse Magnetron Sputtering

HiPIMS is defined as a form of pulsed magnetron sputtering, where the peak power density is two orders of magnitude greater than the time averaged power [7]. HiPIMS operates at 500–2000 V, peak power densities of 0.5–10 kW/m and a pulse of 50–5000 Hz at a duty cycle of 0.5–5 % [7]. The discharge produces a high-density plasma above the target surface that can reach densities of $10^{19}/m^3$ [7]. HiPIMS utilizes the same magnetic circuit setup as a conventional DC magnetron, the only difference being the power supply. HiPIMS generally experiences lower sputter rates than conventional DC magnetrons at the same average power [7]. One of the factors is because the sputtered material are becoming ionized in the discharge and returning to the target due to the applied bias [7]. The returning ionized sputter material can eject more material on impact, leading to a phenomenon called self-sputtering, where it is possible to sustain sputtering without utilizing the background gas [7]. The effect of

self-sputtering on the discharge current is shown in figure 2.6. Here, each curve corresponds to a discharge with a different self-sputtering parameter Π_{ss}, which is defined as [21]

$$\Pi_{ss} \equiv \alpha\beta\gamma_{ss}, \tag{2.25}$$

where α is the ionization probability of the sputtered ion, β probability that the ions return to the target and γ_{ss} is the self-sputter yield. $\Pi_{ss} = 1$ is the threshold for sustained self-sputtering and $\Pi_{ss} > 1$ results in self-sputtering runaway [21].

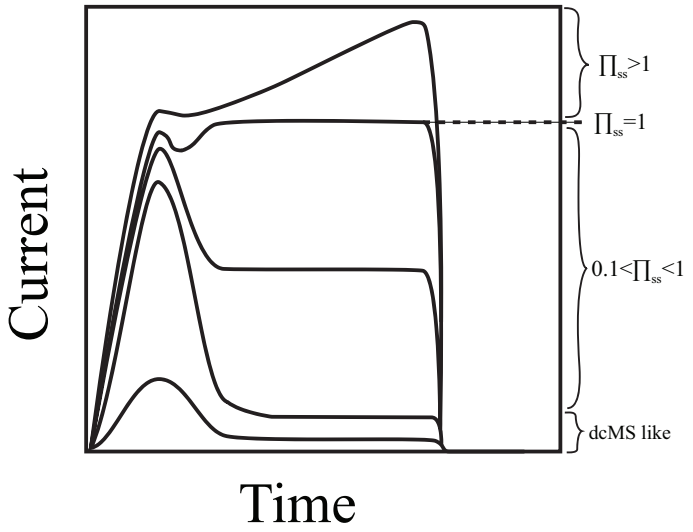

Figure 2.6: HiPIMS discharge current curve with varying values of self-sputtering parameter Π_{ss}, adapted from [7]. The first peak, represents the sputtering process as dominated by the background gas, as this gas is depleted through gas rarefaction, the discharge current decreases. The second peak is caused by self-sputtered ions returning to the target. The prominence of the second peak depends on the self-sputtering parameter Π_{ss}.

Another factor that reduces the deposition rate of HiPIMS is gas rarefaction. As the sputtered material collides with the background gas, the gas around the cathode gets heated and expands. This results in lower density of background gas around the discharge, which leads to lower sputter and deposition rates [7].

The highly ionized and dense plasma produced in a HiPIMS discharge differs from conventional DC magnetron discharge in that it is an ionized physical vapour deposition (IPVD) plasma, where the ion flux is greater than the neutral flux at the substrate. The ionization of sputtering material in IPVD has certain benefits for the film quality. The increased ion

current at the substrate increases the mobility and reactivity of the condensate and increases the temperature of the substrate. Certain high-quality films can only be achieved at a sufficiently high substrate temperature [22]. Furthermore, high rates of ionization lead to denser films with better adhesion to the substrate. In conventional DC magnetron sputtering, the sputter material is neutral and difficult to control, whereas in IPVD ions are accelerated and collimated by the sheath towards the substrate, this increases deposition rates in deep trenches and other surface features [22]. A bias can be applied to the substrate to control the ion flux and incident energy on the substrate. Unbalanced magnetrons and HiPIMS are both methods of increasing ion deposition at the substrate. Another method to increase ionization in the sputtering process is though a secondary discharge in addition to the magnetron discharge.

2.3.3 Inductively Coupled Plasma

An inductively coupled plasma (ICP) is created by injecting RF power into coils which produces an oscillating magnetic field, this gives rise to an electric field described by Faraday's law of induction [6]. Electrons in the gas are accelerated by the electric field, the collision between the energetic electrons and atoms leads to ionization which drives the discharge [1, 6]. This inductive coupling between the power source and the plasma is known as H-mode, however, at low-powers, ICPs operate in a capacitively coupled mode known as E-mode [6]. In this case, the electric charge in the coils create an electric field as described by Gauss's law and electrons are accelerated by this field [6]. For this project, the ICP was operated in H-mode at 200 W.

The ICP system can be thought of as a transformer with an N turn primary coil corresponding to the RF coils, and an one turn secondary coil corresponding to the plasma [23]. The plasma has inductive properties that correspond to the state of the plasma, therefore an impedance matching circuit is required to facilitate efficient energy transfer into the plasma. The coil transmits RF power into the vacuum chamber through a quartz window, quartz is used due to the low dielectric loss and low dielectric constant of the material. A simplified diagram of an ICP system is shown in figure 2.7. ICPs are capable of achieving high plasma densities ($1\text{–}3 \times 10^{17}\,\mathrm{m}^{-3}$) in low pressure discharges (0.83–15 mtorr), allowing for

magnetrons to operate at lower pressures [1]. ICP assisted magnetron discharges have been shown to enhance ionization of the sputtered species, reduce arcing in the magnetron and produce higher quality depositions in terms of homogeneity [24]. The combination of ICPs and magnetrons is widely used in the semiconductor industry for the deposition of metal for pads, vias, and contacts [7]. In this project, ICP was used as a secondary discharge along with the magnetron discharge, this is to explore how the ICP affects the spokes in the discharge.

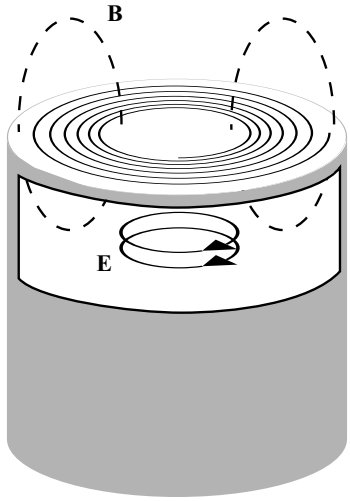

Figure 2.7: Simplified diagram of inductive coils on top of chamber, generating ICP in H-mode. Adapted from [23].

2.4 Plasma Characterization Techniques

In this section I present theoretical background for the plasma characterization techniques used in this project.

2.4.1 Langmuir Probe Theory

The simplest way to measure the properties of a plasma is using a Langmuir probe. A Langmuir probe consists of an electrode placed inside the plasma, by applying different voltages to the electrode and observing the current collected, properties of the plasma such as electron temperature, density and plasma potential can be obtained from the analysis of the I-V curve. An example of a Langmuir probe I-V curve is shown in figure 2.8.

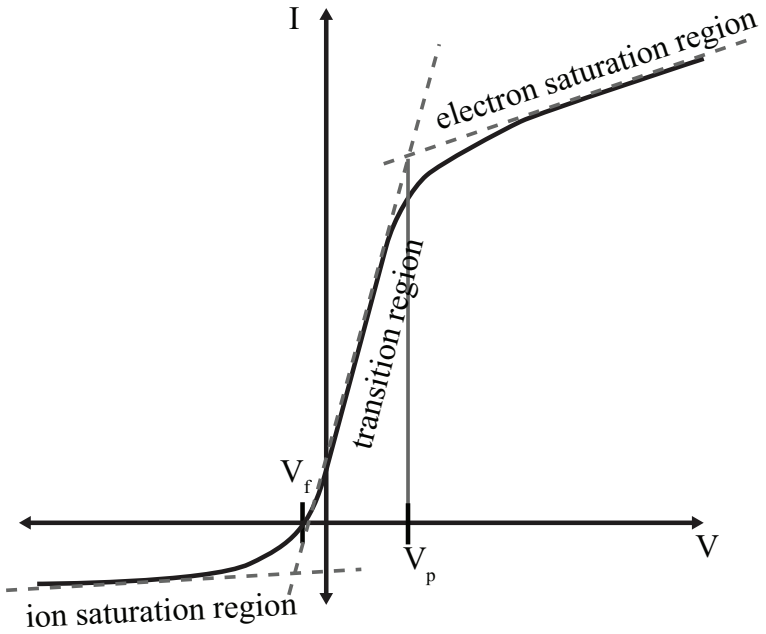

Figure 2.8: Theoretical I-V curve of a Langmuir probe. As the applied voltage scans from negative to positive the probe collects current from the ion then electrons until saturation, adapted from [25].

When the voltage applied to the probe is negative, the electrons are repelled, and the probe collects ion current, when the voltage is positive, the probe collects electron current. Due to the higher mobility of electrons, electron current is much higher than ion current. In

an argon plasma, the electron saturation is around > 200 times more than the ion saturation current [25]. Between the electron and ion saturation regions is the transition region. If the electrons follow a Maxwellian distribution, the current in the transition region will be exponential with respect to the applied voltage, given by [25]

$$I_e = I_{es} \exp\left[e\left(V_{probe} - V_{plasma}\right)/k_B T_e\right], \tag{2.26}$$

where V_{probe} is the potential applied to the probe, V_{plasma} is the plasma potential, e is the charge of an electron and I_{es} is the electron saturation current given by [25]

$$I_{es} = eAn_e\frac{u}{4}. \tag{2.27}$$

Where u is the mean thermal speed for electrons modelled as a Maxwell-Boltzmann distributed gas with temperature T_e given by

$$u = \sqrt{\frac{8}{\pi}\frac{kT_e}{m_e}}. \tag{2.28}$$

The factor of $\frac{1}{4}$ in equation 2.27 comes from the integrating the Maxwell-Boltzmann distribution for all electrons traveling towards the probe and A is the area of the probe tip collecting the current. The electron temperature is obtained by taking the natural logarithm of equation 2.26, the result is a line with a slope of $1/T_e$. Once the electron temperature is found, it can be used to find the thermal velocity u of the electrons, which can be substituted into equation 2.27 to find the electron density.

On the other end of the I-V curve, we find the ion saturation current. Ions entering the sheath of the Langmuir probe has velocity [4]

$$u_0 \geq \sqrt{\frac{k_B T_e}{M}}, \tag{2.29}$$

where M is the mass of the ions, this is known as the Bohm criterion. The Bohm current collected by a negatively biased probe is given by [4]

$$I_{Bohm} = 0.61 n_i e A u_0, \tag{2.30}$$

where n_i is the ion density and A is the area of the probe. Using the electron temperature obtained in the previous steps in equation 2.29 and the measured ion saturation current, the

ion density can be obtained. Here we are assuming the characteristic length of the plasma, or Debye length is much smaller than the dimensions of the probe, this way the area of the probe is approximately the area of the sheath around it. We can confirm this by calculating the Debye length given by [1]

$$\lambda_{Debye} = \sqrt{\frac{k_B T_e}{4\pi n_e e^2}}. \tag{2.31}$$

Using values expected for an HiPIMS plasma: $T_e = 0.3\,\text{eV}$ and $n_e = 10 \times 10^9/\text{cm}^3$ [7], we find the Debye length to be 40 µm. This is orders of magnitudes smaller than our probe tip, which is on the scale of centimeters.

One of factors in this project that can reduce the accuracy of the probe measurement and analysis is the magnetron magnetic field. As discussed previously, the presence of magnetic fields in the plasma can limit charged particle mobility; limited electron mobility reduces the electron saturation current of the probe and rounds off the edge between the transition and electron saturation regions. In this project, magnetization of the plasma occurs in the region directly in front of the magnetron target. For our measurements, the Langmuir probe tip was placed 8 cm from surface of the of the magnetron target, the magnetic field strength at this location is 35 mT, assuming a minimum electron temperature of 0.3 eV(value taken from [7]). We find the electron gyroradius using equations 2.17 and 2.18 to be ∼0.55 m. This value is much bigger than the size of our Langmuir probe and therefore we can ignore the effects of the magnetic field for our analysis.

2.4.2 Optical Emission Spectroscopy

Optical emission spectroscopy (OES) is a non-invasive plasma diagnostic method used to determine electron density, temperature and types of particles in the plasma. Plasmas can emit light through a variety of different processes, of particular interest here is spontaneous emission. Spontaneous emission occurs as electrons transition from a higher energy level to a lower energy level, the difference in energy is released as a photon, this produces a spectrum that is characteristic to the emitting atom. By comparing the observed spectrum to known spectra, the species in the plasma can be identified [26]. Furthermore, the intensity of the emission lines can provide information on the electron temperature in the plasma. To obtain

the temperature, first consider the energy emitted by a spectral line given by [26]

$$\epsilon_{ij} = \frac{h\nu_{ij}}{4\pi} A_{ij} N_j, \tag{2.32}$$

where h is Planck's constant, ν_{ij} is the freqency of the photon emitted during a transition between levels i and j, A_{ij} is the transition probability and N_j is the density of the excited state. ϵ_{ij} is known as the emission coefficient and has units of energy/(time $\times$ volume $\times$ solid angle). This equation assumes an optically thin plasma, meaning the emitted light is not reabsorbed [26]. Assuming the the populations at both levels are at local thermodynamic equilibrium, the density of the excited energy level can be written as a function of temperature using the Boltzmann equation [27]

$$\frac{N_j}{N} = \frac{g_j}{U(T)} \exp\left(- \frac{E_j}{k_B T} \right). \tag{2.33}$$

Where $U(T)$ is the partition function, g_j is the statistical weight, E_j is the energy of the level, k_B is the Boltzmann's constant and T is the temperature. Combining equations 2.33 and 2.32 gives [28]

$$\epsilon_{ij} = \frac{hcA_{ij} g_j N}{\lambda_{ij} U(T)} \exp\left(\frac{E_j}{k_B T} \right) . \tag{2.34}$$

The peak ratio method takes the ratio of two spectral lines, so some terms in equation 2.34 cancel out, leaving ϵ_i/ϵ_j as a function of temperature

$$\frac{\epsilon_i}{\epsilon_j} = \frac{g_i A_i \lambda_j}{g_j A_j \lambda_i} \exp\left(- \frac{E_i - E_j}{k_B T} \right). \tag{2.35}$$

The transition probability A, statistical weight g and energy of the excited state E of most species can be found in preexisting databases, with this we can solve equation 2.35 for the electron temperature of the plasma. The accuracy of the peak ratio method can be improved by observing multiple lines. We can rearrange equation 2.34 such that

$$\frac{\lambda_{ij}\epsilon_{ij}}{hcA_{ij}g_j} = \frac{N}{U(T)} \exp\left(- \frac{E_j}{k_B T} \right), \tag{2.36}$$

and take the natural log of both sides

$$\ln\left(\frac{\lambda_{ij}\epsilon_{ij}}{hcA_{ij}g_j} \right) = -\frac{1}{k_B T} E_j + \ln\left(\frac{N}{U(T)} \right). \tag{2.37}$$

Plotting the left hand side as a function of E_j gives a linear line in the form of $y = mx + b$, where $m = -1/k_B T$. The resulting plot is known as a Boltzmann plot and its slope is used to find the electron temperature [28].

2.4.3 Morphological Image Processing

A high-speed camera was used to capture images of the spokes during the discharge, these images provide important information on the mode number, size, and shape of the spokes. Image processing techniques were used to process the high-speed camera data, here, I present a short introduction to the fundamentals of image processing.

In mathematical morphology, a structuring element (sometimes called kernel) is a shape that is used to interact with an image, it consists of a pattern defined around an origin. The shape and size of the pattern is chosen depending on the application. Figure 2.9 shows three examples of structuring elements.

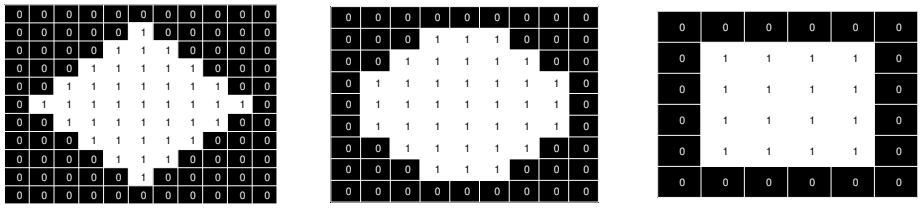

(a) **(b)** **(c)**

Figure 2.9: Examples of structuring element shapes: (a) diamond, (b) disk, (c) square. White squares represents the on or foreground pixels and black squares represents the off or background pixels.

When using a structuring elements in a morphological operation, the origin of the structuring element scans over every pixel in an image, the pixel values of the image is then compared to the pixel value of the structuring element and the results depend on the type of morphological operation being carried out.

Two fundamental morphological operations are dilation $\oplus$ and erosion $\ominus$. To carry out a dilation, the origin of the structuring element is superimposed on each pixel in the image, which is taken as the input pixel. For each input pixel, check the values of its neighbouring pixels as dictated by the shape and size of the superimposed structuring element, if at least one pixel in neighbourhood is on then the input pixel is turned on, if no pixels are on, then the input pixel is left off. This leads to a 'dilation' or growth of the foreground pixels. The process for erosion is similar, the rules are, if at least one pixel in the neighbourhood is off, then the input pixel is turned off. The effects of dilation and erosion are shown in figure 2.10.

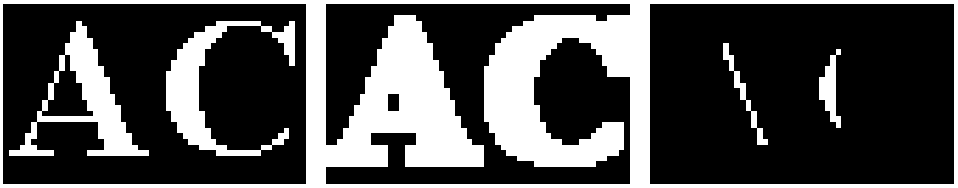

(a) **(b)** **(c)**

Figure 2.10: Example of morphological operations performed on an image using a 4x4 square structuring element. (a) original image, (b) dilation, (c) erosion

Opening and closing are compound morphological operations composed of dilation and erosion. Opening is an erosion followed by a dilation, the opening of image X by structuring element K is written as $X \circ K = (X \ominus K) \oplus K$. The first erosion removes small objects in the image, the following dilation restores the surviving objects to their original size. Opening is useful for opening gaps and removing small objects. Closing is a dilation followed by an erosion, written as $X \bullet K = (X \oplus K) \ominus K$. Closing is useful for filling in holes and gaps in the image.

Using a combination of these functions, the images of the plasma were processed and areas of interest identified, this process is discussed in further detail in section 4.4.

3 Experiment

The HiPIMS system was custom designed and machined for this project. In this chapter I discuss my design process for the magnetron and the characterization methods used.

3.1 HiPIMS Design

The magnetic field of the magnetron is created by two N42 grade neodymium magnets configured as follows: one 1/2" (1.27 cm) cylindrical button magnet is placed in the center of a ring magnet having an inner diameter of 1" (2.54 cm) and outer diameter of 2" (5.08 cm). The peak magnetic field strength as measured by a gaussmeter is ∼2.8 kG. The two magnets are the same grade, which means they have the same magnetic flux output per unit volume. Since the centre magnet is smaller than the outer ring magnet, some of the field lines from the outer magnet do not pass through the centre, rather they extend off towards the substrate forming a type-2 unbalanced magnetron. A cross-section of the magnetron assembly is shown in figure 3.1.

The biased stand is mounted on a copper power feedthrough that is connected to the high-voltage pulse modulator which provides the high-voltage bias needed for the magnetron discharge. The biased assembly is electrically isolated from the chamber walls and the ground shield. As shown in figure 3.1, the target is mounted in front of the magnets and held in place using screws and washers. Boron doped silicon wafers obtained from Silicon Materials Inc and polished commercial aluminum sheet metal were used as targets in this project. These two materials were chosen because silicon and aluminum sputtering are both widely used in nanofabrication. The ground shield is attached to the magnetic housing with three insulating Teflon bolts. A circular opening allows for the ions to sputter the target, but no biased stainless-steel surface is exposed. The ground shield is connected to the chamber walls through a copper ribbon. The different parts of the magnetron with their electrical biases

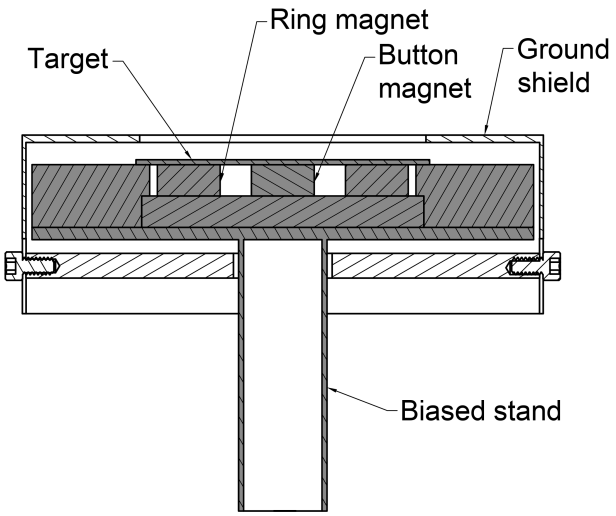

Figure 3.1: Cross-section of magnetron. The configuration is radially symmetric along the centre vertical axis. The grey hatched areas indicates biased components while the white hatched areas are grounded.

are shown in figure 3.2.

In the first iteration of the design, the magnetic housing was made from 304 grade stainless-steel, which is not ferromagnetic. The magnetic field lines of this first iteration is shown in figure 3.3 (a). The magnetic field lines behind the target confined energetic electrons and caused an unwanted discharge in the cavity between the ground shield and the target. This discharge resulted in the sputtering of stainless-steel onto the insulating bolts (Figure 3.4), and also made it difficult to achieve a discharge in front of the target area. This problem was resolved by machining a base plate for the magnets using 17-4 PH, a ferromagnetic grade of stainless-steel. This reduced the magnetic field intensity behind the target, see figure 3.3 (b). The magnetic field of the magnetron with the 17-f PH base was measured using a Gaussmeter and compared with the simulated results from Finite Element Method Magnetics (FEMM), see figure 3.5.

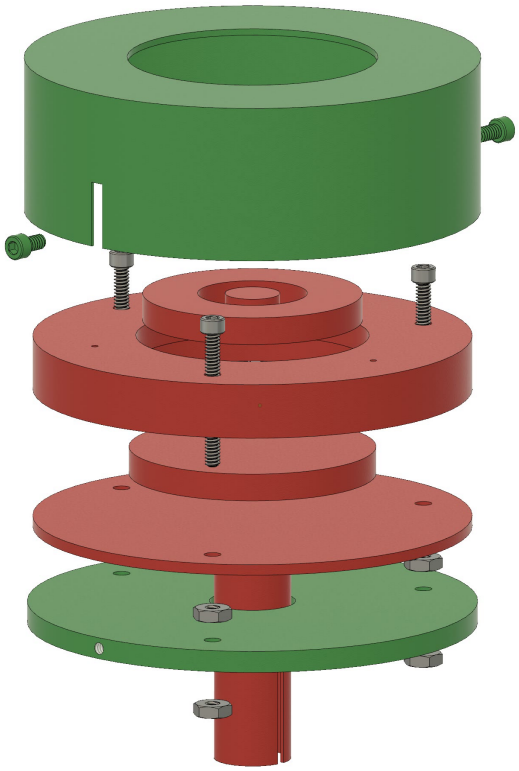

Figure 3.2: Exploded isometric view of magnetron assembly. Red are high-voltage biased components, green are grounded, grey are the insulating nuts and bolts.

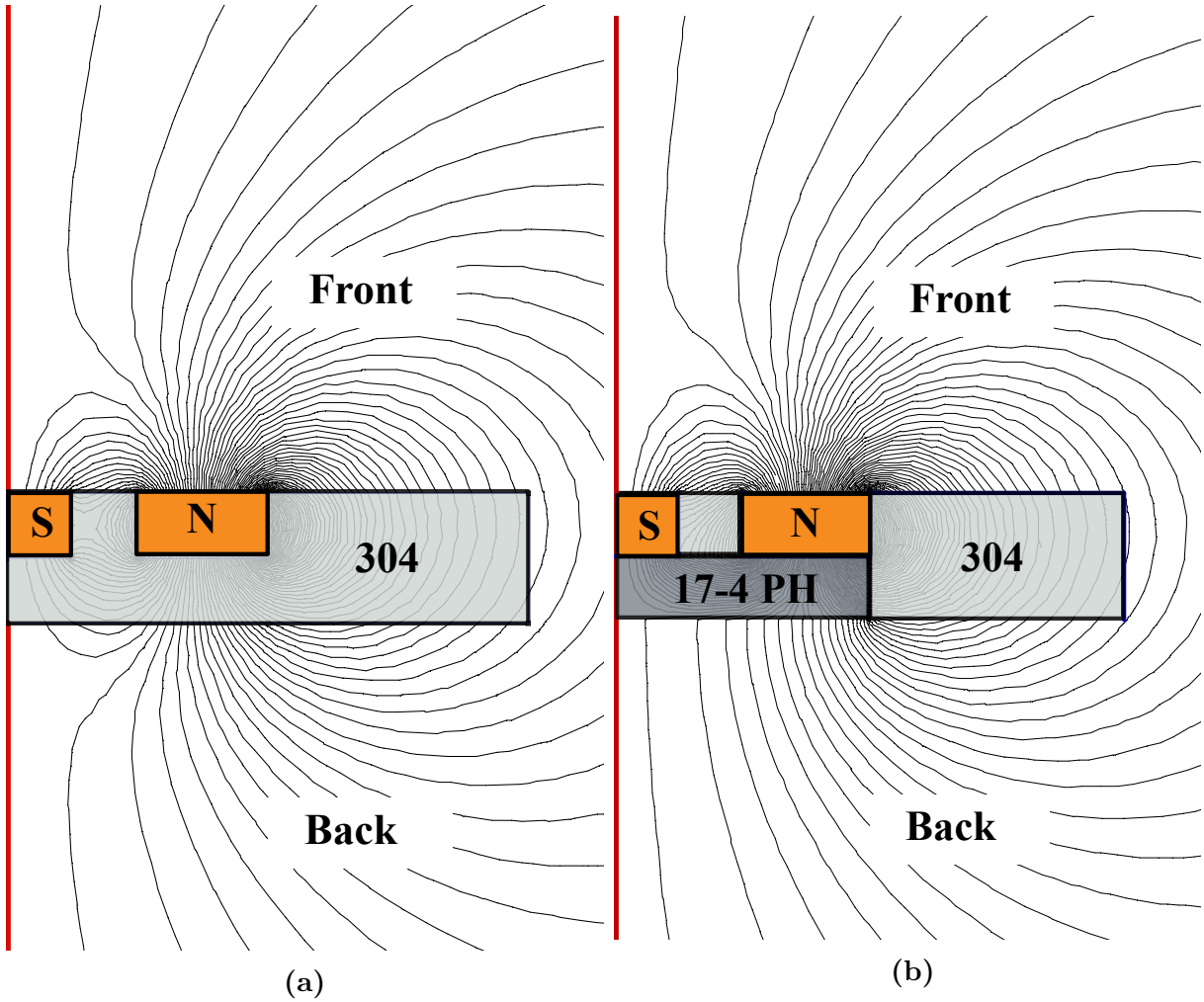

Figure 3.3: (a) Magnetic field lines of magnetron with 304 stainless-steel housing, (b) Magnetic field lines of new magnetic housing. The left hand edge is the axis of radial symmetry. The magnets sit on a plate of 17-4 PH stainless-steel, this reduces the magnetic field intensity behind the target area. Simulated using FEMM [29].

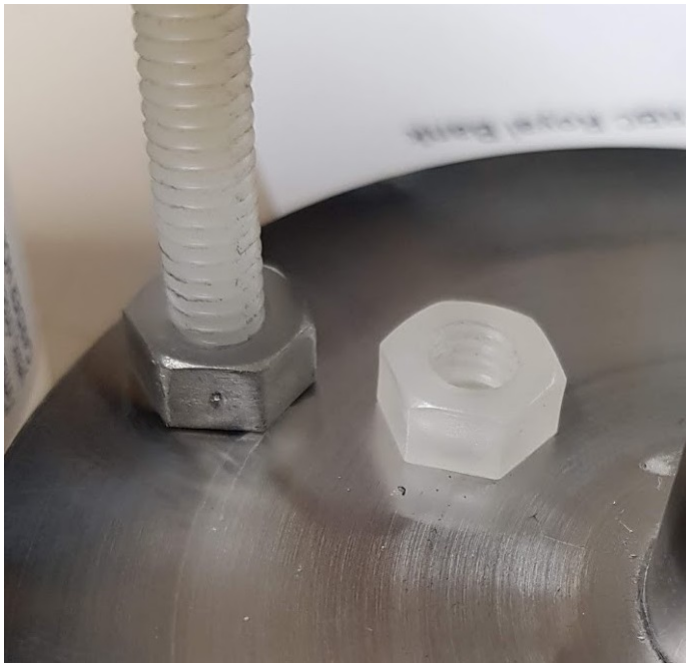

Figure 3.4: Teflon bolt sputtered with stainless-steel (left), normal Teflon bolt (right).

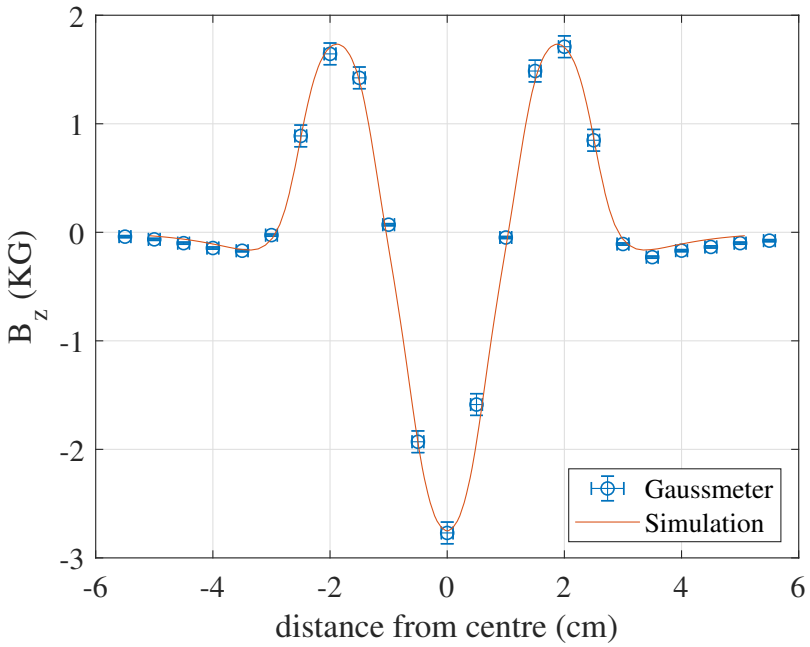

Figure 3.5: Magnetic field strength normal to target surface, 4 mm above target. With 17-4 PH ferromagnetic stainless-steel base. The magnetic flux was measured using a Gauss meter with a ruler to determine the radial position.

The computer-aided design (CAD) model of the magnetron assembly was designed in Autodesk Fusion 360. The permanent magnets were acquired from K&J magnetics and the stainless steel components were machined by the University of Saskatchewan physics machine shop. The magnetron was biased using a custom solid state high power modulator built by a previous student and subsequently modified [30]. The pulser is an IGBT-switched Marx generator with an 1:10 radar transformer, it is capable of providing a capacitive discharge up to 2 kV peak voltage with a max pulse duration of 200 µs at 270 Hz, experiments were carried out using a 800 V and 100 µs long pulse. The voltage from the pulse modulator was measured using a Tektronix P6015A high-voltage probe, current draw by the magnetron was measured using a Model 150 Pearson current monitor. A picture of the magnetron discharge is shown in figure 3.6.

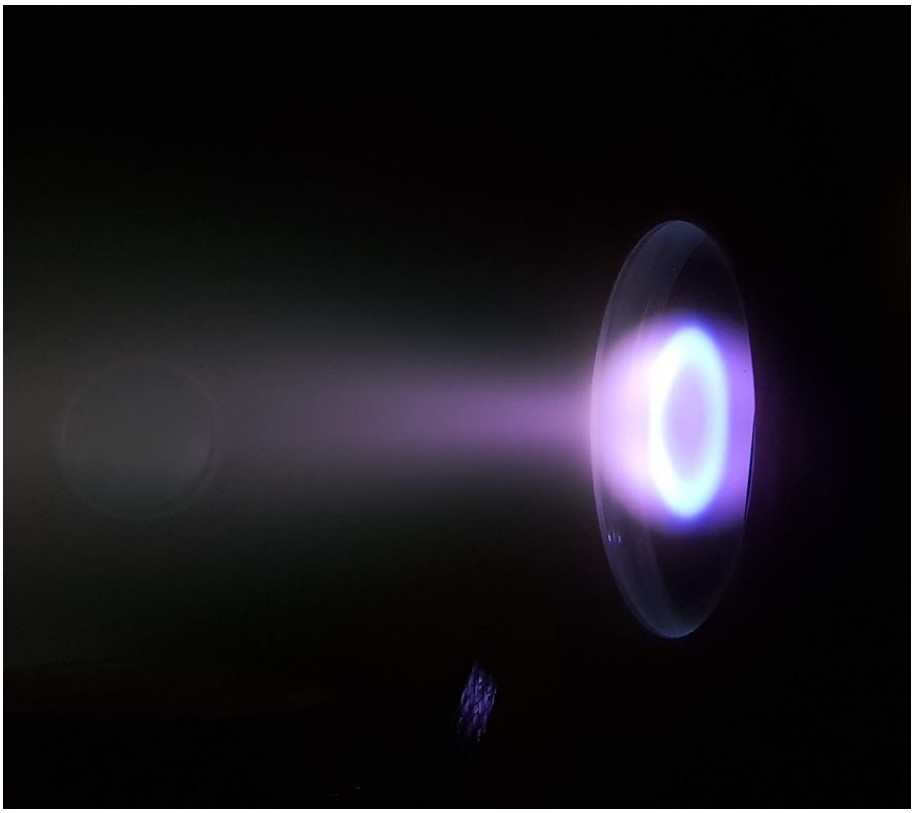

Figure 3.6: Silicon target magnetron discharge plasma. The bright annulus on the target surface is the magnetron racetrack. The plasma is seen extending out in front of the magnetron due to the type-2 unbalanced magnetic configuration.

3.2 ICP and Test Chamber

The magnetron system was mounted in an Plasmionique ICPII-600 chamber, see figure 3.7. The chamber was designed for ICP ion implantations, with the source of the ICP coming from a Seren R601 RF generator which drives the ICP coils located on top of the chamber. The coupling of the ICP power supply to the plasma is managed by a series-parallel 2 capacitor matching network (<1% reflected power). A Faraday shield positioned between the coils and the quartz window suppresses the E-mode and ensures the ICP operates in H-mode. This system is capable of producing an ICP plasma at maximum power of 600 W, for this project, an ICP power of 200 W was used. The RF frequency driving the ICP discharge is 13.56 MHz, this frequency was allocated to research, industrial and medical applications by legislation [1].

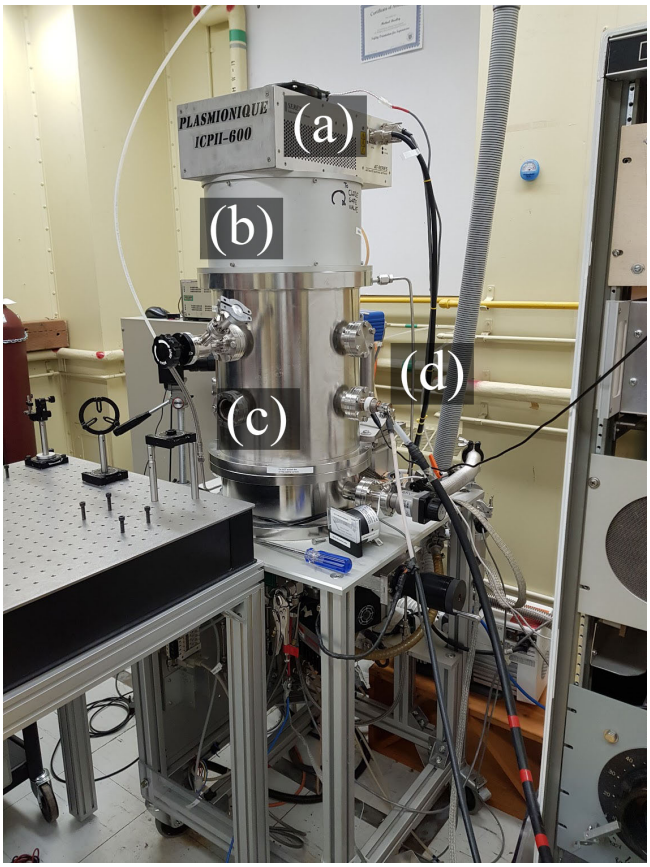

Figure 3.7: ICP immersed ion implanter chamber used for magnetron experiments. (a) Impedance matching network, (b) ICP coils, (c) vacuum chamber, (d) magnetron mounting port.

The chamber is cylindrical and has the dimensions: $1'$ (30.48 cm) in diameter and $1.5'$ (45.72 cm) high—giving it a volume of 33.41 L. The magnetron was mounted horizontally on one of the four lower ports on the side of the chamber. The chamber is pumped by a Turbovac TW 290 H turbo pump and an auxiliary roughing pump. The turbo pump has a pumping speed of 240 L/s for argon between 8×10^{-6}–8×10^{-3} torr (1.067×10^{-3}–1.067 Pa), giving us a base pressure of $\sim 10^{-7}$ torr ($\sim 1.333 \times 10^{-4}$ Pa). Experiments were conducted using argon as a background gas at around 5×10^{-3} torr (0.666 Pa), this was achieved using an MKS M100B mass flow controller, which fed a constant flow of $5\,\mathrm{cm}^3/\,\mathrm{min}$ of argon gas into the chamber.

3.3 Time-Resolved Langmuir Probe Measurements

A tungsten tipped Langmuir probe was mounted 8 cm in front of the centre of the target. A DC bias was applied to the Langmuir probe using a lab bench power supply, this current was directed through a shunt resistor whose voltage drop was measured using an INA 117 comparator op amp. The waveform of the probe current draw during the magnetron pulse was recorded using an Siglent SDS 1104X-E oscilloscope. The DC bias was generated from a GW Instek GPR-30H10D linear power supply and the voltage changed manually to obtain data for voltages from -40 to $+40$ V in steps of 0.5 V. The current waveforms at different applied voltages were combined in MATLAB to form continuous I-V curves that correspond to different times of the discharge. Langmuir analysis was be performed on these I-V curves to find the evolution of plasma characteristics over the duration of the discharge, this is discussed further in 4.1. A block diagram of the experimental setup is shown in figure 3.8.

3.4 Floating Probes

Three probes were used to measure the floating potential of the plasma during the discharge. The tips were made with tungsten wire, seated in a ceramic tube. The probes were positioned radially around the discharge region at ∼0, 180 and 257°. The floating potentials of the probes were measured using an oscilloscope. The probes were held in place by a stainless steel shroud fitted over the ground shield, see figure 3.9. The floating probes were connected using heat resistant thermocouple wire. A block diagram of the probes array and high-speed camera measurement system is shown in figure 3.8

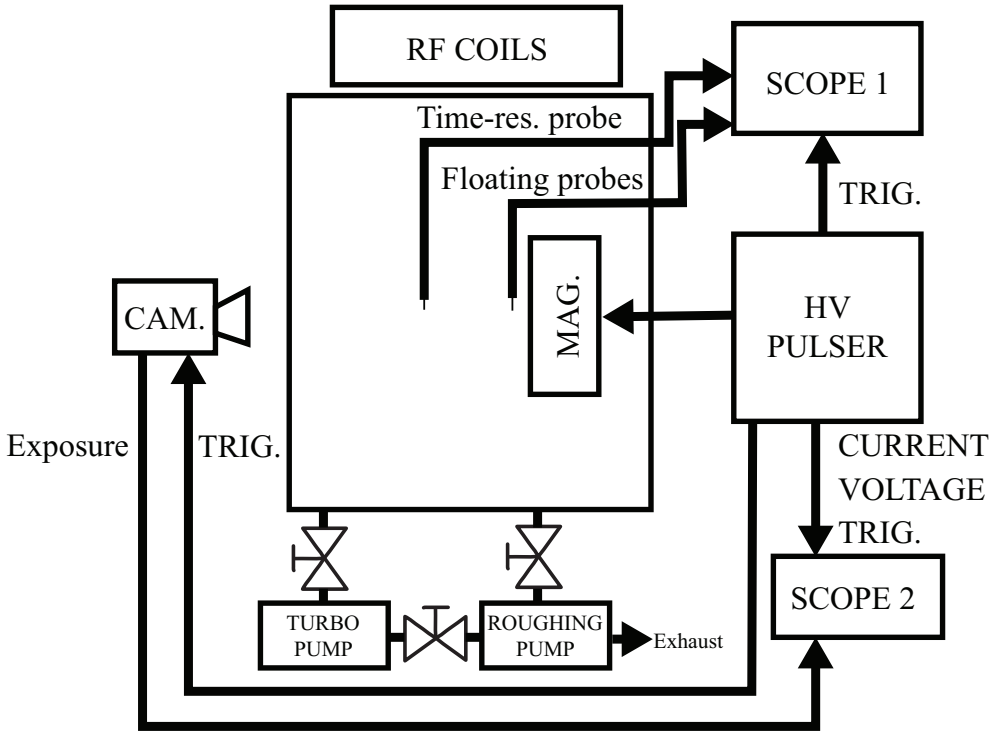

Figure 3.8: Floating probe and high-speed camera experimental setup block diagram.

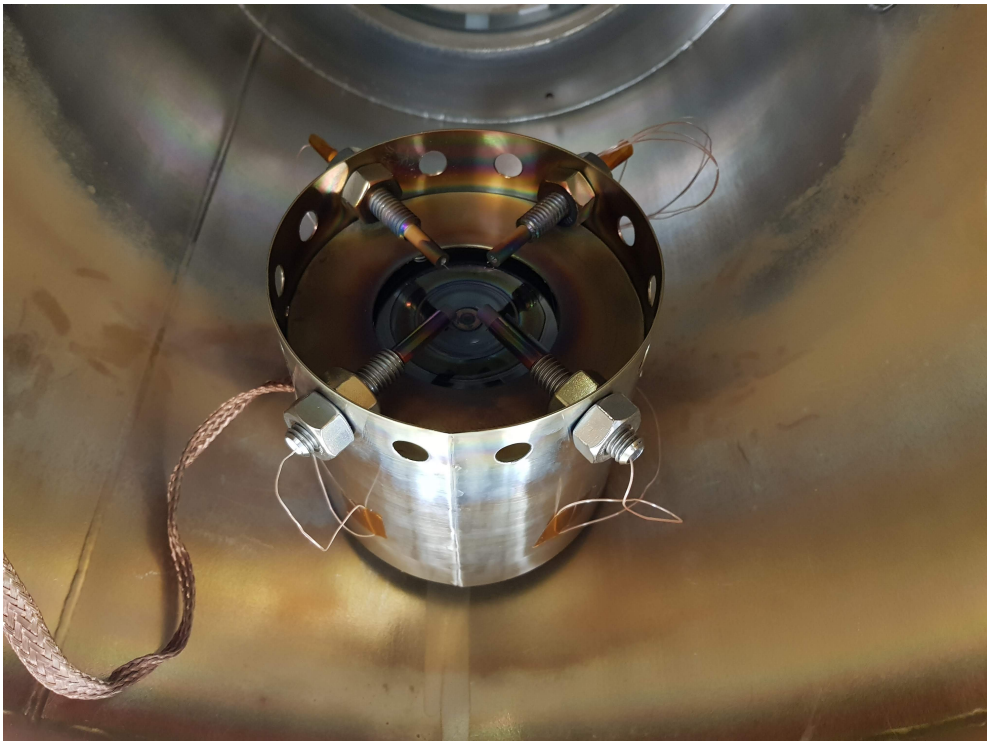

Figure 3.9: Assembled magnetron with radial probes mounted in ICP chamber. Four probes are shown in the picture, however, due to the limitations of our oscilloscope, only three were used.

3.5 High-speed camera

High-speed video of the magnetron discharge was captured using a Chronos 1.4 camera, the monochrome CMOS sensor on the camera was capable of 1.4 Gigapixel/s throughput, resulting in a maximum of 38500 frames per second; however, the resolution is greatly reduced at high frame rates. To capture images of the spokes the camera was set to 15941 frames per second, at a resolution of 336×240 pixels and an exposure time of 1 µs. Since the duration of the pulse discharge is 100 µs it can capture a max of two frames per pulse. The camera was set to record continuously, saving the frames into a ring buffer. This buffer stores frames until it is full. Once full, the newest frames overwrite the oldest frames in the buffer, allowing the camera to record indefinitely, but only saving recent frames. A 0–5 V TTL signal from the pulser was used to trigger the camera to stop the recording and save the frames in the buffer, the same TTL signal was also used to trigger two oscilloscopes in single trigger mode.

This allows measurements from the oscilloscopes and camera to be synchronized. Since the 62.73 µs period of the camera did not lineup exactly with the 100 µs pulse, the camera footage has a maximum ±1 camera period difference between the frames and the trigger pulse. To determine the exact time of the camera exposure, the camera exposure signal was measured using an oscilloscope. An example of the trigger timing is shown in figure 3.10.

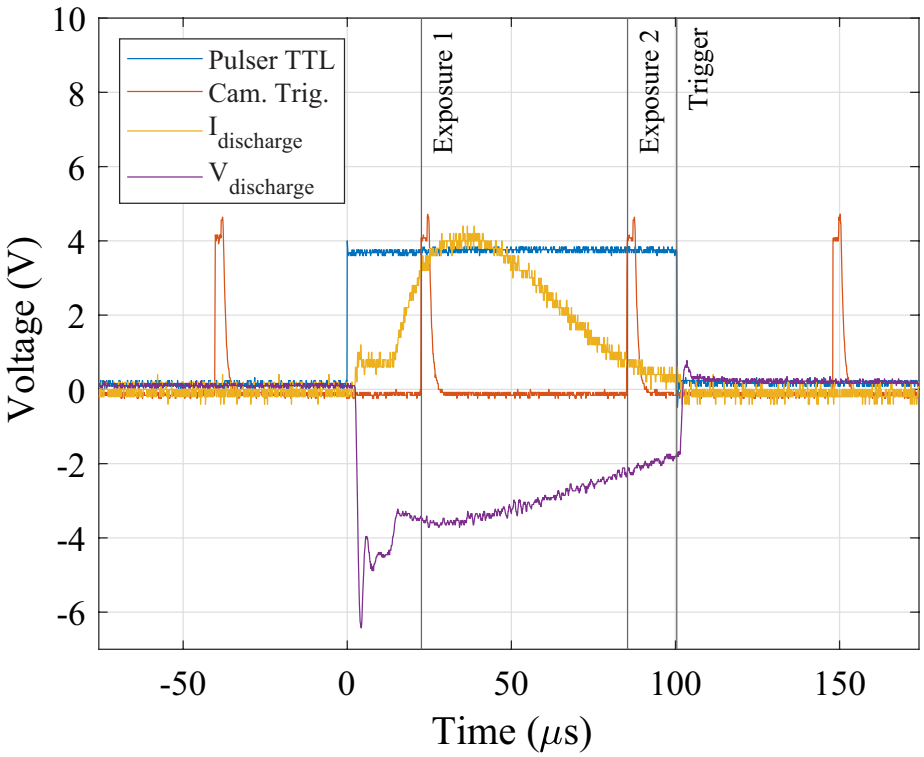

Figure 3.10: Example of the timing of camera trigger. The camera triggers on the falling edge of the pulser TTL signal, exposures before the trigger are saved and after the trigger are discarded. In this case two frames land within the pulse duration. Y-axis is not to scale for signals.

For high-speed camera measurements without floating probes, a CD4047 multivibrator in monostable mode was used to provide the camera trigger signal, this circuit is shown in figure 3.11. The pulser trigger signal is fed into the +TRIG. pin of the chip which triggers on rising slopes. Once triggered, the CD4047 provides a delayed trigger signal to the camera, the delay is controlled using a potentiometer. This allows us to capture frames at a certain time in the pulse and over multiple pulses, then, by varying the delay time, the evolution of the discharge was captured.

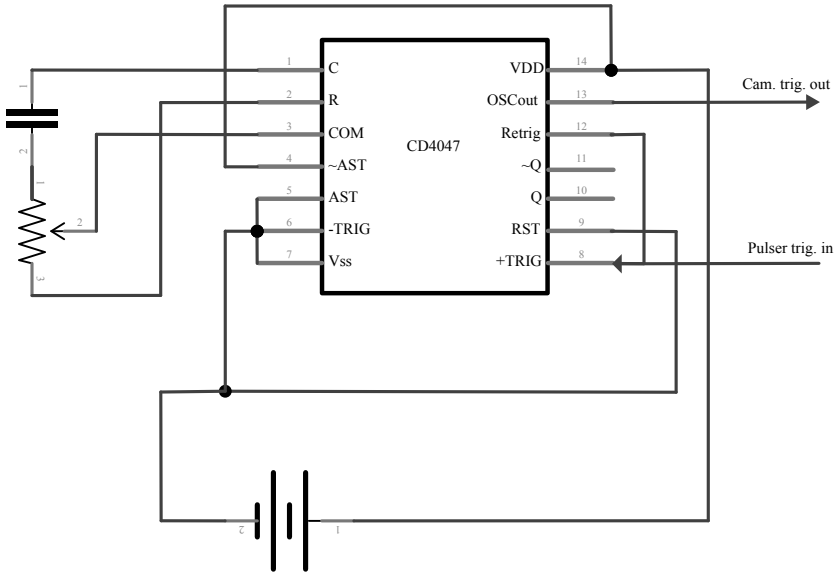

Figure 3.11: Circuit diagram of camera trigger circuit.

3.6 Optical Emission Spectroscopy

Optical emission spectroscopy (OES) was used to study the electron temperature and ion species in the plasma. OES was done using an Ocean Optics USB-650 Red Tide Spectrometer, which has a wavelength range of 350–1000 nm and a resolution of 1 nm. Since it only has a resolution of 1 nm, spectral broadening of the peaks cannot be analysed, but the intensities of the peaks can still analysed. The spectrum reported by the spectrometer was verified by measuring the spectrum of a sodium lamp, which produces two bright lines at 588.9950 nm and 589.5924 nm [15]. The intensity response of the spectrometer at different wavelengths was calibrated using a Newport 6334 NS quartz tungsten halogen lamp with a known spectrum; the curves used for calibration are shown in the Appendix in figure A.2. The vacuum chamber window and optical focus system was included in the calibration test to take into account their effects on the spectrum.

The integration time of the spectrometer is on the scale of seconds, so the result is a time-averaged spectrum of the magnetron discharge. The temperature was determined using the peak ratio and Boltzmann plot methods. The observed spectrum was compared to the NIST database to identify species in the plasma. Two lenses in a lens tube system was used to focus the light coming from the centre of the magnetron, figure 3.12. The lens tube was

affixed to the vacuum chamber port using a custom 3D printed sheath.

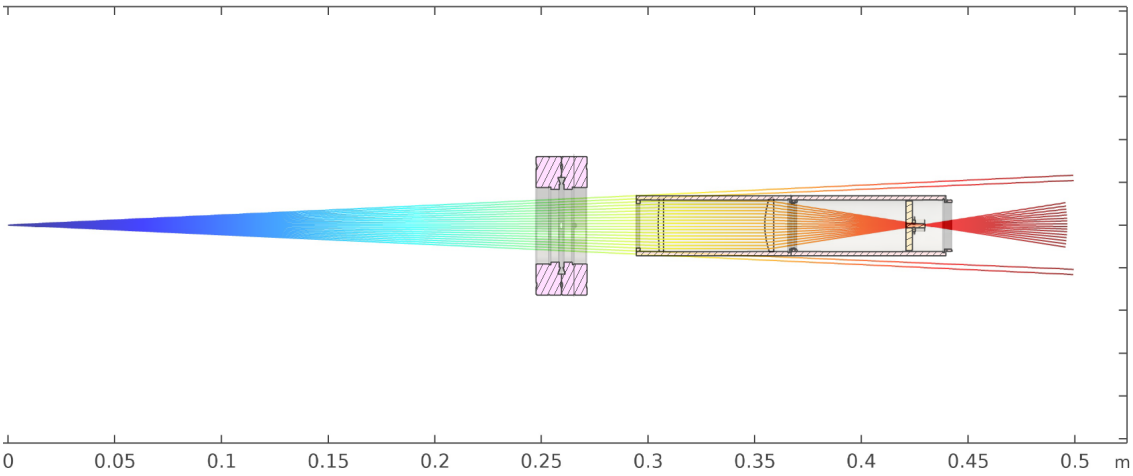

Figure 3.12: Raytrace diagram of focusing system. The light source is the magnetron target positioned at the opposite end of the chamber, approximately 30 cm away from the first lens. The metal piece in the centre represents the window of the vacuum chamber, on which the lens system was mounted.

4 Analysis

4.1 Time resolved Langmuir probe

The current drawn by the Langmuir probe at a fixed voltage during a discharge was recorded by an oscilloscope, this gives us high time-resolution in our data. To obtain the full I-V curve of the discharge, the voltage applied to the Langmuir probe was changed incrementally with each measurement, see figure 4.1 for visual example. This means that measurements at each voltage are taken from different pulses and we assume the I-V curve of the discharge stays constant as between pulses. We justify this by observing the continuity of the I-V curves between pulses.

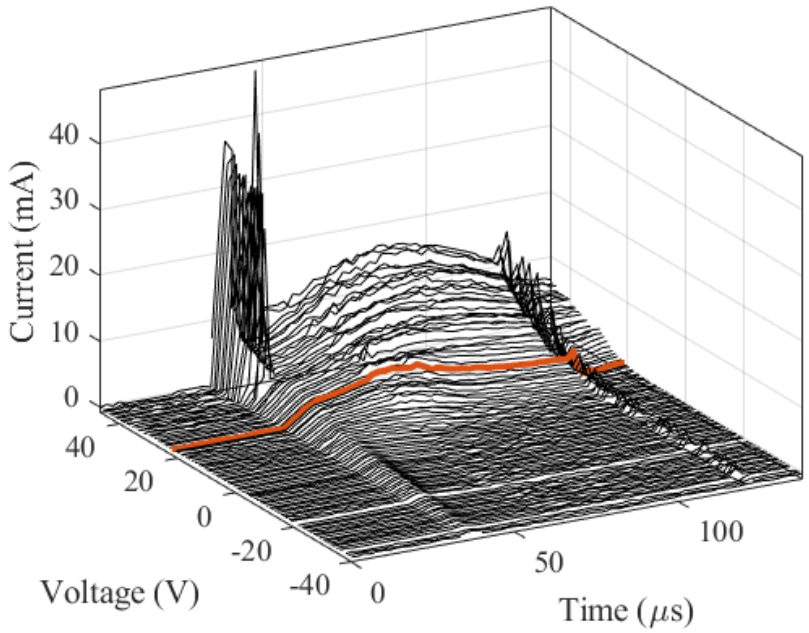

Figure 4.1: 3d plot of time resolved Langmuir probe data for 800 V magnetron discharge with a silicon target. The highlighted red line is an example of the data from one pulse at a fixed voltage.

To extract the information on plasma characteristics from the data, we first take the natural log of current for each I-V curve, then fit a arctangent line to the data points, see figure 4.2a. Since the natural log function only has real solutions for numbers greater than zero, the ion saturation region or negative current region is discarded. Finding the minimum of the second derivative of the fitted arctangent line reveals the location of the plasma potential. From here, the curve is divided into two regions, the electron saturation and transition regions, a linear line is fitted to both parts, see figure 4.2b. Then, following the process discussed in section 2.4.1 for Langmuir analysis, the values for electron density, electron temperature, ion density and plasma potential are obtained.

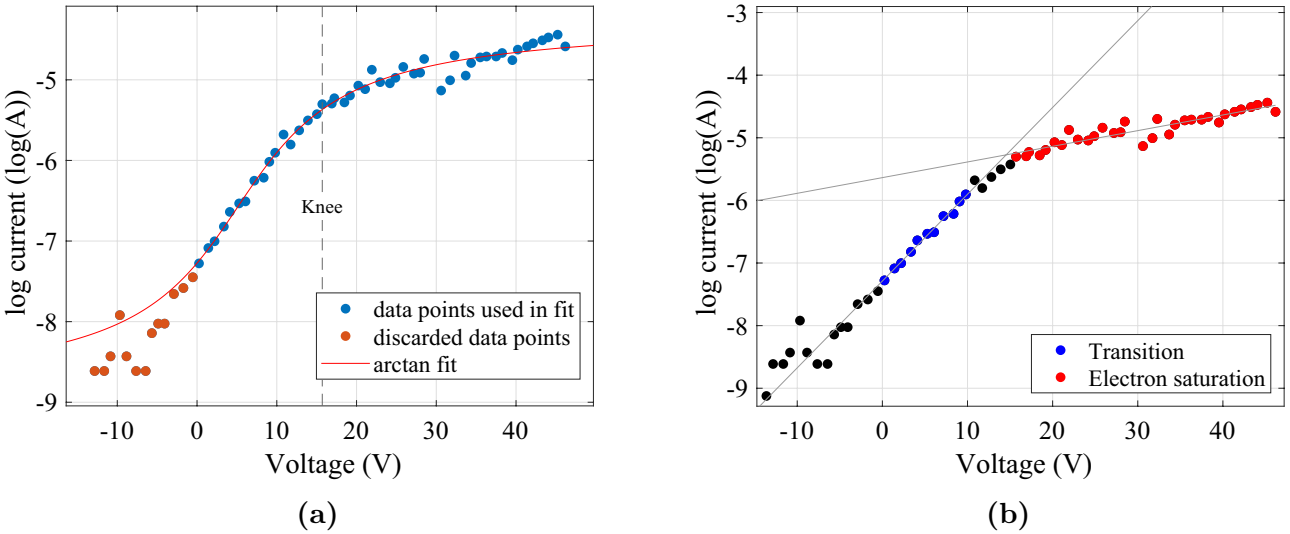

Figure 4.2: Fitting procedure to obtain electron transition and electron saturation data from I-V curves. (a) Fitting of arctangent curve to determine location of knee, (b) fitting of transition and electron saturation regions.

This process is done for I-V curved at each time step to produce a time-resolved picture of the discharge, see figure 4.1. Note not every I-V curve is viable for analysis, the data points before the pulse have no plasma so they are discarded. But also during pulse on and off, when the plasma is changing and has not yet reached a stable state, the I-V curves there are not suitable for Langmuir analysis and therefore discarded, examples of poorly behaving I-V curves are shown in figure 4.4. Figure 4.4 (a), was taken at a time before the plasma is fully formed, here the probe draws very little current, there is no clear distinction between the saturation and transition regions. The I-V curve shown in (b) at the moment the pulse

switches off. We see the I-V curve reaches saturation quickly, resulting in few data points for the determination of the transition region. We claim this is caused by the changing magnetron bias depleting the electrons around the probe, causing the Langmuir analysis to produce inconsistent results from one time-step to the next. Figure 4.5 shows the locations of these I-V curve discontinuities with respect to the discharge voltage.

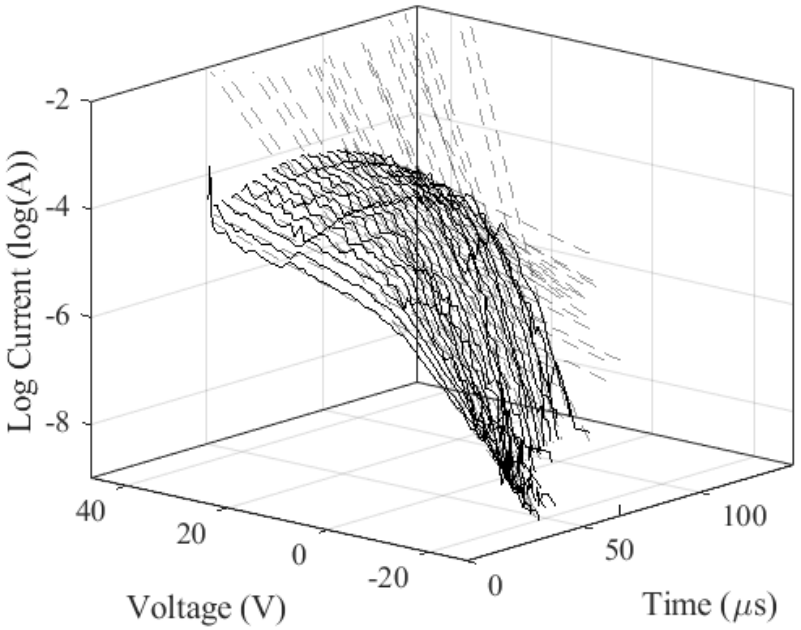

Figure 4.3: Time resolved I-V curves for Langmuir analysis. The dashed lines are the linear fits to the electron saturation and ion saturation regions. The number of curves were reduced for readability.

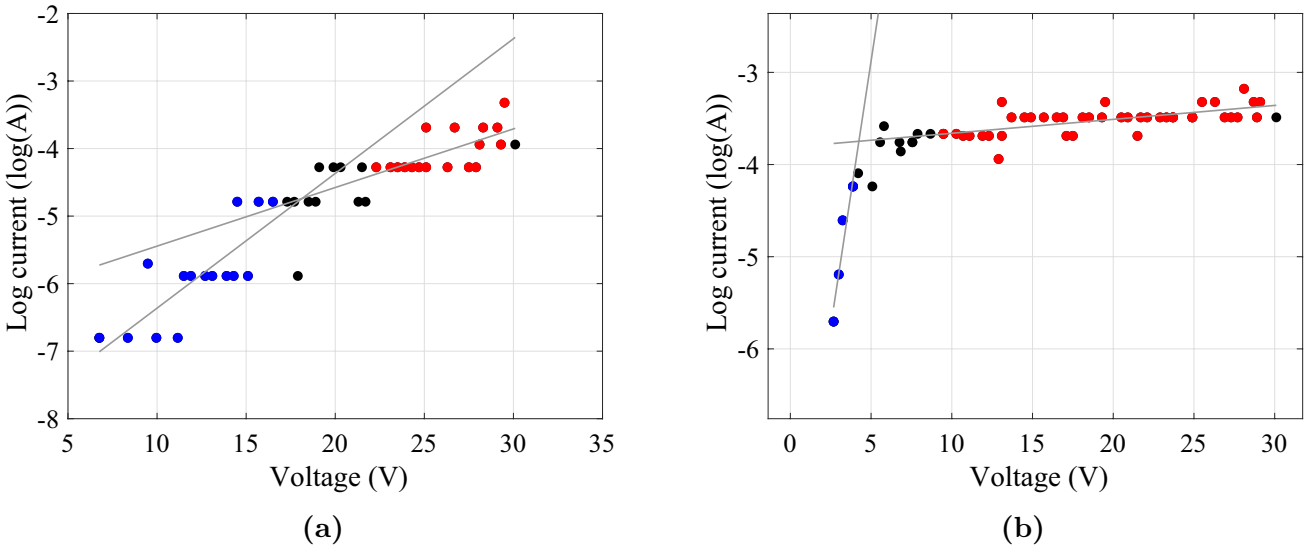

Figure 4.4: Examples of I-V curves not suitable for Langmuir analysis. (a) No clear distinction between transition and saturation regions, (b) Not enough data in transition region.

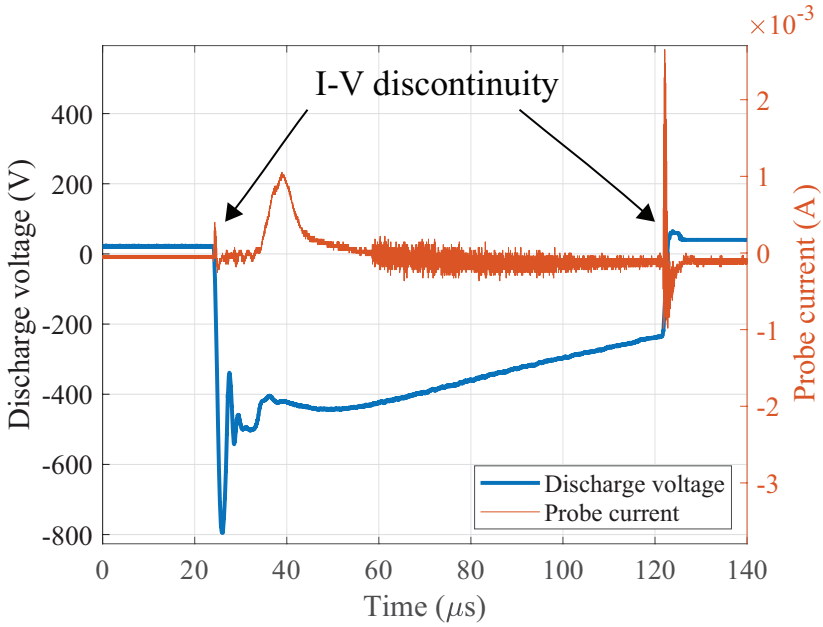

Figure 4.5: Location of I-V curve discontinuities at the start and end of magnetron discharge. The plotted probe current is the current measured by the Langmuir probe at a fixed voltage. The discharge shown is from a silicon target.

4.2 Probe array measurements and empirical mode decomposition

Signal from the three probes above the magnetron target were processed using empirical mode decomposition (EMD). EMD was chosen as it is a powerful method to decompose signals and allow us to extract signals of interest from our otherwise noisy raw data. An example processed signal from a floating probe is shown in figure 4.6.

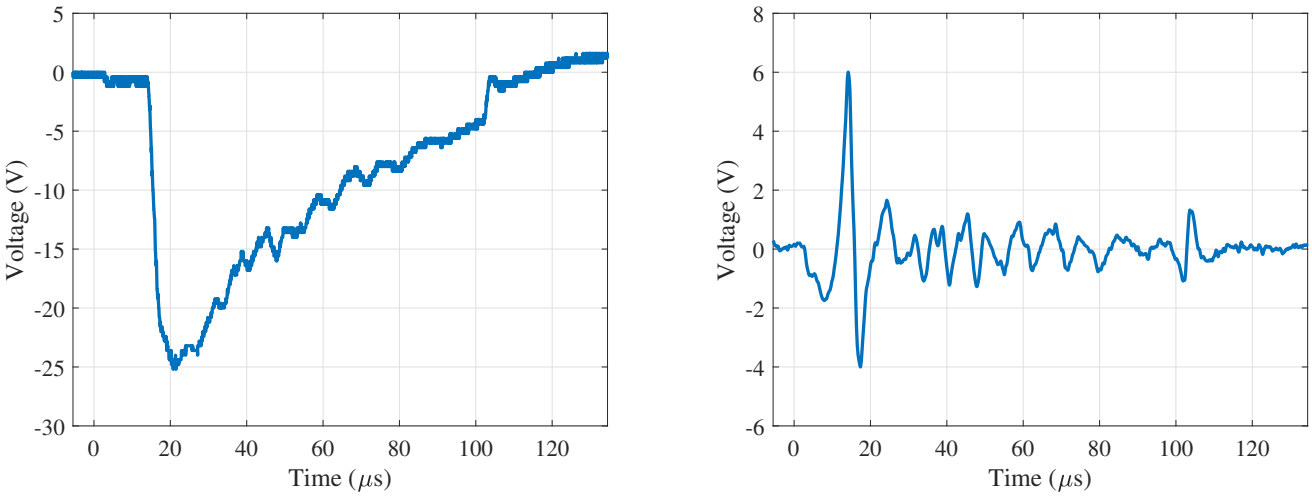

Figure 4.6: (a) Raw probe signal, (b) same signal processed signal using EMD.

EMD is an algorithm to decompose non-linear and non-stationary signals into various components of different frequencies known as intrinsic mode functions (IMFs) or modes [31]. EMD differs from Fourier transform and wavelet decomposition in that it is completely data driven and does not need any *a priori* defined basis system [32]. Here I give a high-level description of how the EMD algorithm decomposes a signal, using a sinusoidal signal as an example:

1. Find all local extrema in the signal.

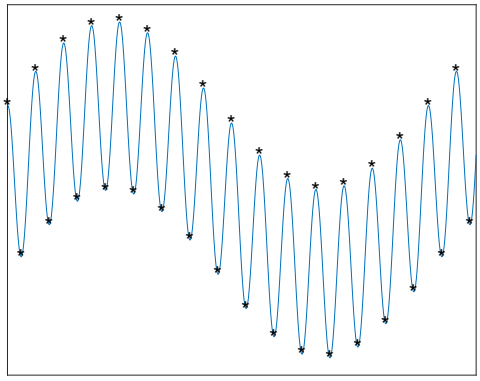

2. Interpolate between the extrema to form an envelope around the original signal.

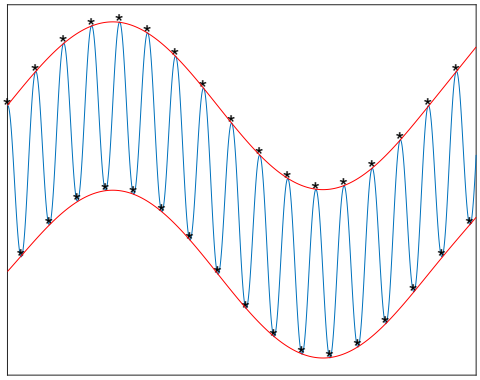

3. Compute the mean of the envelope $m_1 = (e_{\min} + e_{\max})/2$.

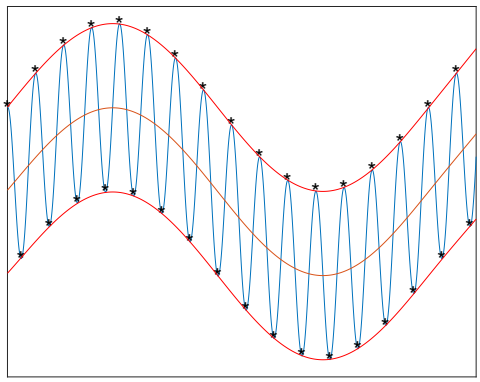

4. Subtract the calculated mean from the original signal $h_1 = X - m_1$, and verify that the h_1 satisfy the requirements of an IMF, that is:

   (a) The number of extrema and the number of zero-crossings must be equal or differ by one.

   (b) The mean value of the envelope must be zero.

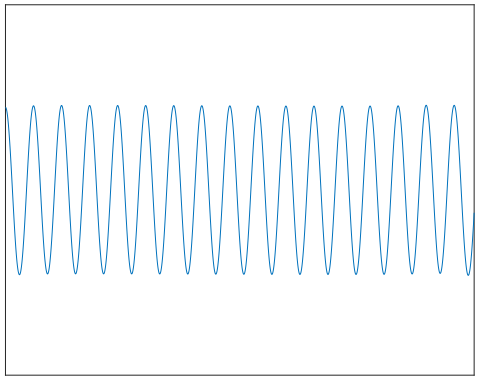

If h_1 does not satisfy the requirements, steps 1-4 are repeated using h_1 as the input until h_{1n} satisfies the requirements or the maximum number of iterations is reached. If h_{1n} satisfies the requirements, it is assigned as the first IMF or mode.

5. Repeat steps 1-4 for each m_n to find subsequent modes until the final mode which should be a monotonic curve with no extrema.

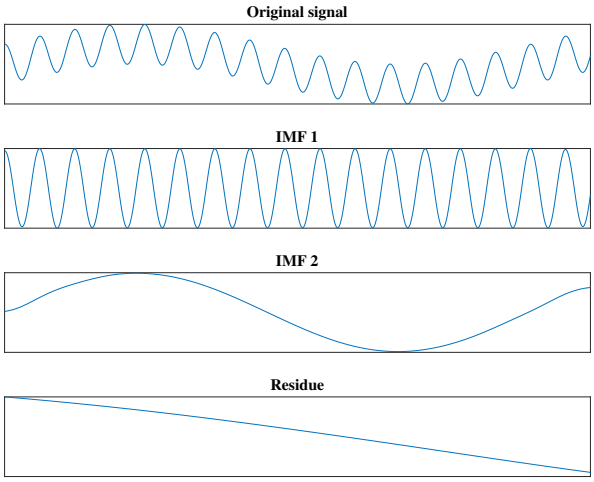

The original signal can be reconstructed without any loss of information as the summation of the modes. Ideally, the EMD algorithm separates the oscillations in the signal into distinct IMFs, however, this is not always the case. One of the problems EMD experiences is called mode mixing, where the oscillations in the signal do not contribute enough to the maxima/minima and the algorithm is unable to separate it into its own IMF, instead it remains mixed in another IMF [33].

To reduce mode mixing, a method was introduced, called ensemble empirical mode decomposition (EEMD) [34]. In EEMD, a series of Gaussian white noise is added to the original signal to separate out the modes. $x^i[n] = x[n] + w^i[n]$, where $w^i[n](i = 1, ..., I)$ are different realizations of Gaussian white noise and $x[n]$ is the original signal. Each realization $x^i[n]$ is decomposed via EMD to produce $\text{IMF}_k^i[n]$, where k indicates the mode number. The "true" $\overline{\text{IMF}}_k$ is obtained by averaging the k^{th} $\text{IMF}_k^i[n]$ over all realizations; with enough realizations, the added white noise is removed via the average process [34]. For this project, the probe signals are processed using the complete ensemble empirical mode decomposition (CEEMD) algorithm from [31]. Whereas EEMD computes each realization separately, CEEMD calculates each realization using the residue from the previous realizations. This alleviates some problems with EEMD where residual noise is present in the reconstructed signal [31]. An

example of mode mixing and the difference between EMD and CEEMD capabilities is shown in figure 4.7.

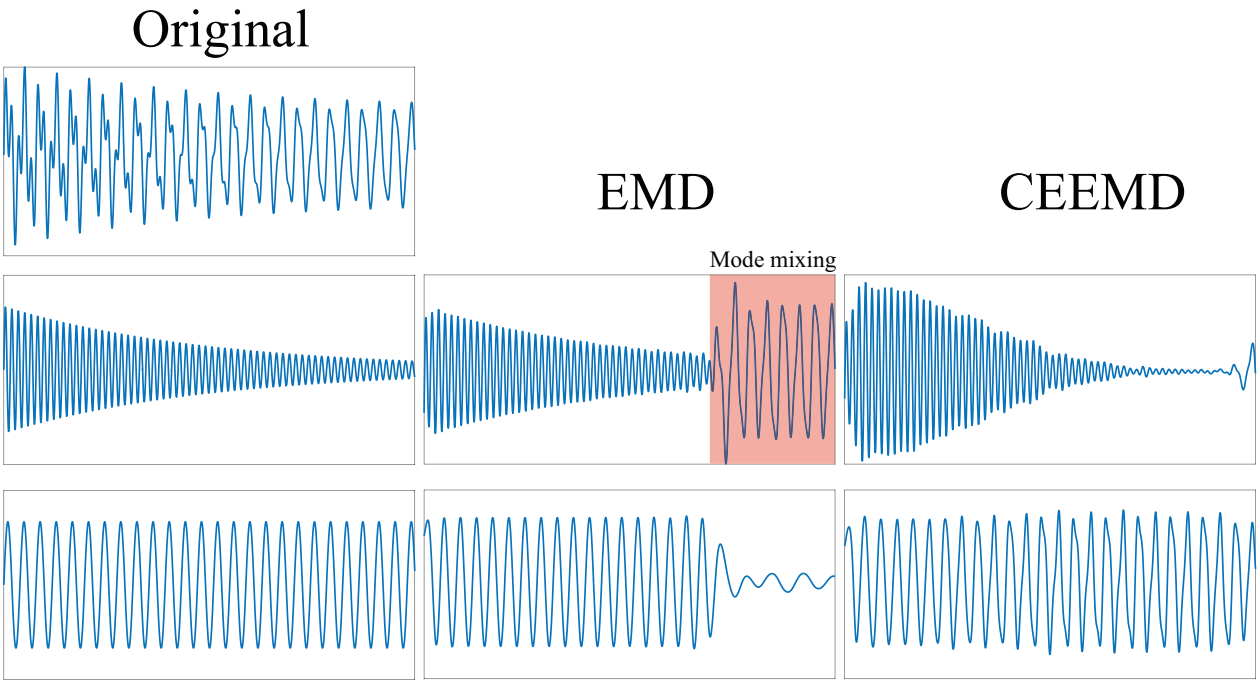

Figure 4.7: Mode mixing example. The original signal (top left) is the sum of two terms: $f(x) = \exp(-0.1x) * \sin 20x + sin(8x)$; these two terms are plotted separately under the original signal. In the centre and right columns are IMFs extracted from EMD and CEEMD respectively. As the exponential term gets smaller, the EMD algorithm cannot decompose the signal into different frequency IMFS, resulting in mode mixing. This problem is reduced by CEEMD, here we see the two terms were extracted with better accuracy.

4.3 Cross-correlation

After being decomposed into individual IMFs, the signal from the floating probes were cross-correlated to investigate the time offset between the probes. Cross-correlation measures the similarities between two signals for a given time shift [35]. This is accomplished by a sliding dot product given by the equation [35]

$$(f \star g)(\tau) \equiv \int_{-\infty}^{\infty} \overline{f(t)} g(t+\tau) dt, \tag{4.1}$$

where f and g are period signals, τ is the lag time and $\overline{f(t)}$ is the complex conjugate of f. An example of the cross-correlation done for the probe signals is shown in figure 4.8. The

location of the peak of cross-correlation indicates the lag time between the channels.

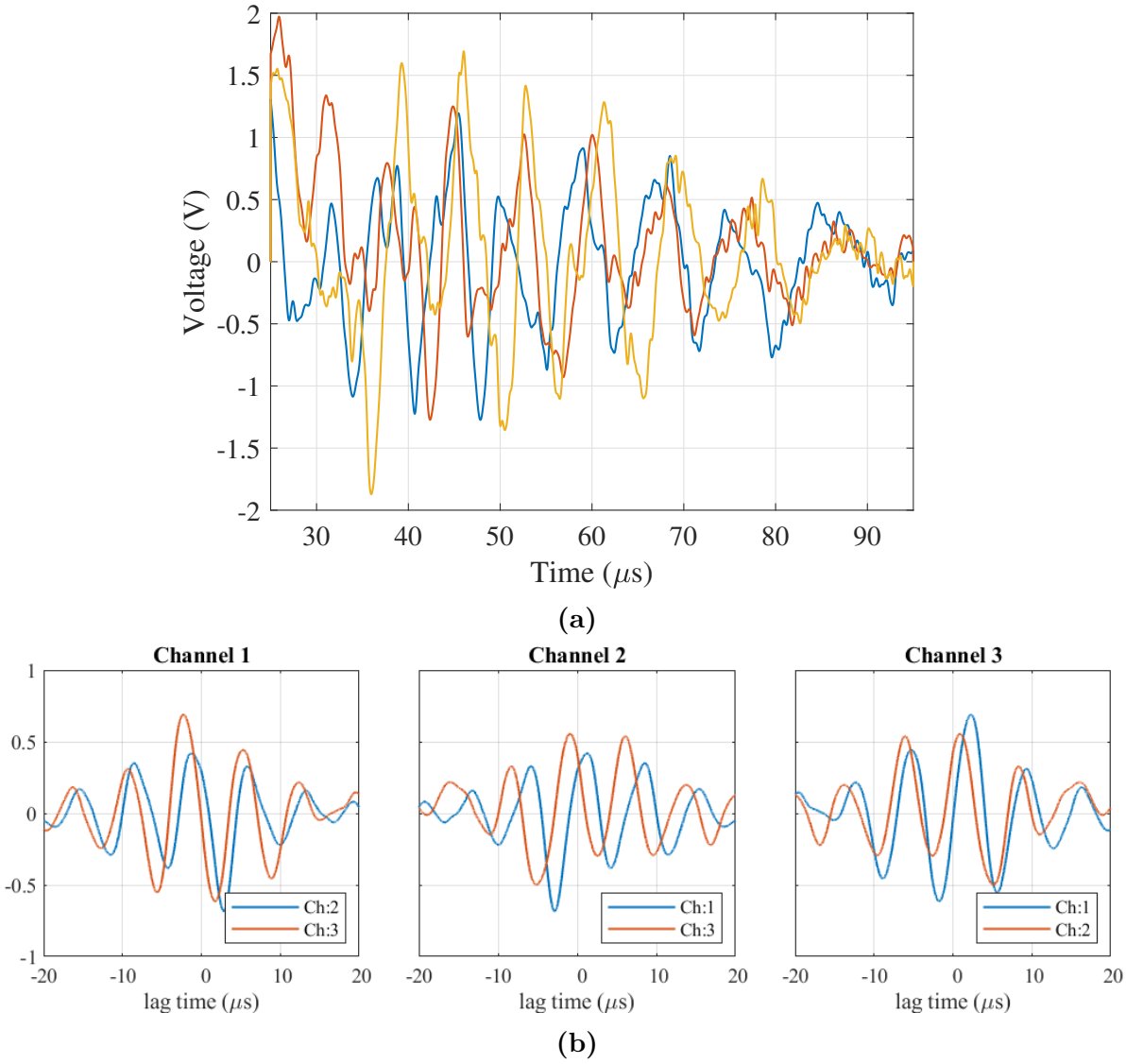

Figure 4.8: Cross-correlation example. (a) EMD processed probe signal, (b) normalized cross-correlation results.

4.4 High-Speed Camera

Around 32,000 frames of the discharge were captured using the high-speed camera each frame containing information about the plasma. Our goal with the footage is to determine the sizes of the spokes, the mode number and the intensity of the spokes which has been correlated

with ion production [12]. To automate the image processing, a custom MATLAB script was used, the images were processed as follows:

1. The image is read in and the intensity adjusted such that the top 1% and the bottom 1% of pixel values are saturated, figure 4.9 (a) and (b).

2. The image is eroded to remove small noise pixels surrounding the discharge, then the image is reconstructed to restore the original size and shape of the surviving pixels. This is called opening by reconstruction, figure 4.9 (c).

3. Convert image into binary image by setting all pixel values below 85% of the maximum to 0 and those above to 1, figure 4.9 (d).

4. The binary image has many holes and rough edges, these are smoothed out using a closing followed by an erosion. Finally an area open operation removes any areas smaller than a certain threshold to ensure the final preserved structures are the main plasma maxima, figure 4.9 (e).

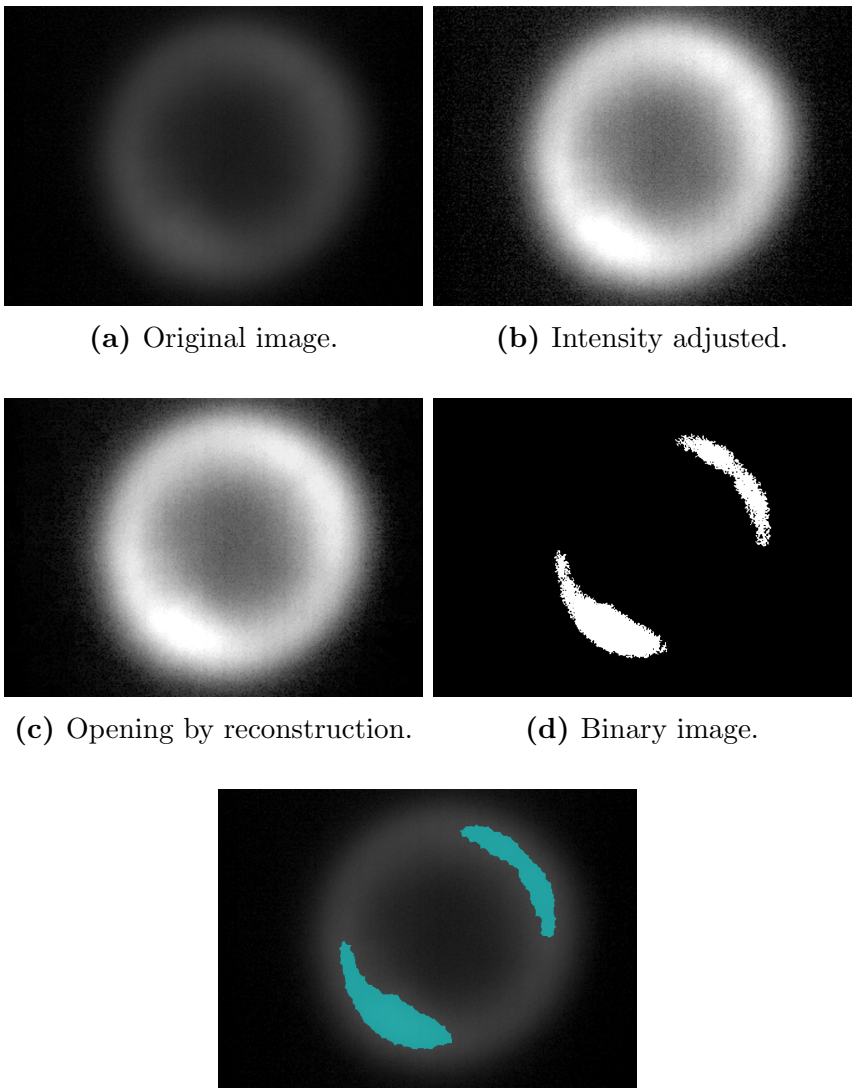

(a) Original image.

(b) Intensity adjusted.

(c) Opening by reconstruction.

(d) Binary image.

(e) Final image overlaid on original.

Figure 4.9: Image processing steps to identify spokes in image.

5 Results

5.1 Magnetron Discharge Characteristics

Figure 5.1 shows the voltage and current draw of the magnetron with varying pulse lengths using a silicon target and 5 mtorr of argon and a peak voltage of −800 V. Higher voltages were not explored due to excessive arcing and limitations of the power supply.

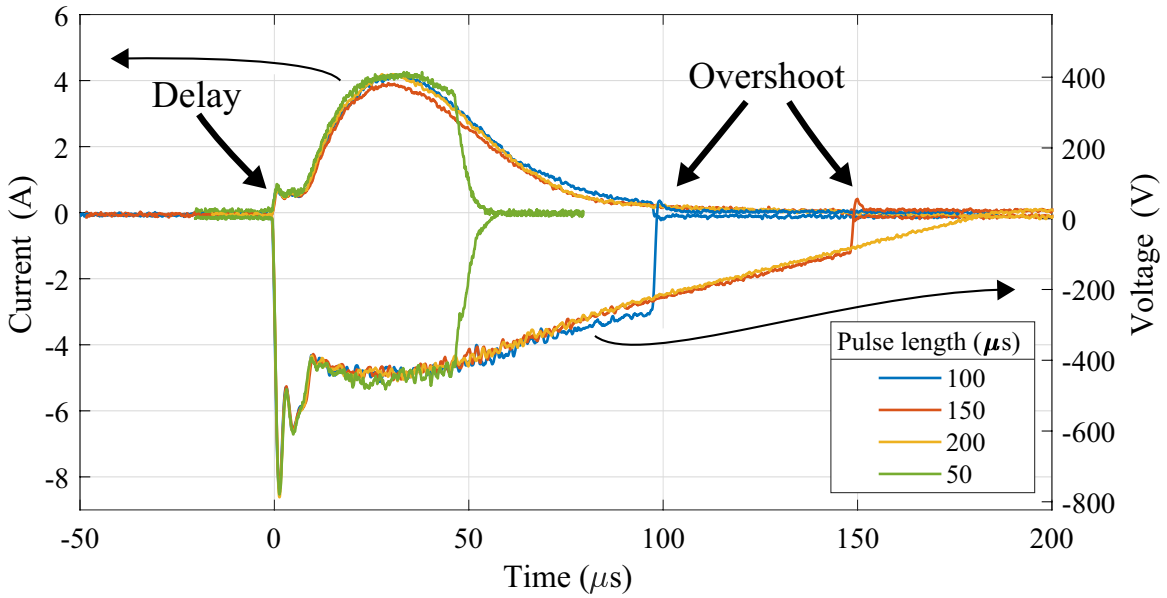

Figure 5.1: Silicon target magnetron discharge current (positive) and voltage (negative), with varying pulse lengths. The initial delay and final overshoot that distinguish the magnetron and the ICP assisted magnetron discharges are labeled.

Due to the limitations of the capacitive discharge provided by our pulser, the upper limit to the pulse time is around 200 µs. For the rest of the study we chose to use a pulse length of 100 µs, since it has been shown that plasmas in shorter pulses do not have enough time to develop into a stable discharge [7]. Multiplying the current and voltage together and averaging over time, we find the average power during the 100 µs discharge is 392 W.

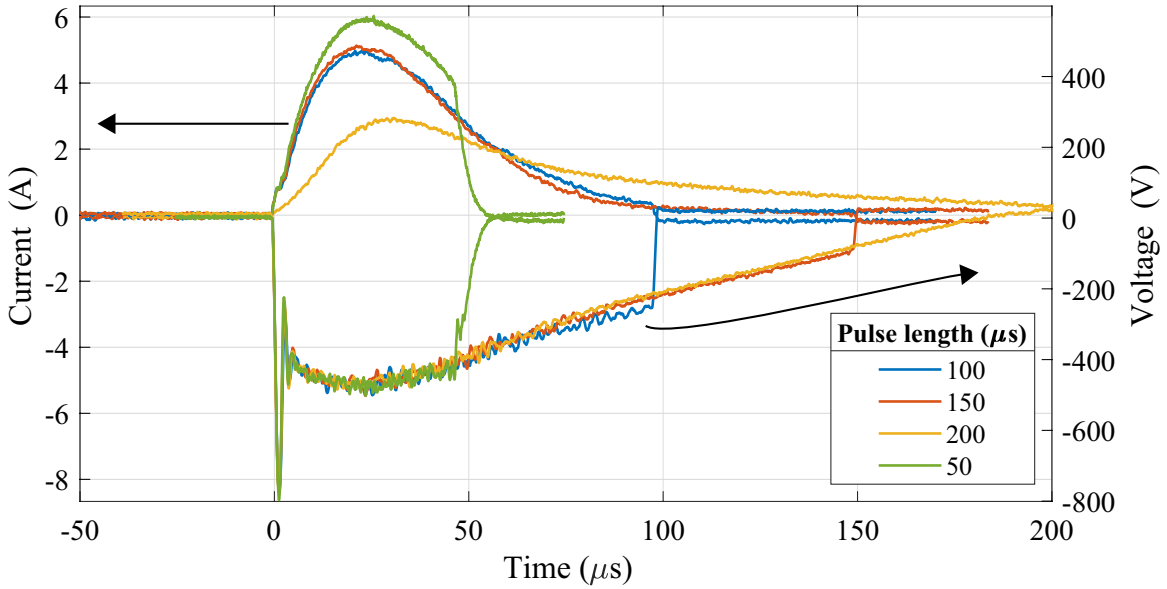

Figure 5.2: Silicon target ICP assisted magnetron discharge current (positive) and voltage (negative) with varying pulse lengths. Here, a much shorter delay is observed and no overshoot compared with figure 5.1.

In figure 5.2, the variation of pulse length is carried out together with a 200 W ICP discharge. The combined discharge draws more current than the magnetron only discharge. With the ICP, the average power of the 100 µs discharge increases to 464 W. The current waveforms shows that for combined discharges, the current rises quickly, in time with the voltage, while for the magnetron only discharge, the current has a delay of ∼7 µs before rising to its peak. This delay has been observed before by others [7]. It was determined that the delay time increased with the decrease of pressure, until the plasma is no longer able to ignite [7]. The shorter delay time observed in the ICP assisted discharge affirms that the secondary discharge provides a seed of ionized gas so the main discharge can form quicker and at lower pressures [7]. Without the ICP, the voltage overshoots and swings positive at the end of the pulse, in the combined discharge, the extra electrons from the ICP reduces this positive voltage swing, this is seen in figures 5.1 and 5.2.

Figure 5.3 shows the current waveforms of varying discharge voltages with different ICP powers, here we see the inital lag time decreases as the applied voltage or ICP power is increased. Furthermore, as the discharge voltage and ICP power is increased, we see the current waveform peak become more symmetrical and the tail flattening out faster. This

change in the current waveform is likely due to gas rarefaction. At higher powers, the increased sputtering causes the argon gas to deplete faster, resulting in a drop in secondary electron production and the current. The effects of gas rarefaction is more pronounced in the waveform of the aluminum target, shown in comparison with the silicon target waveform in figure 5.4. Here, the same pulse is applied to the two targets, but results in very different waveforms. It is evident that the aluminum target draws more current, therefore experiencing more gas rarefaction. For the silicon target, we see a lower current draw, and the discharge current tapers off slower than for aluminum. The difference in the current draw of the two materials could be a result of the difference in secondary electron yield. The secondary electron emission coefficients are $\delta_{\text{Aluminum}} = 0.84$ and $\delta_{\text{Silicon}} = 0.44$ at $2\,\text{keV}$ [36]. The lack of secondary electrons would mean less charge carriers to facilitate current flow from the target and result in a lower discharge power.

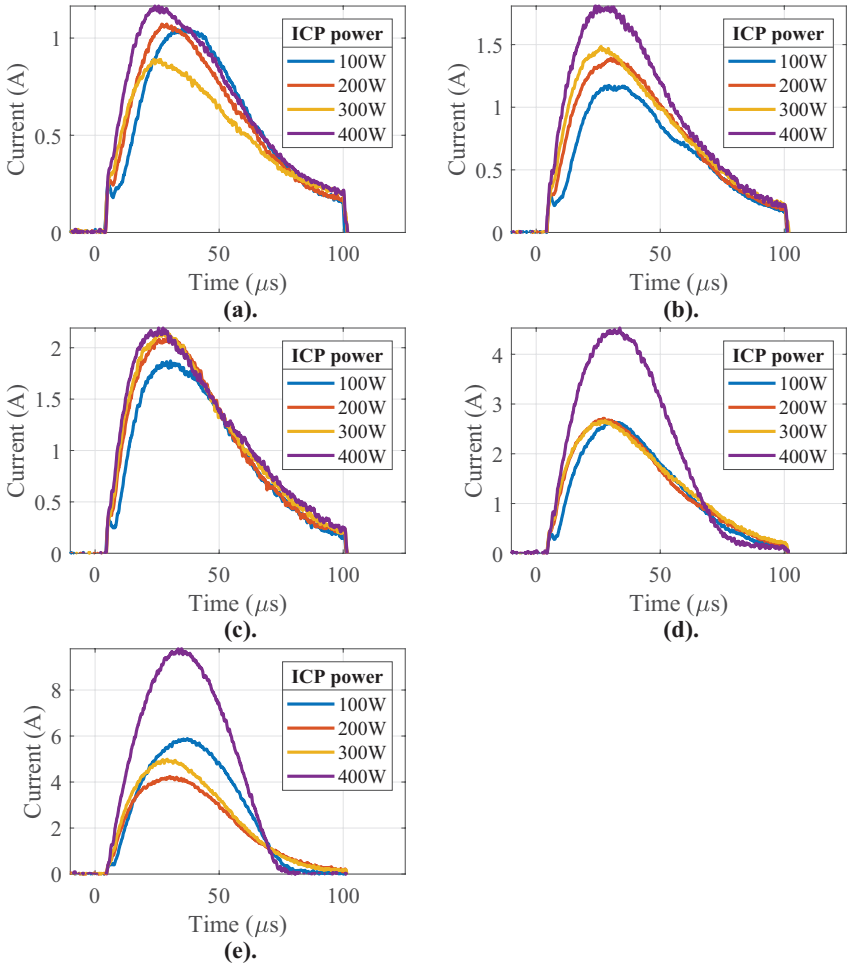

Figure 5.3: 100 µs pulse, silicon target discharge current with varying applied voltage and ICP power. Discharge voltage: (a) −500 V, (b) −600 V, (c) −700 V, (d) −800 V, (e) −1000 V. The delay at the start of the pulse is less pronounced at higher ICP powers. In general we see higher discharge current for higher ICP powers.

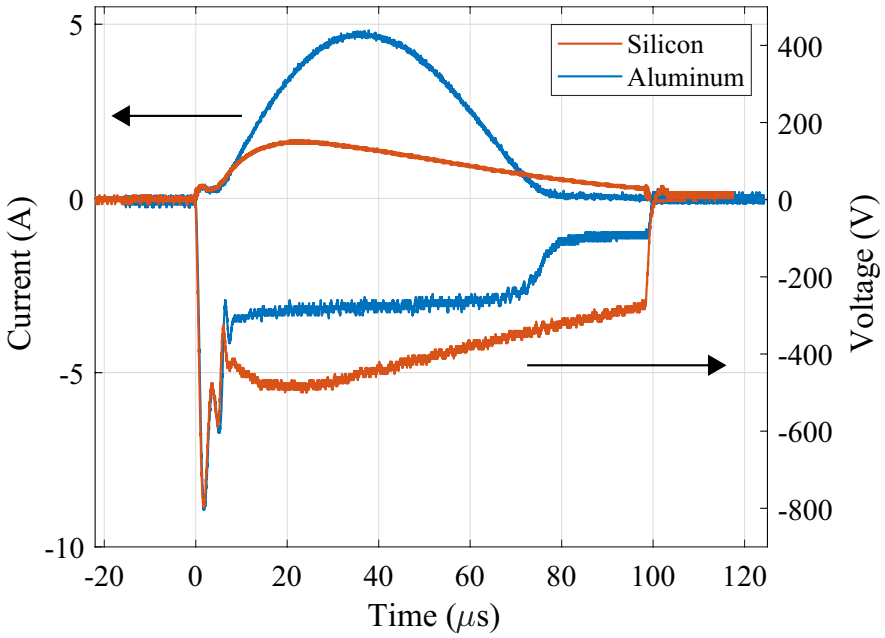

Figure 5.4: Magnetron discharge waveform with silicon and aluminum target under the same conditions: 100 µs, 5 mtorr and −800 V. Negative going curves are voltage while the positive going curves are current. A clear difference between the magnitude and shape of the discharge current and magnitude can be seen between the two target materials.

In the presence of an ICP discharge, we observe a significant increase in discharge power for the silicon target, and a smaller increase for aluminum target, see figure 5.5. Here, the power of the silicon target discharge is limited by the secondary electron production, the addition of the ICP increases the electron density and therefore the current flow. However, once the discharge power reaches a certain point, the effects of gas rarefaction become more pronounced, which results in the smaller power increase seen in the aluminum target. If the discharge power were increased further, we would start to see self-sputtering—where ionized target material takes over the sputtering process. In section 2.3.2, the discharge current characteristic of self-sputtering was discussed, the discharge current would have a initial peak corresponding to argon sputtering and a secondary peak corresponding to self-sputtering—whose prominence would be dependent on the self-sputtering parameter of the material. We did not observe any evidence of self-sputtering at the discharge powers attempted, since all the current waveforms we observed only show a single peak followed by a tapering tail.

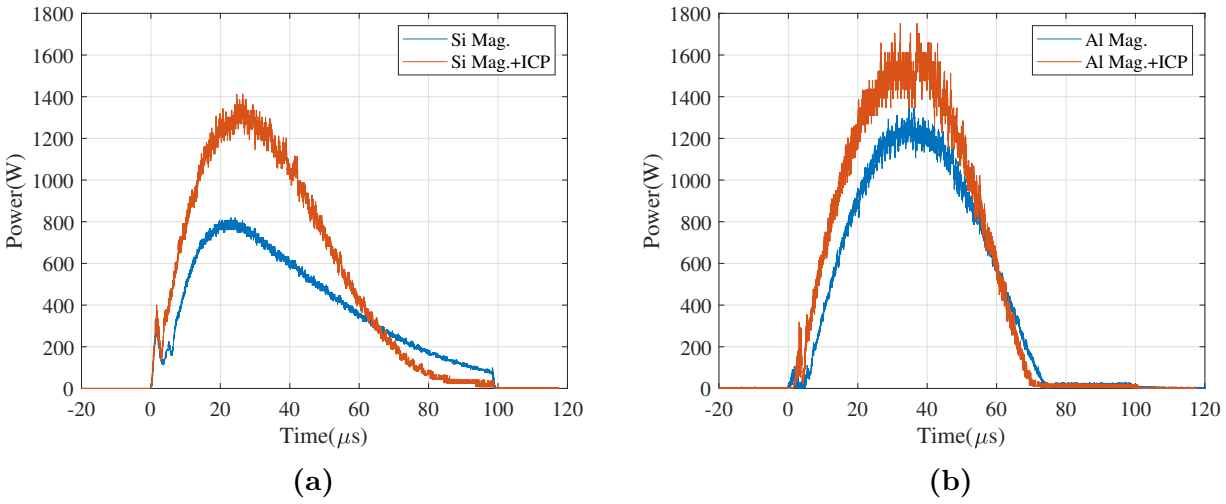

Figure 5.5: Effect of the addition of a secondary ICP discharge on magnetron discharge power of (a) silicon and (b) aluminum targets. The increase in power is much more pronounced for the silicon target. The increased power also causes the power to decrease faster after reaching the peak, we claim this is due to gas rarefaction.

5.2 Emission Spectroscopy

Figure 5.6 shows the spectrum of the magnetron plasma when using a silicon target.

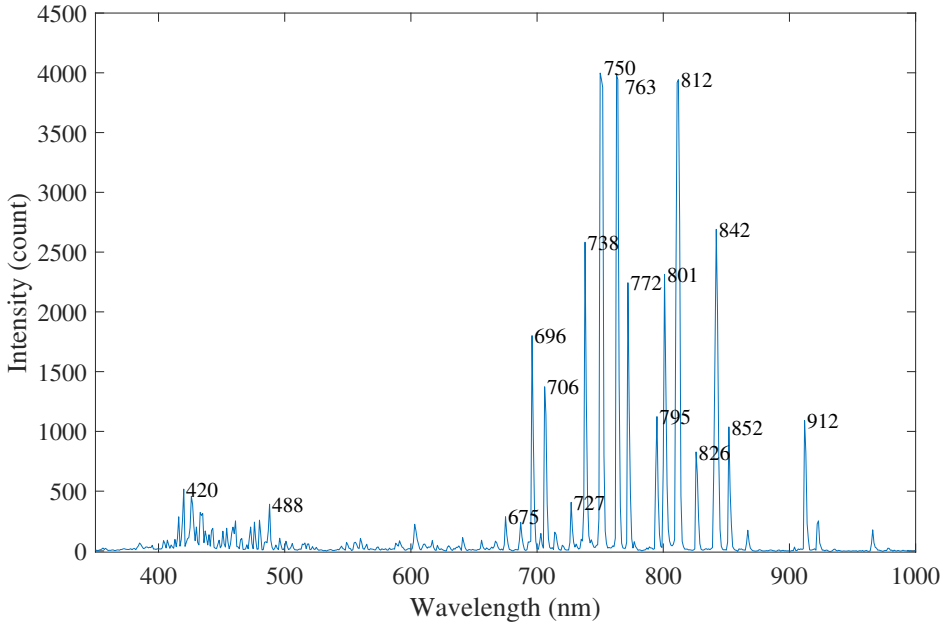

Figure 5.6: Silicon target emission spectrum. Prominent peaks are labeled with their respective wavelengths.

Comparing the spectrum observed from the discharge to known argon lines, the prominent peaks in figure 5.6 can all be attributed to argon neutrals, no silicon lines were observed [15]. The most intense silicon lines within our detection range are 742, 728, 740 and 390 nm, none of these lines were detected as significant peaks in our spectrum [15]. In the NIST database, the spectral lines are given with a relative intensity, the strongest silicon line is 281 nm with an intensity of 1000, whereas the strongest line in our detection range is 390 nm with an intensity of only 200, so the silicon lines maybe too faint for our spectrometer to detect. This was not the case for aluminum, figure 5.7 shows the spectrum of the magnetron discharge under similar conditions with an aluminum target. Here, the prominent peaks 396 and 394 nm are attributed to aluminum neutrals and 466 nm is from singly ionized aluminum [15].

Following the process discussed in section 2.4.2, we use the line intensity from our observations in figures 5.7 and 5.6 and the data on the transition probabilities from table 5.1, we construct Boltzmann plots of the spectrum for each discharge, an example is shown in

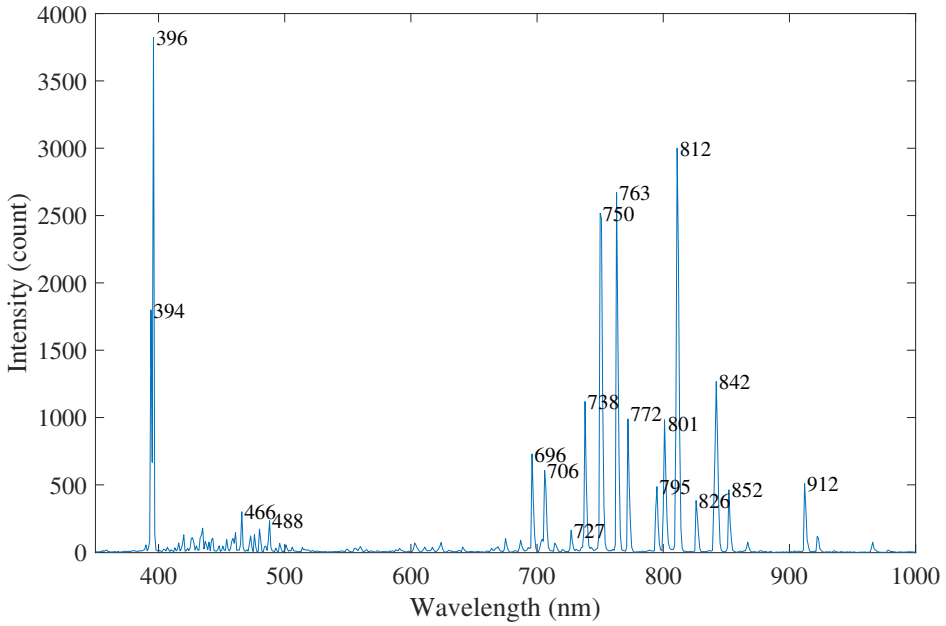

Figure 5.7: Aluminum target emission spectrum.

figure 5.8. The slope of the linear fit of the data points is used to find electron temperature, shown in figure 5.9. The collection time of the spectrometer is on the order of seconds, so this represents a time averaged measurement of the electron temperature. From figure 5.9, we see very little change in electron temperature with increasing discharge voltage; similar results were reported by Crintea *et al* in [37]. Electron temperatures for HiPIMS discharges generally start high, around 6 eV, then stabilizes around 1 eV [7]. So the temperature results we obtained for the magnetron discharge is acceptable considering it is a time-averaged measurement of the pulse. However, the temperatures we obtained for the ICP combined discharge is too low. An argon ICP plasma under the conditions we were operating at should have electron temperatures of around 3 eV [1]. The factors that impact the accuracy of our OES temperature measurements are:

- Assumption of LTE and optically thin plasma—this may not be the case for all the Ar-I lines used.
- Resolution of the spectrometer—with a minimum resolution of 1 nm, emissions from nearby lines resulting in higher apparent line intensity.

Table 5.1: Spectroscopic data for Ar I lines, obtained from NIST [15].

λ (nm)	E (eV)	gA (s^{-1})
912.30	12.91	5.7×10^7
866.79	13.15	7.3×10^6
810.37	13.15	7.5×10^7
739.30	13.17	2.2×10^6
731.60	15.02	2.9×10^6
614.54	15.32	5.3×10^6
542.14	15.36	3.0×10^6
522.13	15.45	7.9×10^6

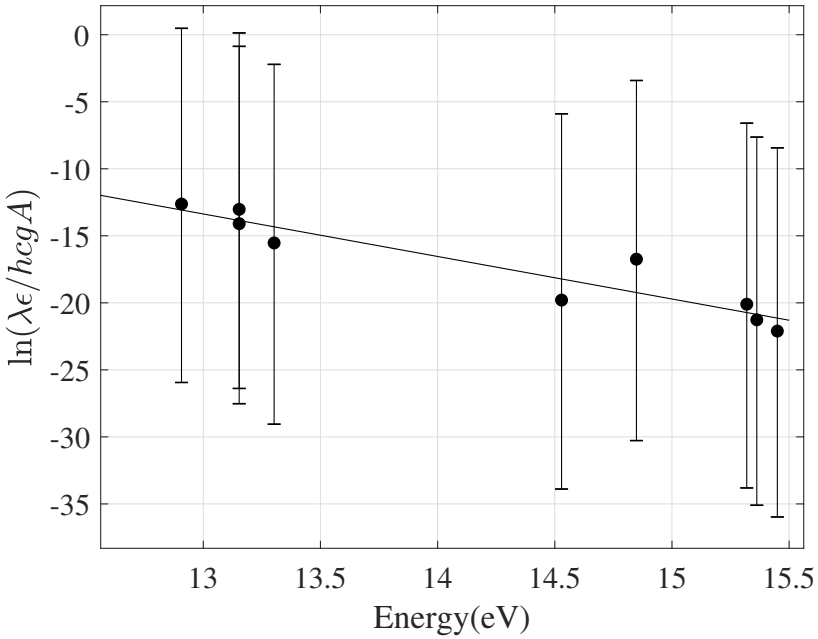

Figure 5.8: Boltzmann plot of the aluminum target magnetron discharge spectrum. Data points are fitted with a linear curve, the slope of this curve is used to find electron temperature.

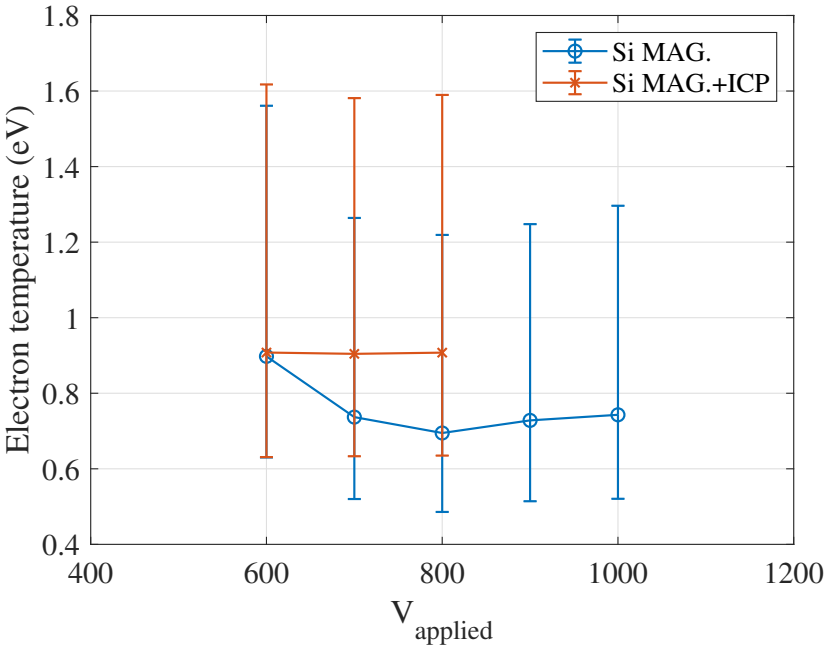

(a)

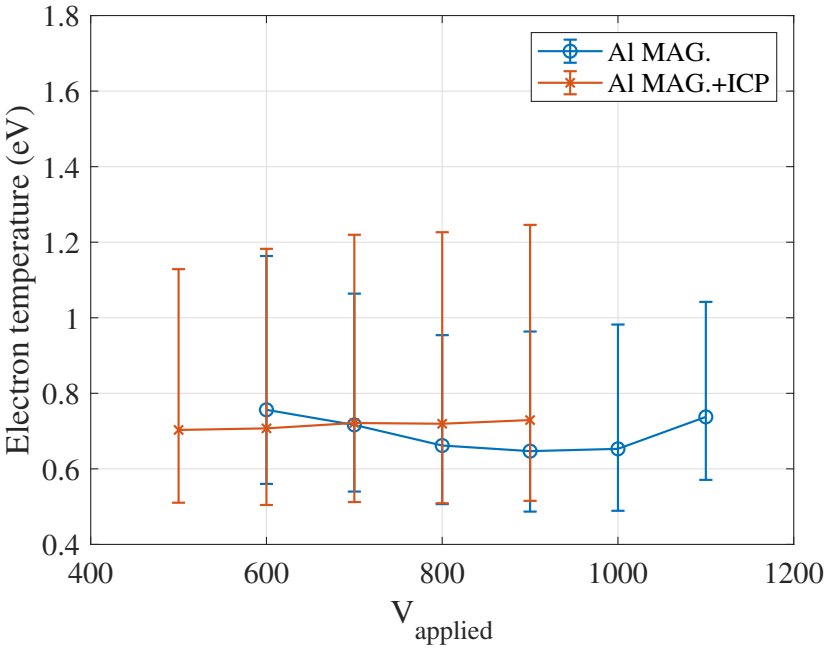

(b)

Figure 5.9: Electron temperature for (a) silicon and (b) aluminum targets at different magnetron discharge voltages, determined via Boltzmann plot of Ar I lines.

5.3 Time Resolved Langmuir Analysis

By varying the voltage applied to the Langmuir probe and recording the current draw over many pulses, a time resolved I-V curve of the magnetron discharge was constructed, see figures 5.10 and 5.11. In these figures we see the secondary ICP discharge has the effect of smoothing the I-V curves and eliminating the spikes that occur at the beginning and end of the pulse. The disruption of the I-V curves seen towards the end of the pulse in figure 5.10 (a) is caused by the voltage overshoot, discussed in section 5.1. The measured electron temperature for discharges with the ICP will be higher than the actual temperature. This is due to the RF power causing the plasma potential to oscillate. What we see is the time-averaged I-V curve, which is more flat, resulting in higher apparent electron temperature.

In figure 5.10 (a), before the start of the pulse at $\sim$40 µs the probe collects a small amount of current, likely due to charged particles left over from the previous pulse. Performing Langmuir analysis of the I-V curves before the pulse, we found the electron density to be $8 \times 10^7/\text{cm}^3$ and the electron temperature to be 10 eV. The magnetron was pulsed at 266 Hz, so the observed afterglow lasted at least 3.76 ms. Similarly, Poolcharuansin and Bradley reported electron densities $\sim 2 \times 10^9/\text{cm}^3$ up to 4000 µs after an HiPIMS pulse, Anders and Yushkov proposed long-lived argon metastable states as an explanation for the plasma after glow [38, 39].

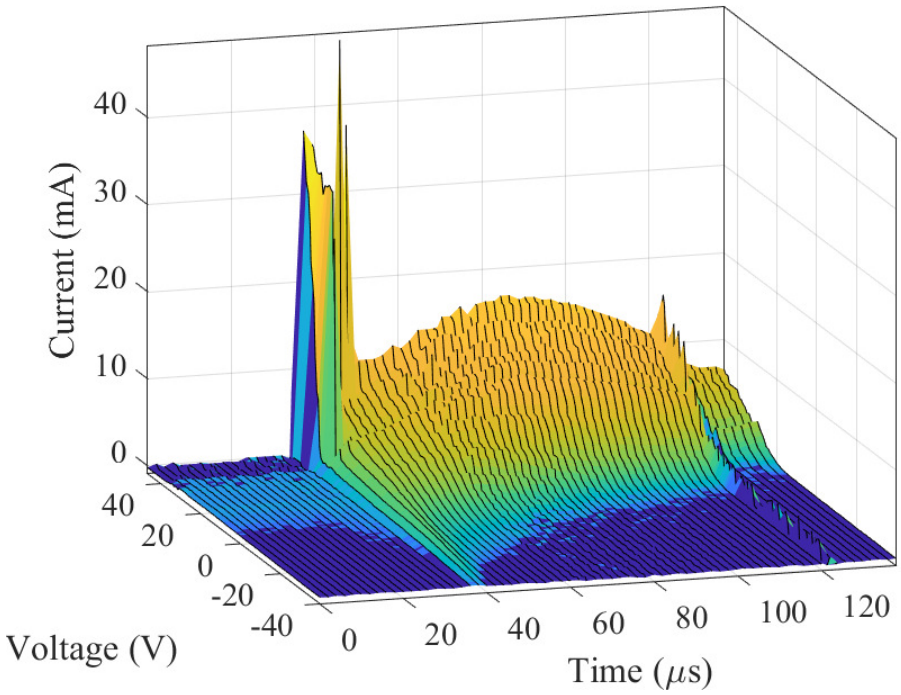

(a)

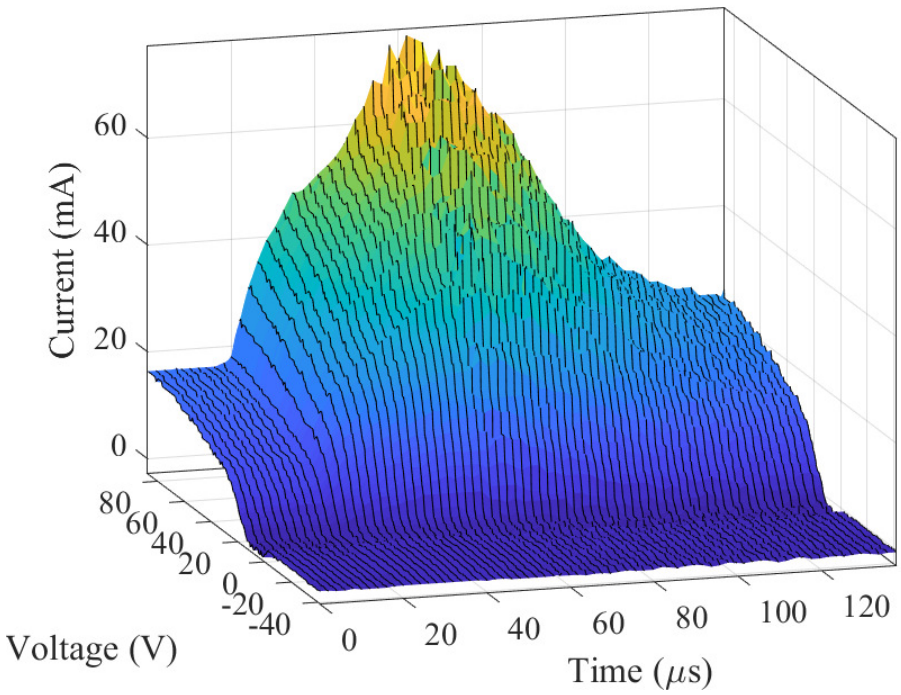

(b)

Figure 5.10: Time resolved Langmuir probe measurement of magnetron discharge for silicon target. (a) Magnetron discharge, (b) magnetron ICP combined discharge. The colour is scaled to the current, to accentuate the topology of the plot. Each black line represents the I-V curve at a specific time.

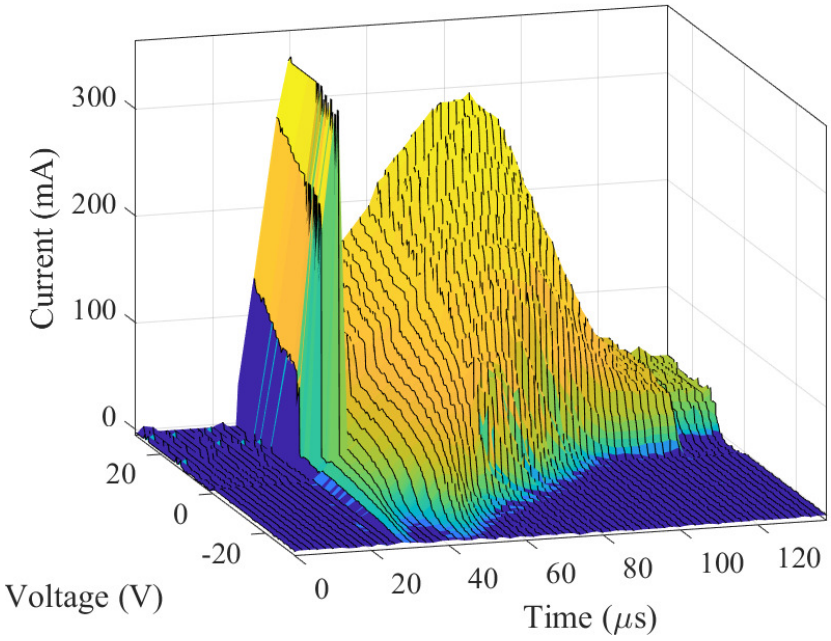

(a)

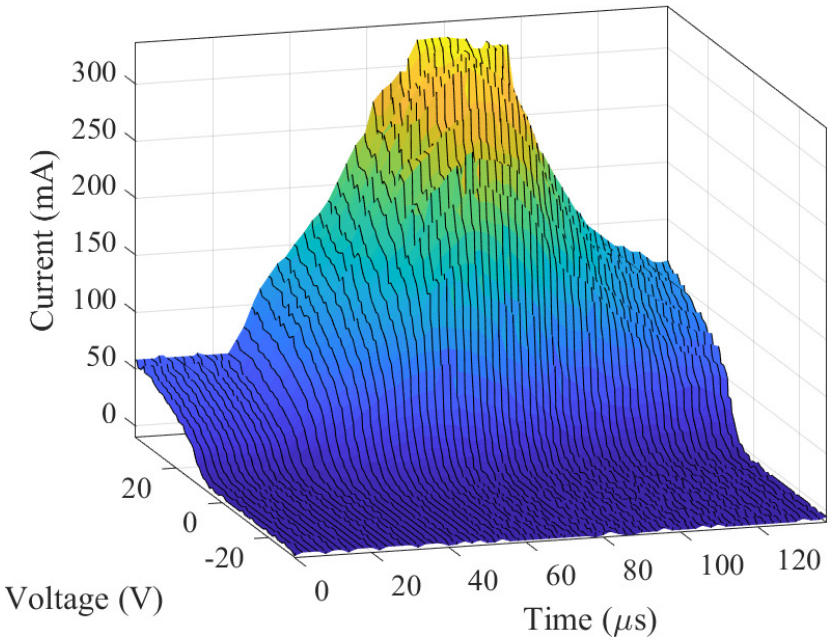

(b)

Figure 5.11: Time resolved Langmuir probe measurement of magnetron discharge for aluminum target. (a) Magnetron discharge, (b) Magnetron ICP discharge.

Performing Langmuir analysis on the IV-curves for each time-step, the time resolved plasma properties are obtained, shown in figures 5.12 and 5.13. In all four figures, the electron and ion densities are seen rising and falling at the same time, indicating ambipolar diffusion. In this case, as the more mobile electrons diffuse away from the ions, an ambipolar electric field is formed, this reduces the electron flux and increases ion flux until a quasineutral state is reached [1]. Ambipolar diffusion results in electrons and ions diffusing at the same rate [1]. The electron and ion densities should be similar to maintain quasineutrality, however, from our analysis we got higher ion densities than electron densities. This is likely due to the resolution of the sense resistor used. In order to measure the entire I-V curve, the sense resistor needed to be small enough so the voltage drop caused by the electron saturation current does not saturate the comparator amplifier. However, a smaller sense resistor results in less voltage drop for the ion saturation region, where the current is orders of magnitudes less than electron saturation. This contributes to the error in measured ion density.

In figures 5.12 and 5.13, a delay is seen between the peak discharge current at the target and the peak ion/electron density at the probe. The Langmuir probe is located 8 cm away from the magnetron target surface. Assuming the different species in the plasma move at the same speed due to ambipolar diffusion, the drift speed of the particles is calculated by dividing the distance from the magnetron to the probe by the delay time. Then knowing the different masses of these particles, their kinetic energies are calculated, shown in table 5.2.

Table 5.2: Delay between electron density peak and peak discharge current, used to calculate speed and energy. Here we assume the charged particles all originate from the cathode and drift towards to probe at constant speed. Particle energy is calculated assuming the same speed for all species.

Discharge	Delay (μs)	Speed (km/s)	Energy$_{argon}$ (eV)	Energy$_{metal}$ (eV)
Al. ICP+MAG.	22	3.6	2.7	1.8
Al. MAG.	45	1.8	0.7	0.5
Si. ICP+MAG.	21	3.8	3.0	2.1
Si. MAG.	46	1.7	0.6	0.4

The calculated ion energies are similar to those found in literature. Poolcharuanisn and

Bradley reported titanium ion energy of 1.6 eV while operating their HiPIMS at 3.75 mtorr [39].

From figures 5.12 and 5.13 we also observe higher overall ion/electron densities with the aluminum target compared with silicon. This could be caused by the difference in sputtering yield and secondary electron yield of the two materials. The sputtering yield for aluminum is 1.2 and for silicon is 0.5 per 600 eV argon atom [40]. As the result of higher ion densities, we see that the electron temperature is lower for the aluminum target. Due to the higher plasma density, the collision rate is higher. This results in the thermalization of electrons, where electrons give up energy in due to collision and subsequent ionization or excitation of sputtered and gas atoms. The reduction of electron temperature due to collisions can be seen in all four figures. When the electron/ion densities increase it causes a decrease in electron temperature.

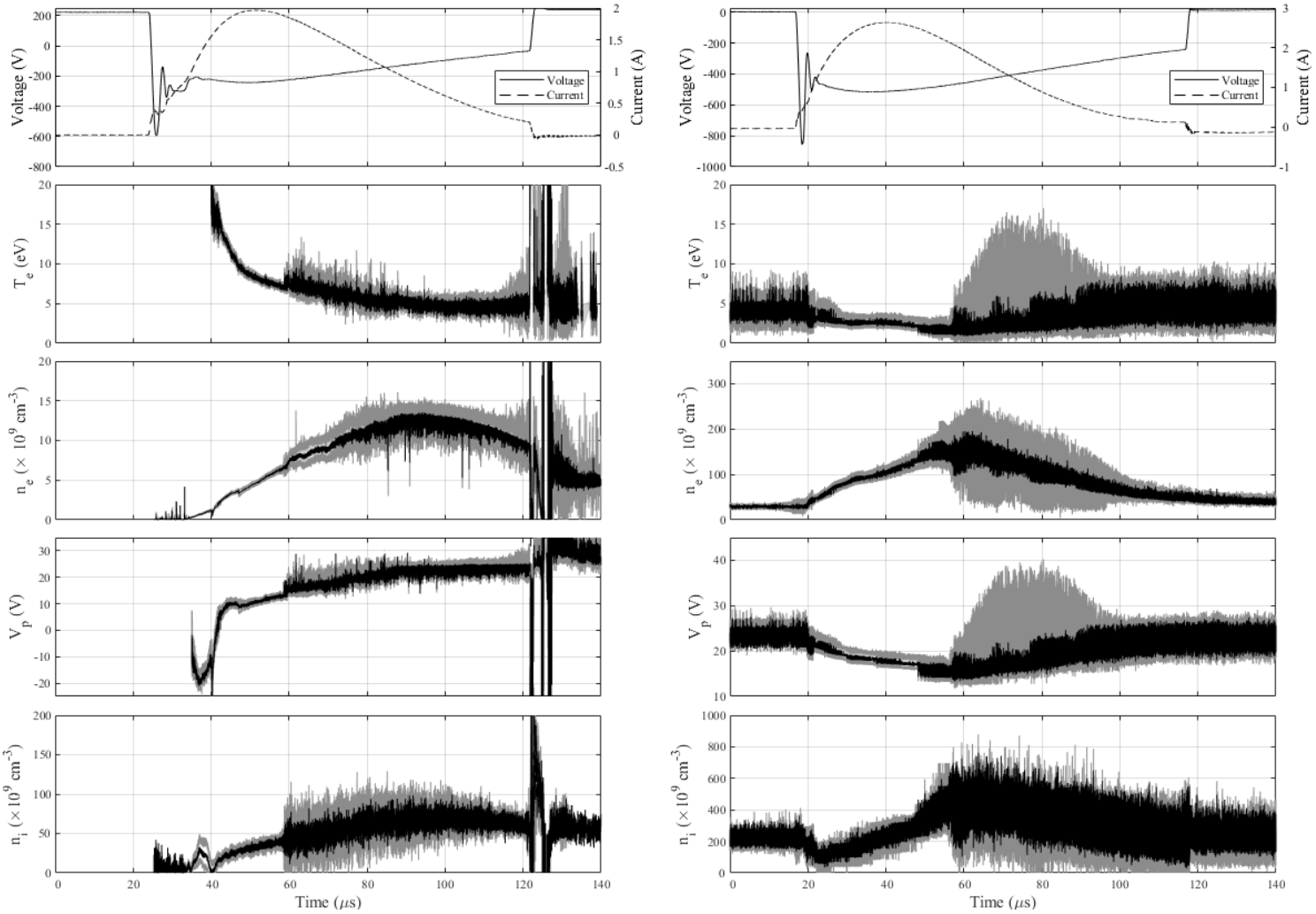

Figure 5.12: Plasma parameters obtained from Langmuir analysis of time resolved curves for a silicon target. (a) Magnetron discharge, (b) Magnetron ICP discharge. The plots from top to bottom are: Discharge waveform, electron temperature, electron density, plasma potential and ion density.

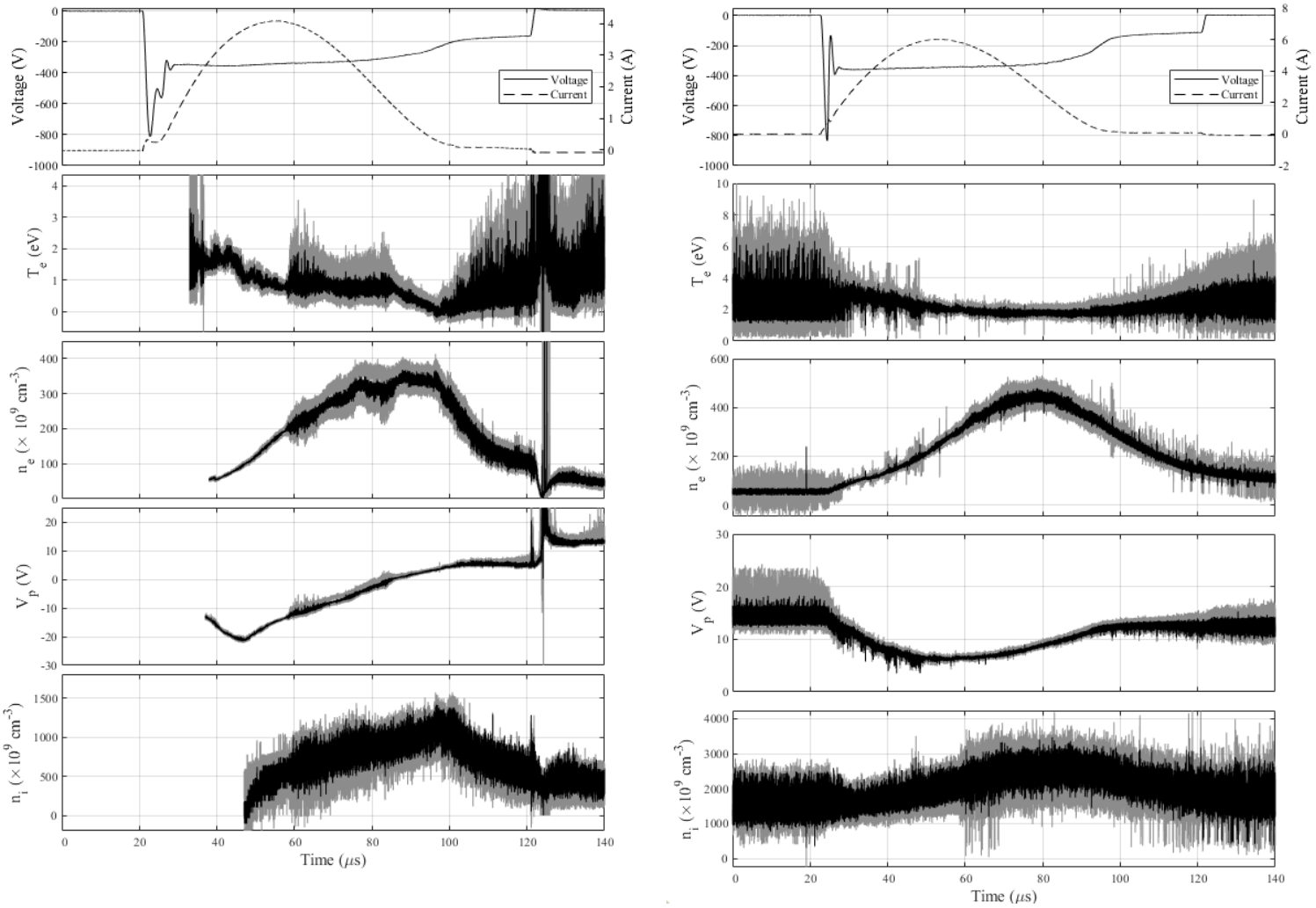

(a) **(b)**

Figure 5.13: Plasma parameters obtained from Langmuir analysis of time resolved curves for an aluminum target. (a) Magnetron discharge, (b) Magnetron ICP discharge. The plots from top to bottom are: Discharge waveform, electron temperature, electron density, plasma potential and ion density.

5.4 Floating Probes

Silicon target magnetron discharge data from the three floating probes were processed using EMD, shown in figure 5.14. The IMFs containing high frequency noise and low frequency DC offsets are discarded and the signal is reconstructed as a summation of the rest of the IMFs. The processed signal shows clear oscillations developing between the initial pulse on and pulse off events.

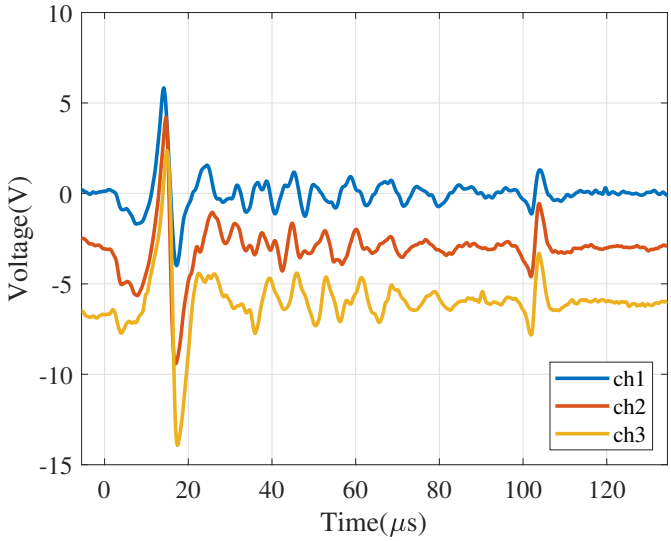

Figure 5.14: EMD processed signal from three floating probes, channels are offset vertically for readability. Periodic fluctuations in floating potential is seen in all three channels throughout the 100 µs discharge.

High-speed camera frames were captured in sync with the floating probe measurements to correlate floating potential to the spoke structure above the target. The frame captured by the camera in figure 5.17 shows a mode 1 spoke with high intensity near probe 2 and its tail located on the other side of the magnetron racetrack. It has been shown in [12], that the area of high intensity measured by a high-speed camera corresponds to an area of high ionization, which produces excess electrons and results in a drop in floating potential near that area. Figure 5.15 shows the signal from the probes at the time of the camera exposure, all three channels are approaching a peak; the signals are offset from each other by a time delay, with probe 1 leading probe 2 by 1 µs and probe 2 leading probe 3 by 1.2 µs. We interpret this as a clockwise rotation (-$\mathbf{E} \times \mathbf{B}$ direction) of the spoke in figure 5.17.

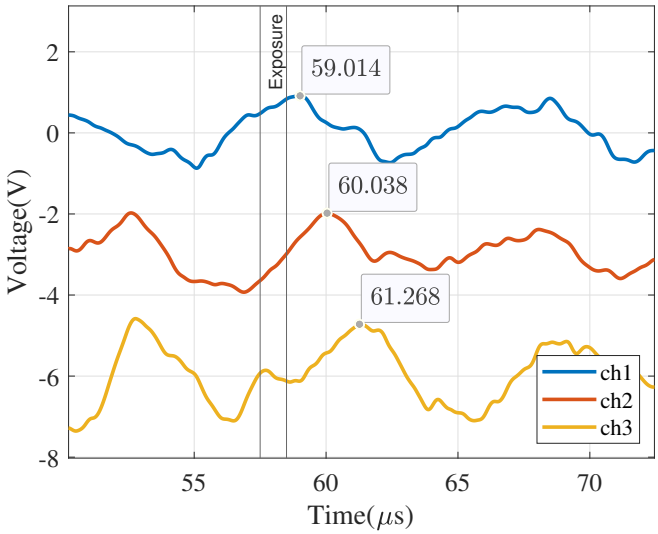

Figure 5.15: EMD Processed probe signals, time of camera exposure indicated by vertical bar; camera frame is shown in figure 5.17 below. Also labeled are the times of the peaks for each channel, showing lag between the probes.

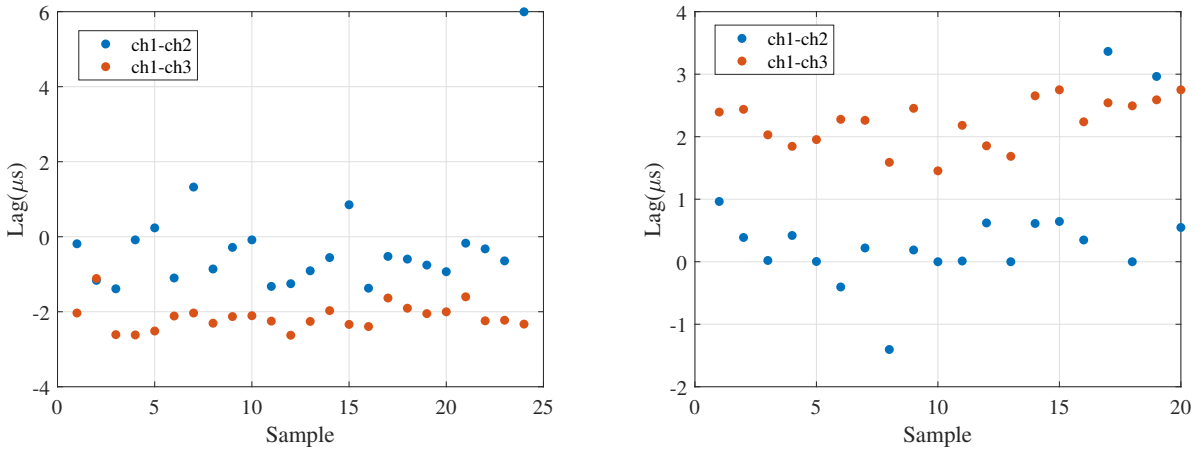

Figure 5.16: Delay time between probe 1 and probes 2 and 3 for (a) silicon target and (b) aluminum target discharge; determined by cross-correlation of probe signals.

To determine the delay between the channels for all samples, we use the cross-correlation function to automate the process, see figure 5.16. The range of the cross-correlation was set to be 35–100 µs, this way the pulse on/off parts of the waveform does not contribute to the results. From figure 5.16, the average delay between probes 1 and 2 for the silicon target is 0.6 µs while the average delay between probes 1 and 3 is 2.2 µs. The racetrack has a perimeter of 60 mm, using the time delay and angle between the probes, the speed of the rotating spoke is found to be 19 km/s. This value is high compared to the values reported in literature which are around 8 km/s [41, 3]. For the aluminum target, the delay average delay between 1 and 2 is -0.3 µs and the average delay between 1 and 3 is -2.3 µs which corresponds to a $\sim$31 km/s counterclockwise rotation. Since we cannot detect spokes changes in the space between the probes have to assume the spokes move in a constant velocity without changing shape or size. In this case we would expect the phase delay between probe 1 and 3 to be twice the delay between 1 and 2 since probe 2 is located in the centre, see figure 5.17. However, we find the phase delay between probes 1 and 2 to be smaller than expected for both targets. This could be due to the stochastic behaviour of the spokes, evolving and changing throughout the pulse, leading to discontinuities between signals observed from each probe.

Figures 5.17 and 5.18 show images of spokes from silicon and aluminum target discharges as recorded by the high-speed camera; this was synchronized with the floating probe measurements. The images show that the spoke structure in the silicon target discharge is more diffuse than the spokes aluminum target. In [12], it was postulated that the sharpness of the spoke is a result of gas rarefaction and insufficient secondary electron production from the bombardment of metal ions. They observed that for materials such as aluminum, with a second ionization energy that is higher than the first ionization energy of argon, the spokes were sharp and localized. For materials such as titanium, with with a second ionization energy that is lower than the first ionization energy of argon, the spoke appeared more diffuse. In our observation we find aluminum to have sharper spokes than the silicon target, however, in this case it is likely due to the lower discharge power for the silicon target, resulting in less gas rarefaction, as discussed in section 5.1.

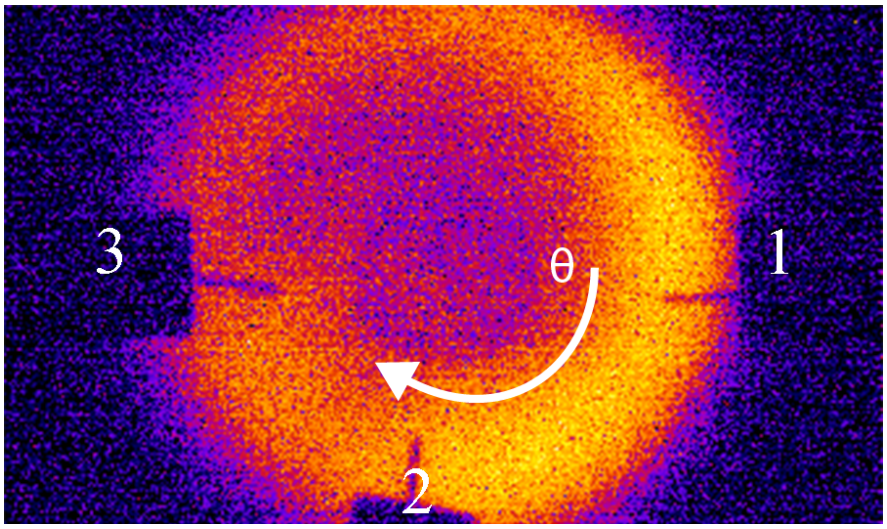

(a)

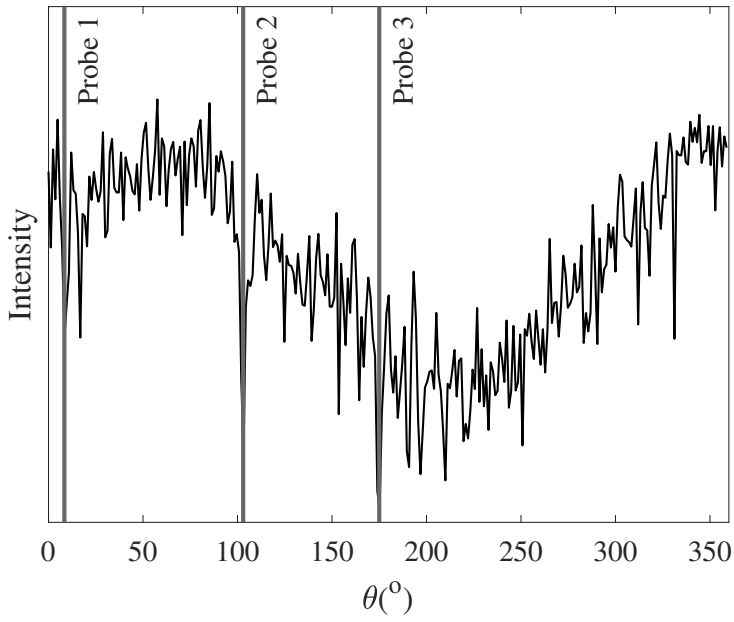

(b)

Figure 5.17: High speed camera measurements for silicon target magnetron discharge. Timing of this exposure with respect to the probe measurements is shown in figure 5.15 above. (a) False colour high-speed camera footage, locations and number of probe labeled in white. (b) Intensity (arbitrary units) of image along circular path over racetrack.

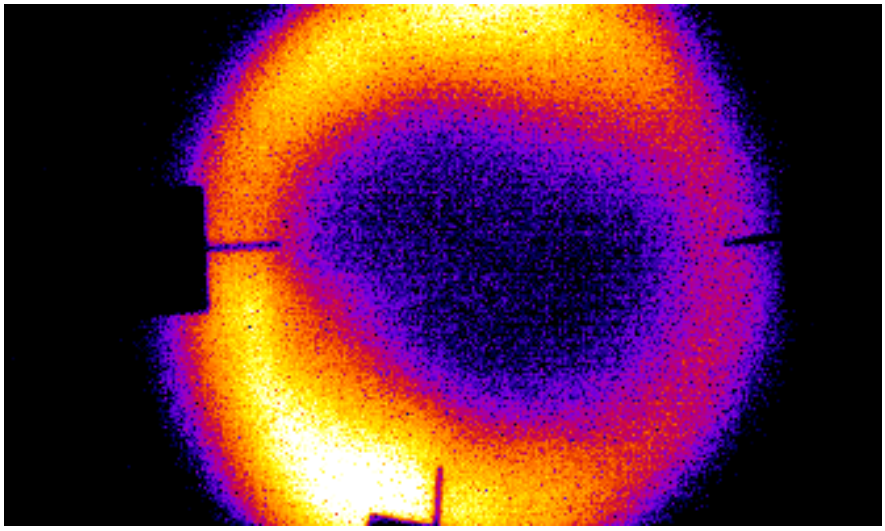

(a)

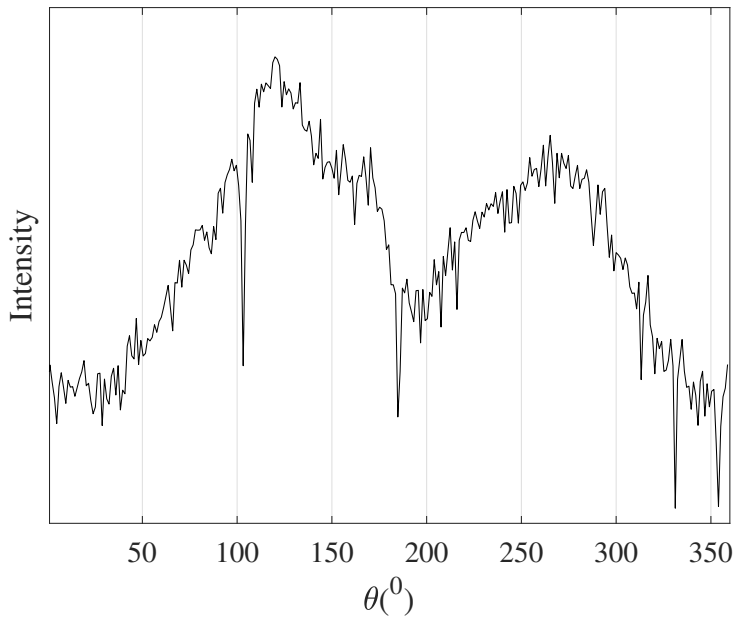

(b)

Figure 5.18: (a) High speed camera footage for aluminum target magnetron discharge, (b) pixel intensity (arbitrary units) of above image azimuthally along the circular racetrack. The structure of the plasma observed here has noticeably sharper edges than in figure 5.17.

5.5 High-speed Camera

Using the high-speed camera, footage of the discharge was collected over many pulses, this footage was processed in MATLAB to obtain quantitative results for the evolution of the discharge, see figure 5.19. By adjusting the image contrast and brightness and applying morphological functions as discussed in section 4.4, we obtain a binary image where the local maxima is isolated, this corresponds to the spoke in the discharge.

The trigger signal to control the camera was adjusted to record images from different times during the discharge. An image sequence can then be constructed to show the evolution of the plasma, see figure 5.20. Each frame represents one of 200 total frames captured at a certain time step.

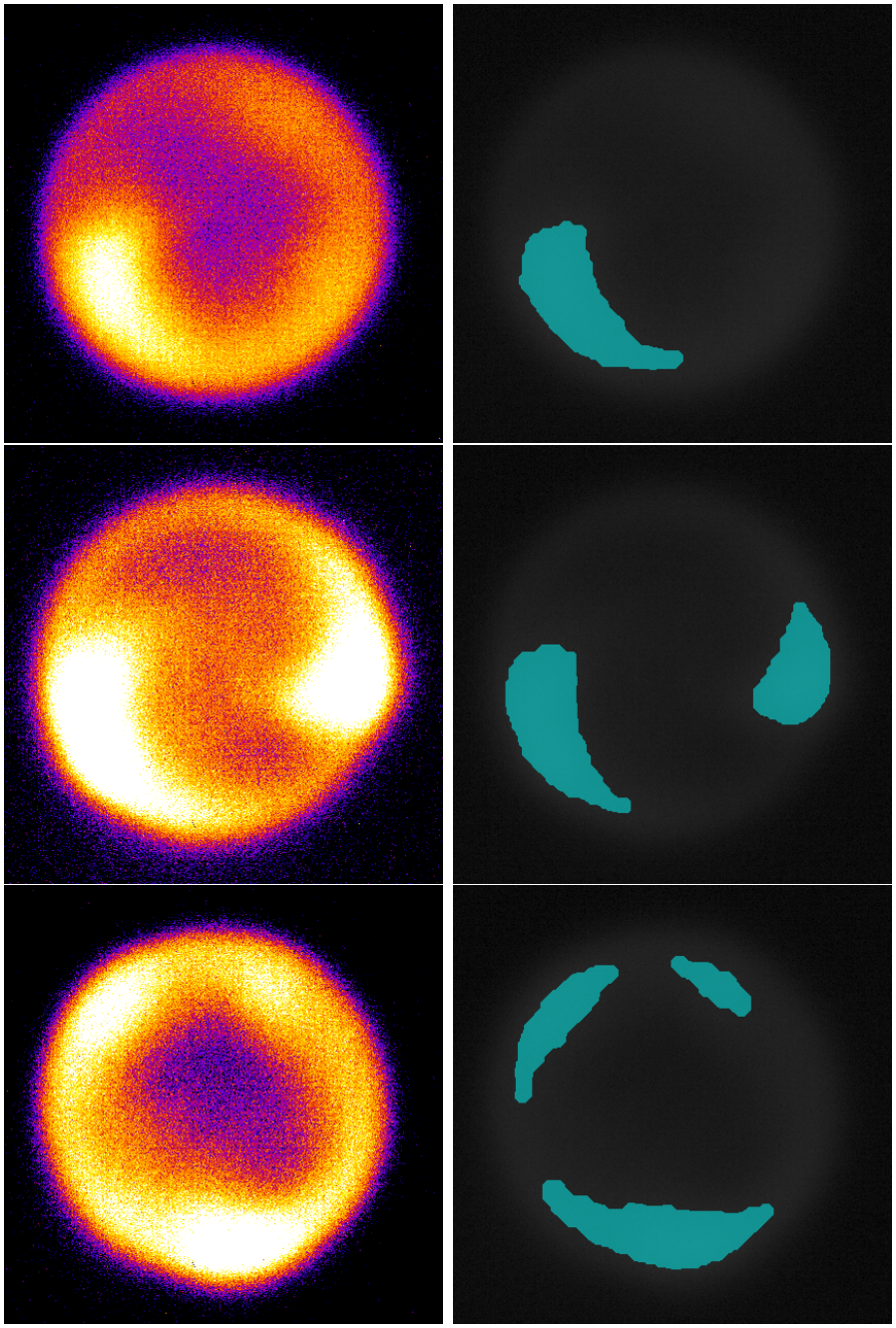

(a) **(b)**

Figure 5.19: Silicon target HiPIMS discharge captured by High-speed camera. (a) false colour high-speed camera frames, (b) the same frames processed in MATLAB to identify the size and number of maximums in the image, overlaid on top of the original image.

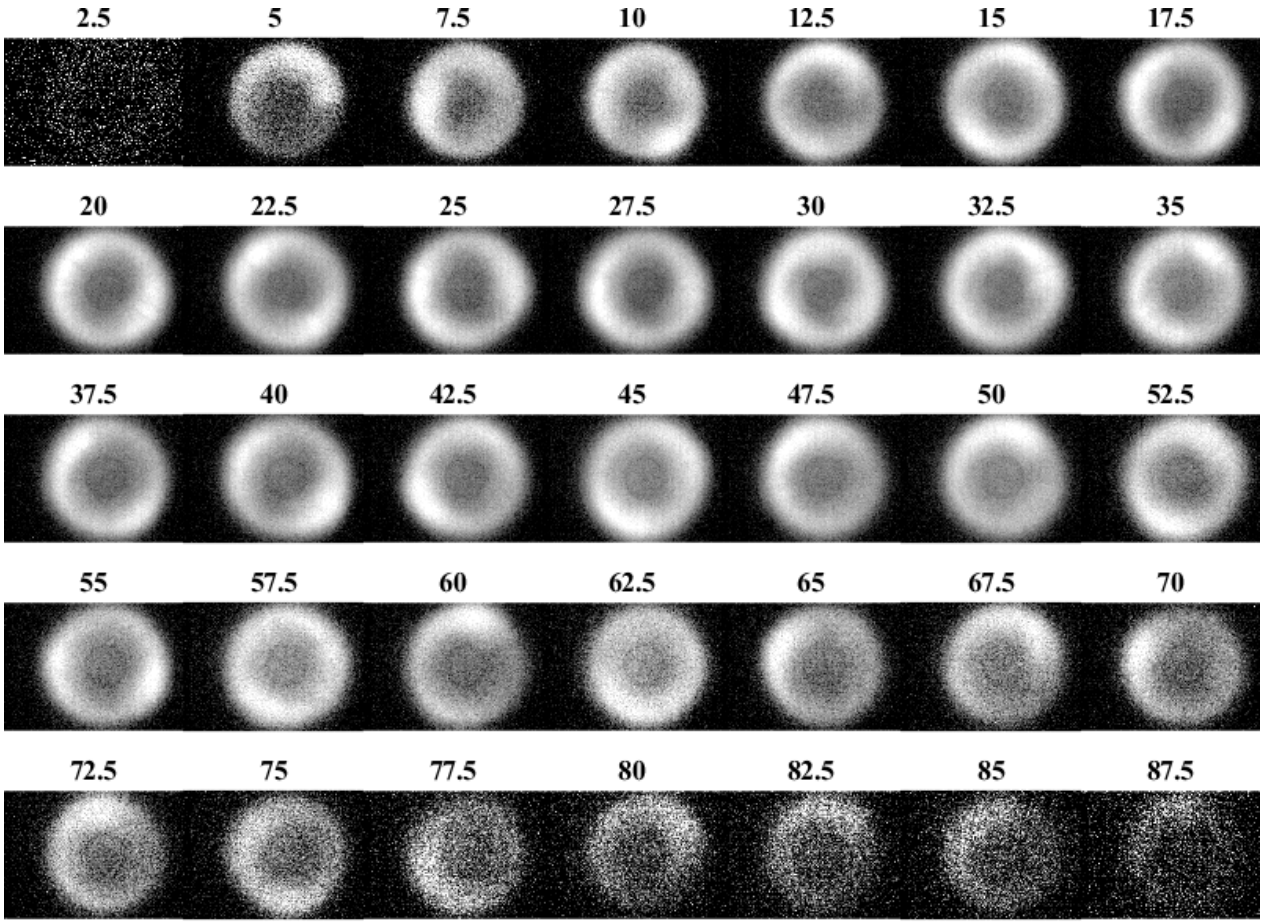

Figure 5.20: Reconstructed time evolution of silicon target magnetron discharge. Above the frames are timestamps in units of μs with respect to the start of the pulse. Brightness was boosted to saturate the brightest pixel in each frame; more noise is seen at the start and end of the pulse due to a low signal-to-noise ratio.

In figure 5.21, four different discharge cases are shown: silicon target with and without ICP and aluminum target with and without ICP. The silicon target with ICP and the both aluminum target discharges share similar power waveforms, and we also see similar average mode numbers for the three pulses. Specifically, the average mode number rises quickly to 1.5 at the beginning of the pulse and falls off quickly just before 80 µs. The silicon target, magnetron only discharge is at a lower discharge power than the other three cases and exhibits a different power waveform. Correspondingly, the average number of modes observed throughout the pulse decreases faster. Previous studies have shown the mode number to be independent of discharge power for pressures below 2 mtorr, above which, the mode number increases with discharge power [13]. Our data shows the number of modes does not follow the discharge power exactly, we see that once the power reaches a certain point, the average number of modes is stable around 1.5, despite further increases in power.

The average intensity of the spoke during the discharge is shown in figure 5.22. The discharge current is correlated to the ionization rate, which relates to the emission of light. As expected, a correlation between the intensity of the spoke and the discharge current is observed.

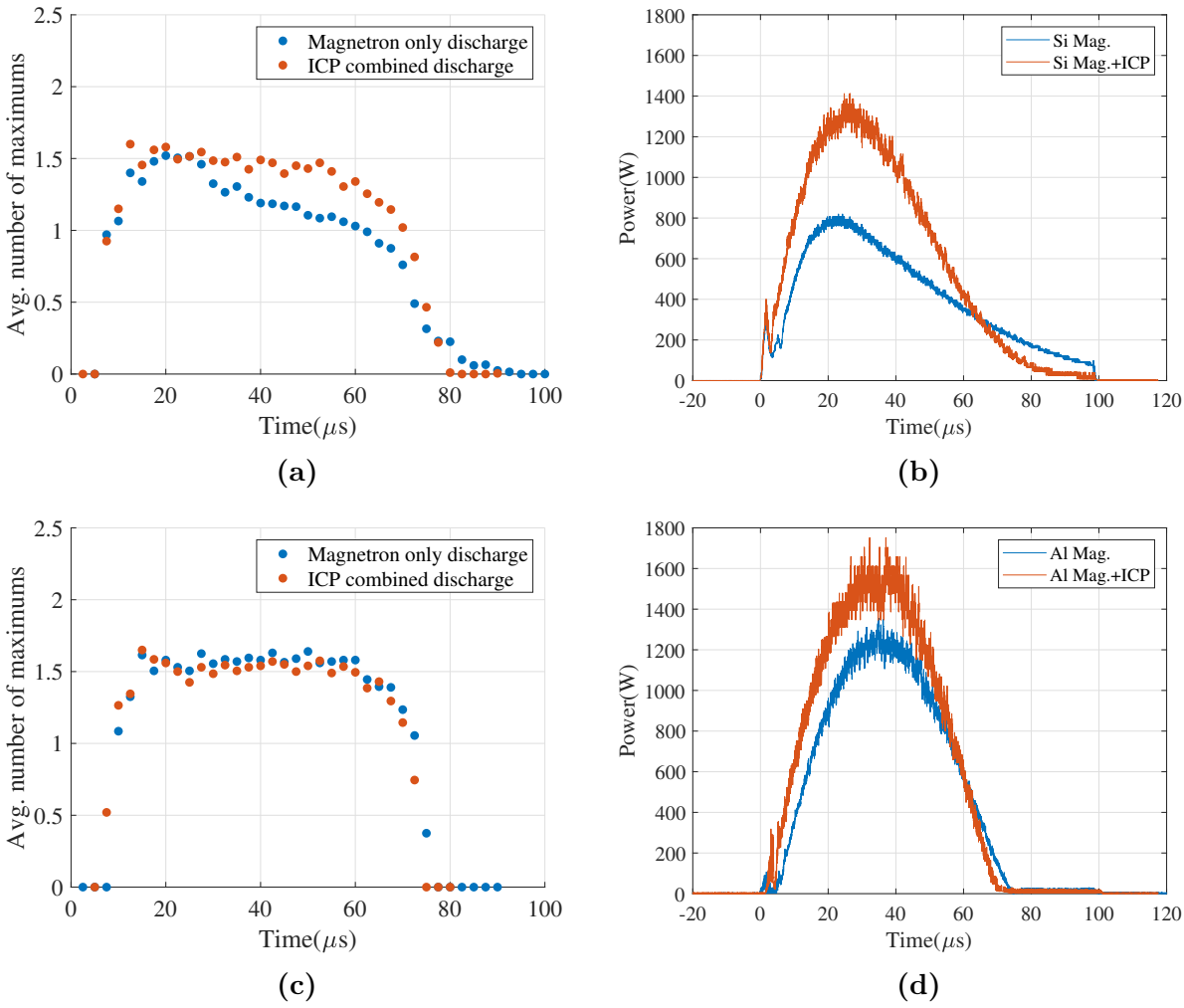

Figure 5.21: Average number of spokes observed by high-speed camera during the discharge for (a) silicon target, (c) aluminum target and the discharge power for (b) silicon target and (d) aluminum target. The average number of spokes increases with discharge power until reaching 1.5, where it remains stable until the end of the pulse. In the case of the silicon target magnetron discharge in (a), the average number of spokes gradually decreases throughout the pulse, then quickly drops off near 70 µs.

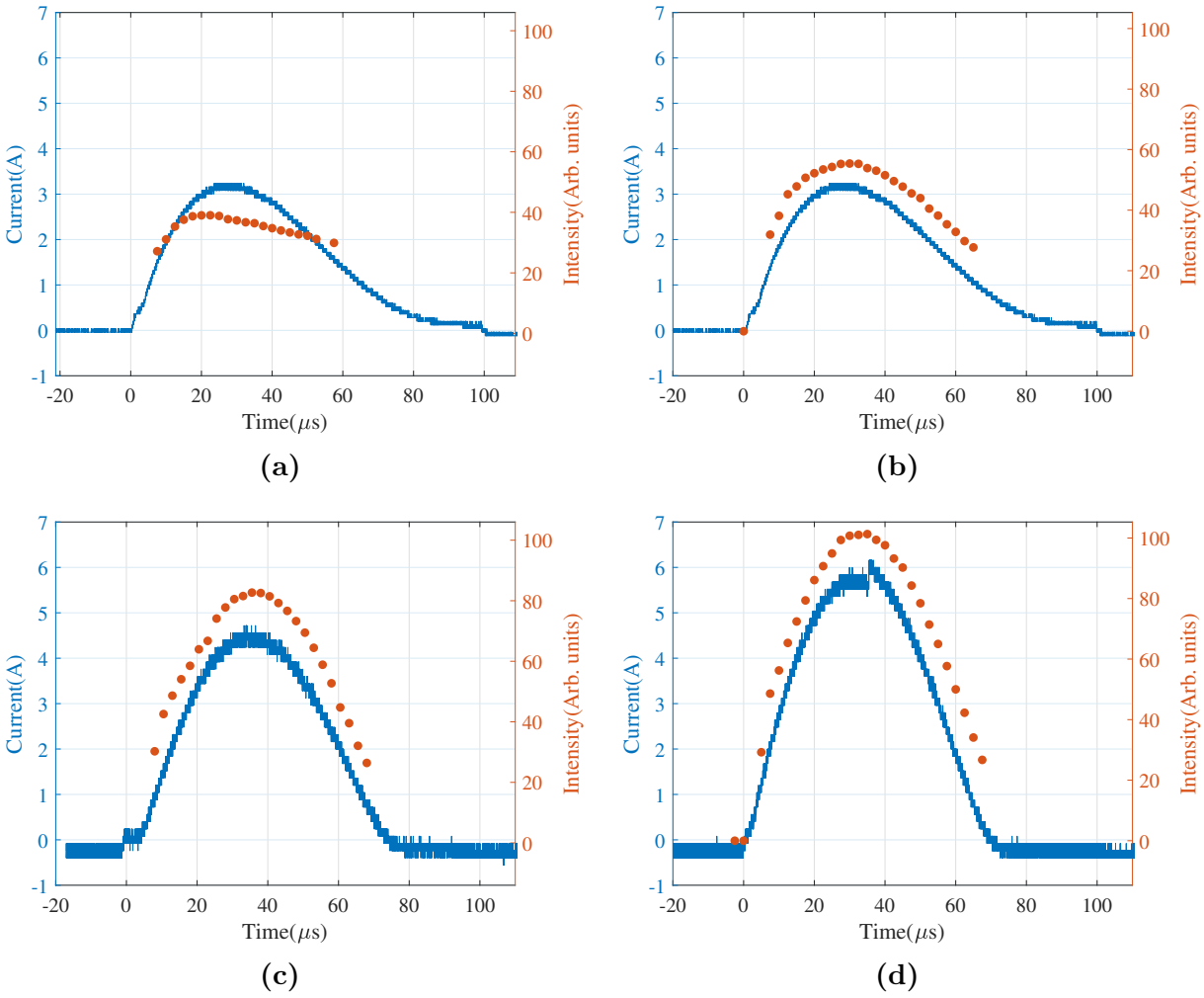

Figure 5.22: Spoke brightness plotted with discharge current. (a) Silicon target, (b) silicon target with secondary ICP discharge, (c) aluminum target, (d) aluminum target with ICP discharge.

The size distributions of the observed spokes are shown in figures 5.23 and 5.24. The size distributions for mode 1 spokes all feature two peaks, the second peak is most prominent in the case of the silicon target with no ICP. This second peak is caused by large diffuse spokes, which were mostly observed at the beginning of the pulse, before the plasma forms into distinct structures and near end, as the plasma is dissipating. The low power of the silicon target with no ICP experiences less gas rarefaction and therefore has more diffuse spokes, this is consistent with the observations in section 5.4. From the size distribution of mode 2 spokes, we can see that smaller spokes are observed more frequently than in mode 1 spokes, this is most evident in figure 5.24 (a) and (b). In [3], it was proposed that in the case of two spokes they compete with each other for argon gas, as one grows, it causes more gas rarefaction which causes the other spoke to decrease in size, this would produce the smaller spokes we see in the distribution. Out of the four mode 2 size distributions, the smaller spokes are least evident in the silicon target discharge with no ICP, I propose this is due to the abundance of argon gas, reducing the competition between the two spokes, so the spokes can both maintain their sizes. The average spoke size over time is shown in figure 5.25. The spoke size follows a similar path to the discharge current, which implies constant current density throughout the pulse. The current literature discussions on spoke size have shown varying current densities as a result of changes in the charge carrier due to self-sputtering [42]. In [43] Hecimovic reports a relationship between spoke current density and discharge voltage of $j \sim V_d^{1.6}$. We were unable to achieve self-sputtering using our power supply, it would be an interesting future project to investigate the spoke current density during a pulse with the onset of self-sputtering.

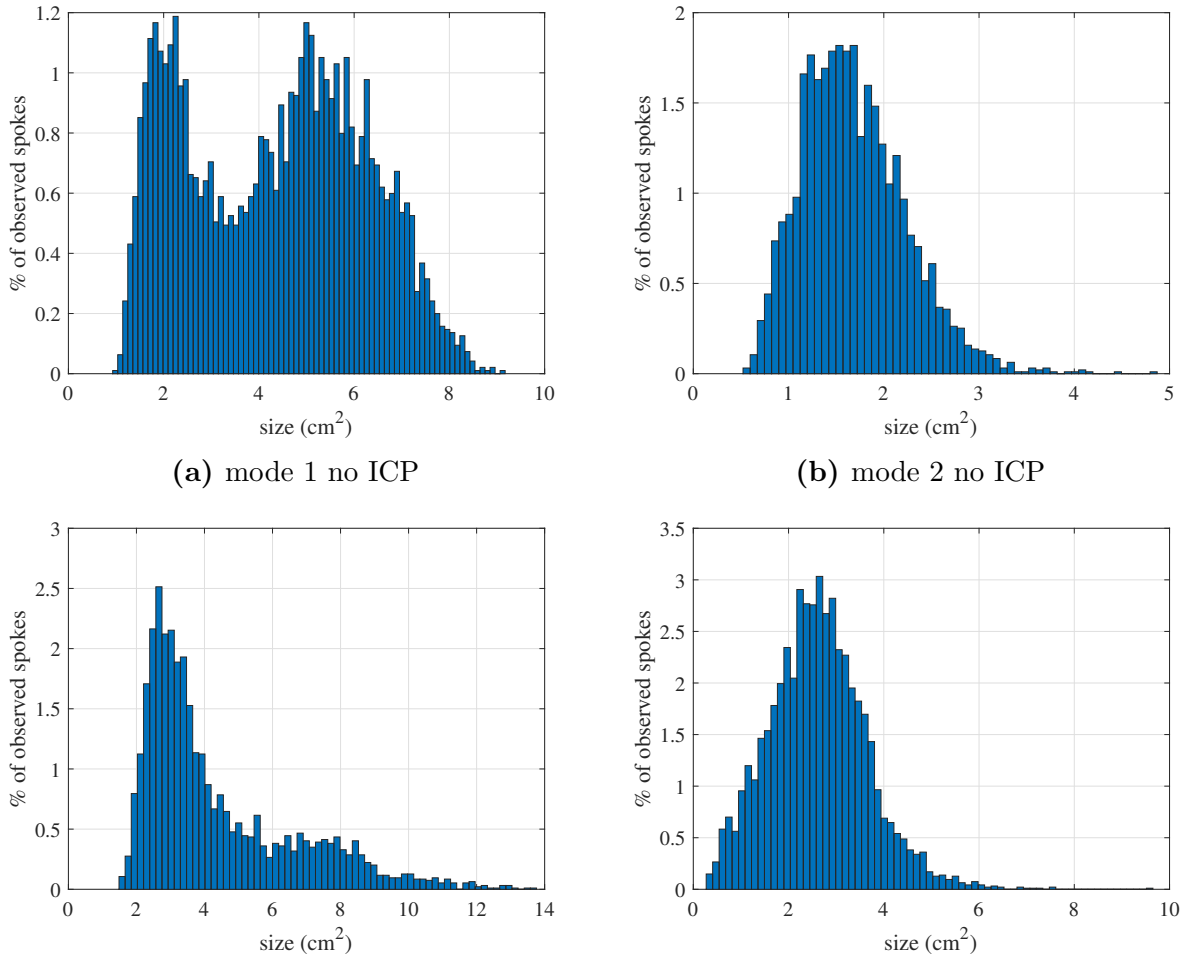

(a) mode 1 no ICP

(b) mode 2 no ICP

(c) mode 1 with ICP

(d) mode 2 with ICP

Figure 5.23: Silicon target spoke size distribution for mode 1 and 2 spokes. The second peak seen in (a) is greatly diminished when a secondary ICP discharge is introduced in (c).

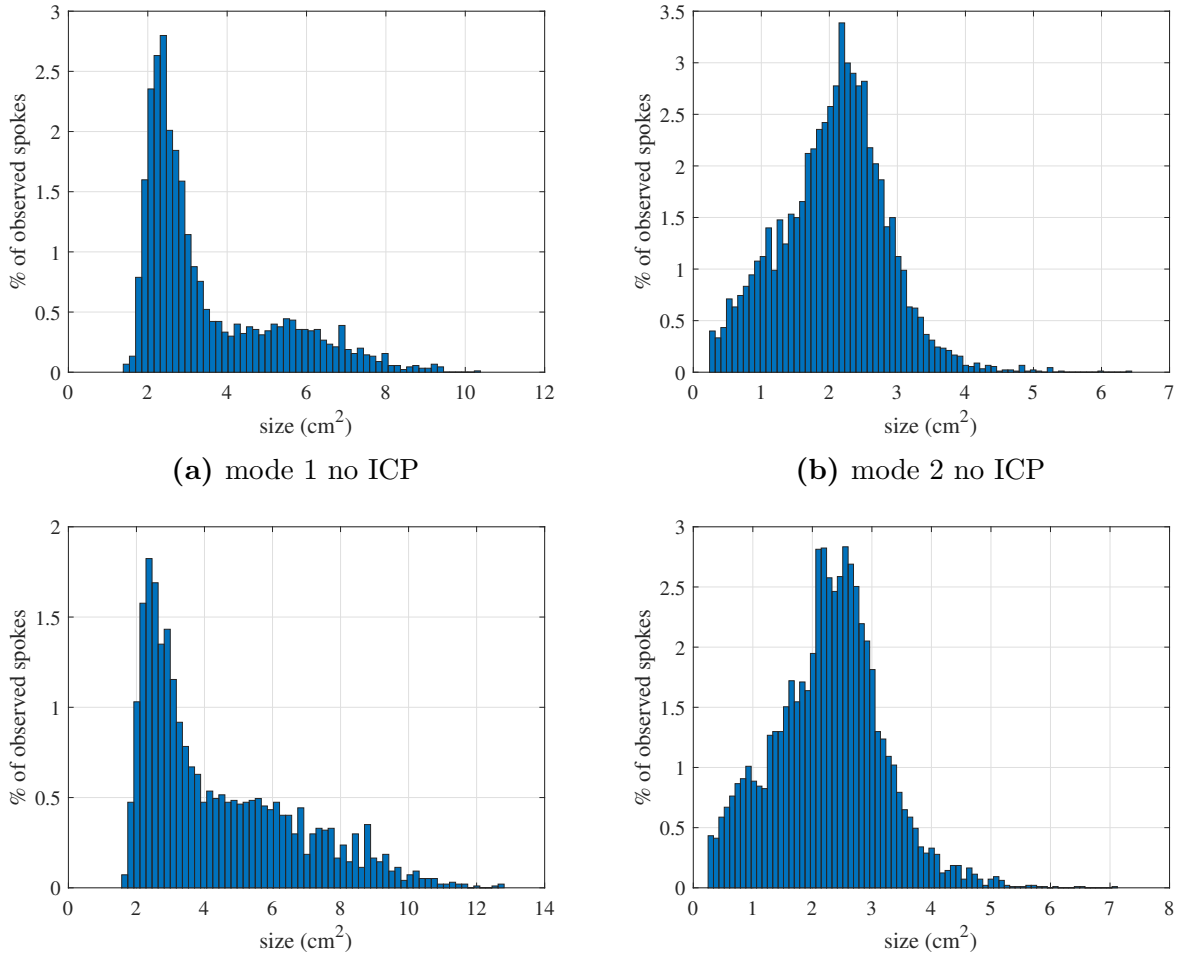

(a) mode 1 no ICP

(b) mode 2 no ICP

(c) mode 1 with ICP

(d) mode 2 with ICP

Figure 5.24: Aluminum target spoke size distribution for mode 1 and 2 spokes.

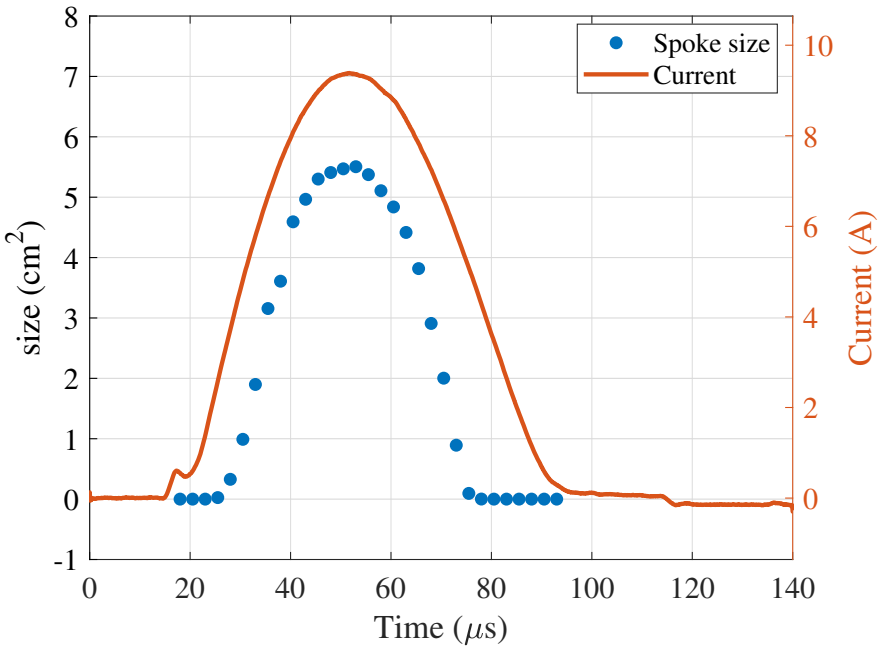

Figure 5.25: Average spoke size and discharge current for aluminum target magnetron discharge.

5.6 Arcing

Arcing was observed on the target surface when the applied voltage exceeded a certain point, an image captured by the high-speed camera of an arcing event is shown in figure 5.26. The electrons released from the arc discharge creates an ionization zone which seems to travel in the $\mathbf{E} \times \mathbf{B}$ direction. Here, the camera period was 300 µs, arcing events only appeared in one frame at a time.

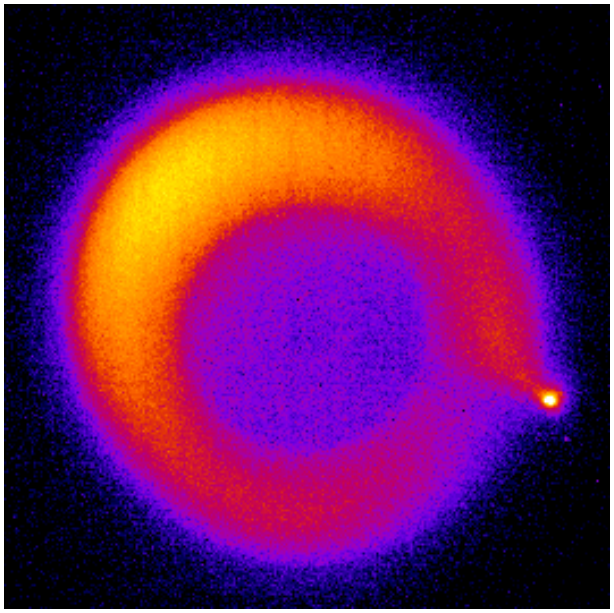

Figure 5.26: Aluminum target magnetron arc during discharge, captured using high-speed camera. The localized bright spot is the location of the arc, where the local electric field became strong enough to cause an explosive discharge event. Increased ionization caused by the release of electrons in the arc event seems to travel in the counterclockwise ($\mathbf{E} \times \mathbf{B}$) direction.

The ignition points were located along the outside of the magnetron racetrack and in the centre of the target, see figure 5.27. The surface of the racetrack remains undamaged, but along the inside and outside edges the surface is pitted with craters from arcing. It was observed that the addition of a secondary ICP discharge reduced the arcing and allowed the magnetron to be operated at lower power.

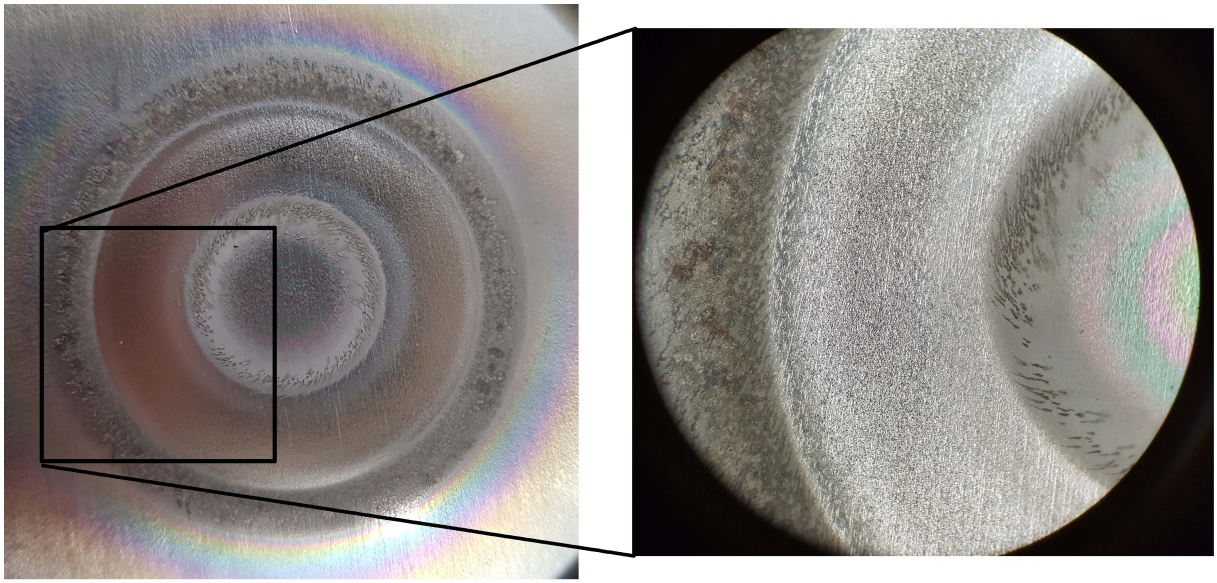

Figure 5.27: Aluminum target surface damage due to arcing. (a) Entire racetrack, (b) 4× magnification.

6 Conclusion

In this thesis, we presented the design and fabrication of an HiPIMS system, with characterization of the plasma focusing on the spoke phenomenon. The following methods were used to characterize the general operation of the magnetron:

- The discharge waveform of the magnetron was observed at different discharge voltages and and pulse lengths. A 7 µs delay was observed at the initiation of the magnetron discharge as the plasma formed. This delay became less pronounced with the addition of a secondary ICP discharge, due to the additional seed of ionized gas. Furthermore, the ICP tended to increase the discharge power, and leading to a more symmetrical discharge current waveform. This was due to increased rarefaction of the background gas, which eventually slowed further increases in discharge power. The current waveforms did not show the characteristic second peak caused by self-sputtering for the discharge powers attempted. In the project we were unable to explore higher power discharges due to limitations of our high-voltage pulser.

- A custom optical system was assembled to perform optical emission spectroscopy on the magnetron plasma. Lines from neutral and singly ionized aluminum were observed, but no silicon lines were observed. Electron temperature was successfully obtained using the Boltzmann plot method. The variation of discharge voltage was shown to have little effect on the electron temperature. The accuracy of our results were limited by the 1 nm resolution of our spectrometer.

- The magnetron plasma parameters were obtained using a time-resolved Langmuir probe system. By comparing the electron and ion densities, we saw they changed in sync and confirmed the charged particles were following ambipolar diffusion. Then by comparing time difference between the peak current and the peak density, the speed of this

diffusion was calculated to be in the range of km/s, which agreed with literature values. The Langmuir probe measurements also showed presence of a plasma afterglow, up to 3 ms after the magnetron discharge, which is from long lasting argon metastable states. Furthermore, the Langmuir analysis showed an inverse relation between electron temperature and plasma density. This was a result of electrons losing their energies due to increased ionization and excitation of ions and neutrals.

Spoke instabilities were observed in the operation of our custom magnetron. A novel characterization method was developed to study the properties of these spokes:

- Three floating probes were placed radially around the magnetron racetrack to observe the fluctuating floating potential caused by the spokes. After processing the signal using EMD methods, we observed a noticeable phase delay between the three probes on the scale of microseconds. Using cross-correlation to determine the phase delay between the signals, the rotation speed of the spokes were determined to be $-19\,\mathrm{km/s}$ and $31\,\mathrm{km/s}$ in the $\mathbf{E} \times \mathbf{B}$ direction for the silicon and aluminum targets respectively. This was higher than the reported values in literature. Our observations of the fluctuating floating potential suggests the characteristics of the spokes are changing in such a way that our probes do not have the angular resolution to observe. So we see discontinuities in the signals between the different probes.

- A high-speed camera was used to collect images of spokes over multiple pulses to construct an statistical picture of the stochastic spokes. We observed the average spoke number evolving in conjunction with the discharge power throughout the pulse. Furthermore, we observed that once the discharge power reached a high enough threshold, the mode number remained stable around 1.5. From the images of the spokes we saw the spokes from the aluminum target having sharper borders than the silicon target spokes. We referred to existing literature and proposed this was a result of higher gas rarefaction in the aluminum target discharge. We then obtained the size distributions of the spokes for the different discharge conditions. The lower power discharge, had a broader distribution of spoke sizes for mode 1 spokes due to the formation of more diffuse spokes. Whereas, in higher power discharges, the gas rarefaction reduced the

sizes of observed spokes. For mode 2 spokes, we observed the lower power discharges had a smaller variance in spoke sizes while the higher power discharges had a relatively larger distribution of spoke sizes. We claimed this was due to more availability of background gas in low power discharges to sustain the two spokes while in a higher power discharge. The lack of background gas causes the two spokes to compete, leading to smaller spokes being formed.

Future studies could investigate axial or breathing mode instabilities in the magnetron plasma, using a similar floating probe and camera setup but with the camera setup to view the discharge from the side. The camera could be used to determine the axial evolution of the spokes similar to how the azimuthal evolution was studied here. Furthermore, if a more powerful high-voltage pulser could be obtained, the higher power regimes of the HiPIMS discharge could be investigated. There we could observe the effects of self-sputtering on the evolution of the spokes.

References

[1] A. Piel. *Plasma Physics: An Introduction to Laboratory, Space, and Fusion Plasmas (Second Edition)*. Springer International, Cham, Switzerland, 2017.

[2] P. Kelly and R. Arnell. Magnetron sputtering: a review of recent developments and applications. *Vacuum*, 56(3):159–172, 2000.

[3] A. Hecimovic. Spokes in High Power Impulse Magnetron Sputtering Plasmas. *Journal of Physics D: Applied Physics*, 51(45), 2018.

[4] F. Chen. *Introduction to Plasma Physics and Controlled Fusion (Third Edition)*. Springer International, Cham, Switzerland, 2016.

[5] R. J. Goldston and P. H. Rutherford. *Introduction to Plasma Physics*. Taylor & Francis Group, New York, NY, USA, 1995.

[6] M. Lieberman and A. Lichtenberg. *Principles of Plasma Discharges and Materials Processing (Second Edition)*. John Wiley & Sons, Hoboken, New Jersey, 2005.

[7] J. Gudmundsson, N. Brenning, D. Lundin, and U. Helmersson. High power impulse magnetron sputtering discharge. *Journal of Vacuum Science & Technology*, 30(3), 2012.

[8] S. Swann. Magnetron Sputtering. *Physics in Technology*, 19(67), 1988.

[9] N. Brenning, D. Lundin, T. Minea, C. Costin, and C. Vitelaru. Spokes and charged particle transport in hipims magnetrons. *Journal of Physics D: Applied Physics*, 46(8):084005, 2013.

[10] A. Hecimovic. Anomalous cross- b field transport and spokes in hipims plasma. *Journal of Physics D: Applied Physics*, 49(18):18LT01, 2016.

[11] A. Anders and Y. Yang. Direct observation of spoke evolution in magnetron sputtering. *Applied Physics Letters*, 111(6), 2017.

[12] A. Hecimovic, M. Böke, and J. Winter. The characteristic shape of emission profiles of plasma spokes in hipims: the role of secondary electrons. *Journal of Physics D: Applied Physics*, 47(10):102003, 2014.

[13] J. Hnilica, P. Klein, M. Šlapanská, M. Fekete, and P. Vašina. Effect of magnetic field on spoke behaviour in hipims plasma. *Journal of Physics D: Applied Physics*, 51(9):095204, 2018.

[14] D. Mattox. *Handbook of Physical Vapor Deposition (PVD) Processing*. Elsevier, Kidlington, Oxford, 2010.

[15] Handbook of basic atomic spectroscopic data. `https://www.nist.gov/pml/handbook-basic-atomic-spectroscopic-data`. accessed 2020-3-19.

[16] U.S. Department of the Interior and U.S. Geological Survey. MINERAL COMMODITY SUMMARIES 2019. *U.S. Geological Survey*.

[17] L.J. Salerno, J. Gaby, R. Johnson, P. Kittle, and E.D. Marquardt. *Terrestrial Applications of Zero-Boil-Off Cryogen Storage. In: Ross R.G. (eds) Cryocoolers 11*. Springer, Boston, MA, 2002.

[18] P. Haussinger, R. Glatthaar, W. Rhode, H. Kick, C. Benkmann, J. Weber, H. J. Wunschel, V. Stenke, E. Leicht, and H. Stenger. *Ullmann's Encyclopedia of Industrial Chemistry*. Wiley-VCH Verlag GmbH & Co. KGaA, 2001.

[19] University of Nevada, Las Vegas, Agreement Information 6238. `https://www.unlv.edu/purchasing/agreements6238`. accessed 2020-10-6.

[20] A. Anders. Physics of arcing, and implications to sputter deposition. *Proceedings of the 5th ICCG, Saarbruecken*, 2003.

[21] A. Anders, J. Čape, M. Hála, and L. Martinu. The 'recycling trap': a generalized explanation of discharge runaway in high-power impulse magnetron sputtering. *Plasma Sources Science and Technology*, 45(1):012003, 2012.

[22] N. Schmidt, T. Totushek, W. Kimes, D. Callender, and J. Doyle. Effects of substrate temperature and near substrate plasma density on the properties of dc magnetron sputtered aluminum doped zinc oxide. *Journal of Applied Physics*, 94(5514), 2003.

[23] J. Hopwood. Review of inductively coupled plasmas for plasma processing. *Plasma Sources Science and Technology*, 1(2):109–116, 1992.

[24] B. B. Sahu, J. G. Han, J. B. Kim, M. Kumar, S. Jin, and M. Hori. Study of Plasma Properties for the Low-Temperature Deposition of Highly Conductive Aluminum Doped ZnO Film Using ICP Assisted DC Magnetron Sputtering. *Plasma Processes and Polymers*, 13(1):134–146, 2016.

[25] F. Chen. Lecture notes on langmuir probe diagnostics. `http://www.seas.ucla.edu/~ffchen/Publs/Chen210R.pdf`, June 2003. accessed 2020-5-1.

[26] H. Kunze. *Introduction to Plasma Spectroscopy*. Springer-Verlag Berlin Heidelberg, Heidelberg, Germany, 2009.

[27] C. Aragon and J.A. Aguilera. Characterization of laser induced plasmas by optical emission spectroscopy: A review of experiments and methods. *Spectrochimica Acta Part B*, 63(893-916), 2008.

[28] H. Ley. Analytical Methods in Plasma Diagnostic by Optical Emission Spectroscopy : A Tutorial Review. *Journal of Science and Technology*, 6(1), 2014.

[29] D. C. Meeker. Finite element method magnetics, Version 4.2 (28Feb2018 Build). `http://www.femm.info`.

[30] C. Steenkamp. High Power Solid State Modulator for Plasma Ion Implantation. Master's thesis, University of Saskatchewan, 116 Science Place, University of Saskatchewan, Saskatoon, S7N5E2, SK, 10 2006.

[31] M. E. Torres, M. A. Colominas, G. Schlotthauer, and P. Flandrin. A complete ensemble empirical mode decomposition with adaptive noise. *ICASSP, IEEE International Conference on Acoustics, Speech and Signal Processing - Proceedings*, pages 4144–4147, 2011.

[32] A. Zeiler, R. Faltermeier, I. R. Keck, A. M. Tomé, C. G. Puntonet, and E. W. Lang. Empirical mode decomposition - an introduction. In *Proceedings of the International Joint Conference on Neural Networks*, 2010.

[33] O. B. Fosso and M. Molinas. Method for Mode Mixing Separation in Empirical Mode Decomposition, 2017.

[34] Z. Wu and N. E. Huang. Ensemble Empirical Mode Decomposition: A Noise-assisted Data Analysis Method. *Advances in Adaptive Data Analysis*, 01(01):1–41, 2009.

[35] D. V. Sarwate and M. B. Pursley. Crosscorrelation properties of pseudorandom and related sequences. *Proceedings of the IEEE*, 68(5):593–619, 1980.

[36] Y. Lin and D. Joy. A new examination of secondary electron yield data. *Surface and interface analysis*, 37(895-900), 2005.

[37] D. Crintea, U. Czarnetzki, S. Iordanova, I. Koleva, and D. Luggenhölscher. Plasma diagnostics by optical emission spectroscopy on argon and comparison with Thomson scattering. *Journal of Physics D: Applied Physics*, 42(4):045208, jan 2009.

[38] A. Anders and G. Y. Yushkov. Plasma "anti-assistance" and "self-assistance" to high power impulse magnetron sputtering. *Journal of Applied Physics*, 105(7), 2010.

[39] P. Poolcharuansin and J. W. Bradley. Short- and long-term plasma phenomena in a HiPIMS discharge. *Plasma Sources Science and Technology*, 19(2):025010, 2010.

[40] Angstrom Sciences. Sputtering yields, accessed July 2020. `www.angstromsciences.com/sputtering-yields`.

[41] Y. Yang, X. Zhou, J. X. Liu, and A. Anders. Evidence for breathing modes in direct current, pulsed, and high power impulse magnetron sputtering plasmas. *Plasma Sources Science and Technology*, 108(3):034101, 2016.

[42] A. von Keudell, A. Hecimovic, and C. Maszl. Control of High Power Pulsed Magnetron Discharge by Monitoring the Current Voltage Characteristics. *Contributions to Plasma Physics*, 56(10):918–926, 2016.

[43] A Hecimovic, V Schulz von der Gathen, M Böke, A von Keudell, and J Winter. Spoke transitions in HiPIMS discharges. *Plasma Sources Science and Technology*, 24(4):045005, 2015.

[44] Newport. Newport quartz tungsten halogen lamp: Model 6334ns, accessed August 2020. `www.newport.com/p/6334NS`.

Appendix A

A.1 Figures

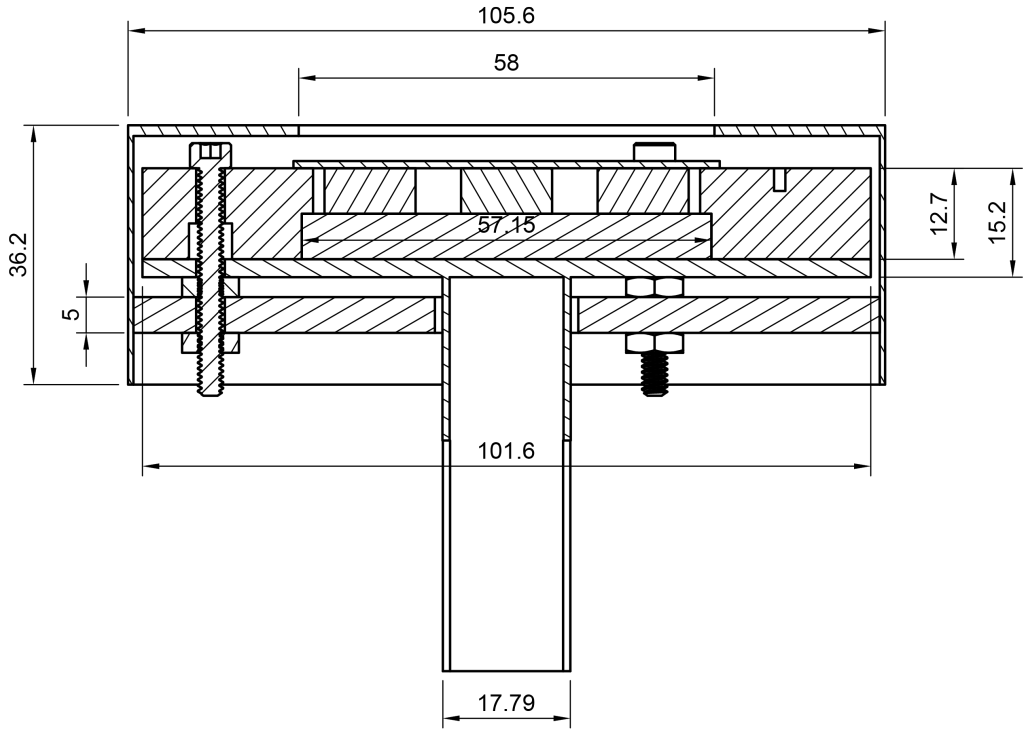

Figure A.1: Cross-section of magnetron assembly with dimensions in mm. The Teflon bolts holding the ground shield has tri-symmetry with respect to the centre vertical axis.

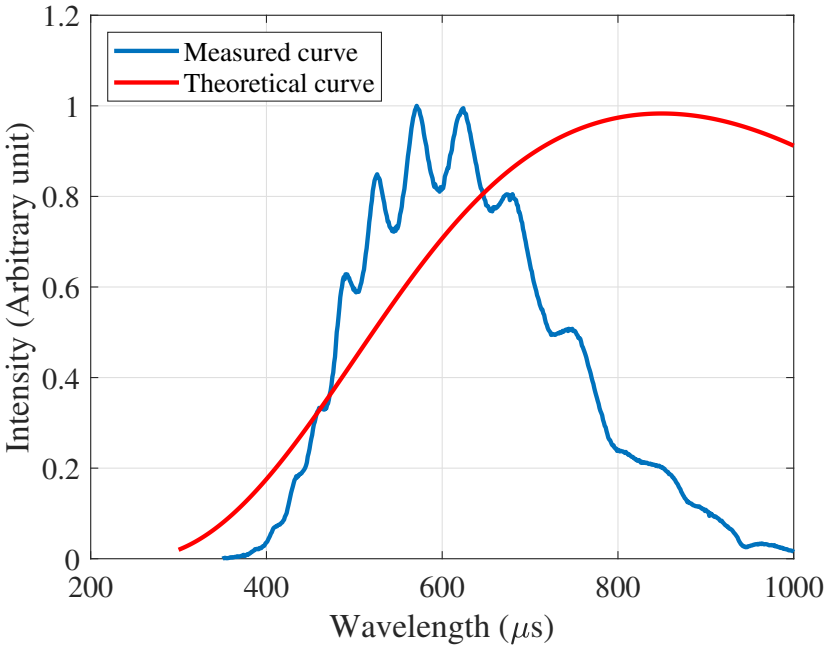

Figure A.2: Measured emission from calibrated quartz tungsten halogen lamp. The blue curve is the measured emission before calibration, the red curve is the theoretical curve obtained from the manufacturer [44]. The measured curve was scaled to match the theoretical, and the correction factor was used in subsequent measurements to scale the response of the spectrometer correctly.